

INFORMATION TO USERS

This manuscript has been reproduced from the microfilm master. UMI films the text directly from the original or copy submitted. Thus, some thesis and dissertation copies are in typewriter face, while others may be from any type of computer printer.

The quality of this reproduction is dependent upon the quality of the copy submitted. Broken or indistinct print, colored or poor quality illustrations and photographs, print bleedthrough, substandard margins, and improper alignment can adversely affect reproduction.

In the unlikely event that the author did not send UMI a complete manuscript and there are missing pages, these will be noted. Also, if unauthorized copyright material had to be removed, a note will indicate the deletion.

Oversize materials (e.g., maps, drawings, charts) are reproduced by sectioning the original, beginning at the upper left-hand corner and continuing from left to right in equal sections with small overlaps.

Photographs included in the original manuscript have been reproduced xerographically in this copy. Higher quality 6" x 9" black and white photographic prints are available for any photographs or illustrations appearing in this copy for an additional charge. Contact UMI directly to order.

ProQuest Information and Learning
300 North Zeeb Road, Ann Arbor, MI 48106-1346 USA
800-521-0600

UMI[®]

University of Alberta

**Investigating the Stability of Bitumen Droplets in Water through Force
Measurements**

by

Isabelle Laroche



A thesis submitted to the Faculty of Graduate Studies and Research in partial
fulfillment of the
requirements for the degree of Master of Science

Department of Chemical and Materials Engineering

Edmonton, Alberta

Spring 2000



National Library
of Canada

Acquisitions and
Bibliographic Services

395 Wellington Street
Ottawa ON K1A 0N4
Canada

Bibliothèque nationale
du Canada

Acquisitions et
services bibliographiques

395, rue Wellington
Ottawa ON K1A 0N4
Canada

Your file *Votre référence*

Our file *Notre référence*

The author has granted a non-exclusive licence allowing the National Library of Canada to reproduce, loan, distribute or sell copies of this thesis in microform, paper or electronic formats.

The author retains ownership of the copyright in this thesis. Neither the thesis nor substantial extracts from it may be printed or otherwise reproduced without the author's permission.

L'auteur a accordé une licence non exclusive permettant à la Bibliothèque nationale du Canada de reproduire, prêter, distribuer ou vendre des copies de cette thèse sous la forme de microfiche/film, de reproduction sur papier ou sur format électronique.

L'auteur conserve la propriété du droit d'auteur qui protège cette thèse. Ni la thèse ni des extraits substantiels de celle-ci ne doivent être imprimés ou autrement reproduits sans son autorisation.

0-612-60143-9

Canada

University of Alberta

Library Release Form

Name of Author: Isabelle Laroche

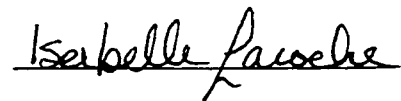
Title of Thesis: Investigating the Stability of Bitumen Droplets in Water through
Force Measurements

Degree: Master of Science

Year this Degree Granted: 2000

Permission is hereby granted to the University of Alberta Library to reproduce single copies of this thesis and to lend or sell such copies for private, scholarly or scientific research purposes only.

The author reserves all other publication and other rights in association with the copyright in the thesis, and except as herein before provided, neither the thesis nor any substantial portion thereof may be printed or otherwise reproduced in any material form whatever without the author's prior written permission.



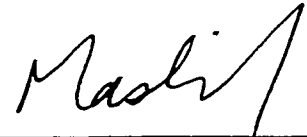
Isabelle Laroche
60, Des Merisiers,
Victoriaville, Québec,
G6P 2E7

Date: March 28, 2000

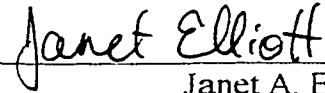
University of Alberta

Faculty of Graduate Studies and Research

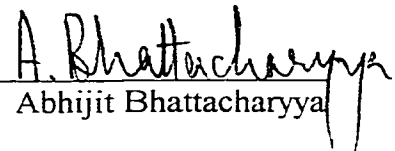
The undersigned certify that they have read, and recommend to the Faculty of Graduate Studies and Research for acceptance, a thesis entitled *Investigating the Stability of Bitumen Droplets in Water through Force Measurements* submitted by Isabelle Laroche in partial fulfillment of the requirements for the degree of Master of Science.



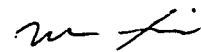
Jacob H. Masliyah
Supervisor



Janet A. Elliott



Abhijit Bhattacharyya



Xin Wu

Date: March 24, 2000

ABSTRACT

During the extraction of bitumen from oil sands, a very stable bitumen-in-water emulsion is formed, which results in the loss of a valuable amount of bitumen. The present study focuses on three important factors known to influence the stability of the emulsion: asphaltenes, pH of solution and clay. The stability was investigated through the measurement of the colloidal forces between bitumen droplets using a microcollider apparatus.

The presence of asphaltenes was found to considerably enhance the repulsion between the bitumen droplets whereas using a different electrolyte solution at a higher pH had the opposite effect. No significant effect on the interaction was seen when clay was added to the emulsion. Colloidal force models were applied to the experimental data in an attempt to characterise the surface of the bitumen droplets and the types of interaction forces. The results show that deasphalted bitumen is smoother than untreated bitumen.

A mes parents et à mes soeurs

Pour leur amour inconditionnel et tout ce qu'ils ont fait pour moi.

A ma belle petite puce, Roxane

Pour ta présence et tes sourires qui me comblent de bonheur.

Et à mon amour, Sylvain

Pour avoir respecté et supporté mon choix. Merci de ta patience et de ta compréhension.

L'attente est finie. Je reviens chez nous.

ACKNOWLEDGEMENT

I would like to take this opportunity to thank my supervisor, Dr. Jacob H. Masliyah, for his guidance and support throughout this work. I'm indebted to Dr. Alex Wu from Syncrude Canada Ltd. who was extremely helpful in many aspects of the present study and provided most of the computer programs used. I also acknowledge Dr. P. Warzyski and Dr. T.G.M. van de Ven (McGill University, Canada) who provided one of the computer programs used in the colloidal particle scattering technique. Finally, I'd like to thank Dr. Jan Czarnecki, also from Syncrude Canada Ltd., and all the colleagues who have helped me and made my stay most enjoyable. I greatly appreciated it.

I would also like to acknowledge the Natural Sciences and Engineering Research Council for its financial support. Finally, I want to acknowledge the Syncrude Chair Program in Oil Sands. Through this program, I had the opportunity to use state of the art equipment and to encounter leading scientists and engineers.

TABLE OF CONTENTS

CHAPTER 1: INTRODUCTION.....	1
1.1 Oil Sands	1
1.2. Problem Definition	3
1.3. Specific Objectives.....	5
1.4 Colloidal State	6
1.5. Literature Review	8
1.5.1. Colloidal Forces.....	8
1.5.1.1. Electrostatic Forces.....	8
1.5.1.2. Steric Forces	13
1.5.1.3. London-Van der Waals Forces.....	14
1.5.2. Force Models	18
1.5.2.1. DLVO Theory.....	18
1.5.2.2. Modified DLVO theories.....	19
1.5.2.2.1. Effect of Surface Roughness.....	20
1.5.2.2.2. Effect of Charge or Potential Heterogeneities.....	21
1.5.2.2.3. Combined effect of surface roughness and charge heterogeneity.....	23
1.5.3. Colloidal Force Measurement Techniques.....	25
1.5.4. Previous Studies of Bitumen-in-Water Emulsions.....	26
CHAPTER 2: EXPERIMENTAL.....	38
2.1. Materials.....	38
2.2. Equipment	39
2.2.1. Microcollider	39
2.2.2. Micro-Electrophoresis Apparatus	40
2.3. Manipulations.....	41
2.4. Experimental Methods.....	42
2.4.1. Colloidal Particle Scattering	42
2.4.2. Hydrodynamic Force Balance Technique.....	51

CHAPTER 3: INTERACTION OF BITUMEN DROPLETS USING COLLOIDAL PARTICLE SCATTERING	64
3.1. Effect of Asphaltenes.....	64
3.1.1. Interaction between Deasphalted Bitumen Droplets in 0.04M KCl.....	65
3.1.2. Interaction between Bitumen Droplets in 0.04M KCl	73
3.2. Effect of Electrolyte on Bitumen Droplet Collision.....	79
3.3. Effect of Clay	83
CHAPTER 4: MEASUREMENT OF THE MAXIMUM ATTRACTIVE FORCE USING HYDRODYNAMIC FORCE BALANCE	113
4.1. Effect of Asphaltenes.....	115
4.2. Effect of Electrolyte and pH.....	118
4.3. Discussion and Conclusions	120
CHAPTER 5: CONCLUSIONS	128
5.1. Review of Problem and Objectives.....	128
5.2. Summary of Experimental Results	129
5.3. Force Modelling	130
5.4. Achievements	133
5.5. Recommendations for Future Work.....	133
BIBLIOGRAPHY	136
APPENDIX A: MULTIPLE SPHERICAL CAP MODEL	144

LIST OF TABLES

Table 1.1: Summary of Force Measurement Techniques.....	33
Table 4.1: Maximum Attractive Force for Deasphalted Bitumen in a 0.1M KCl Solution.....	123
Table 4.2: Maximum Attractive Force for Untreated Bitumen in a 0.1M KCl Solution.....	124
Table 4.3: Maximum Attractive Force for Untreated Bitumen in a 0.1M (NaCl + NaHCO ₃) Solution	125
Table 4.4: Summary of Maximum Attractive Force Measurements	127

LIST OF FIGURES

Figure 1.1: Syncrude's Bitumen Extraction Process.....	29
Figure 1.2: Stern Model for the Diffuse Electric Layer	30
Figure 1.3: Steric Force Model.....	31
Figure 1.4: DLVO Typical Force and Energy Graphs	32
Figure 2.1: Microcollider Apparatus	56
Figure 2.2: Basic Principles of Colloidal Particle Scattering.....	57
Figure 2.3: Particle Trajectories in Colloidal Particle Scattering.....	58
Figure 2.4: Typical Scattering Diagram.....	59
Figure 2.5: Calculation Scheme for Colloidal Particle Scattering	60
Figure 2.6: Location of the Maximum Colloidal Attractive Force on a Typical Force-Distance Curve.....	61
Figure 2.7: Principles of Hydrodynamic Force Balance Technique.....	62
Figure 2.8: Representation of the Forces Involved in the Hydrodynamic Force Balance Technique.....	63
Figure 3.1: Scattering Diagram for Deasphalted Bitumen in 0.04M KCl - DLVO Theory	89
Figure 3.2: SEM Image of Deasphalted Bitumen	90
Figure 3.3: Single Disk Model.....	91
Figure 3.4: Scattering Diagram for Deasphalted Bitumen in 0.04M KCl - Single Disk Model	92
Figure 3.5: Mechanisms for Repulsion due to Polymeric Chain Adsorption.....	93
Figure 3.6: Scattering Diagram for Deasphalted Bitumen in 0.04M KCl - Enhanced Electrostatic Repulsion Model.....	94
Figure 3.7: Scattering Diagram for Deasphalted Bitumen in 0.04M KCl - Steric Repulsion Model	95
Figure 3.8: SEM Image of Untreated Bitumen	96

Figure 3.9a: Scattering Diagram for Bitumen in 0.04M KCl - Single Disk Model (after 1 st screening)	97
Figure 3.9b: Scattering Diagram for Bitumen in 0.04M KCl - Single Disk Model (after 2 nd screening).....	98
Figure 3.10: Force Profiles - Comparison of Roughness Models	99
Figure 3.11: Scattering Diagram for Bitumen in 0.04M KCl - Enhanced Electrostatic Repulsion Model.....	100
Figure 3.12: Scattering Diagram for Bitumen in 0.04M KCl - Steric Repulsion Model.....	101
Figure 3.13: Scattering Diagram for Bitumen in 0.025M NaCl + 0.015M NaHCO ₃ - DLVO and Single Disk Models	102
Figure 3.14: Scattering Diagram for Bitumen in 0.025M NaCl + 0.015M NaHCO ₃ - Enhanced Electrostatic Repulsion Model	105
Figure 3.15: Scattering Diagram for Bitumen in 0.025M NaCl + 0.015M NaHCO ₃ - Steric Repulsion Model	108
Figure 3.16: Shell and Core Model.....	111
Figure 3.17: Scattering Diagram for Bitumen with Clay in 0.025M NaCl + 0.015M NaHCO ₃ - Shell and Core Model	112

NOMENCLATURE

Abbreviations

EUB	Alberta Energy and Utilities Board
PSV	Primary Separation Vessel
TOR	Tailings Oil Recovery Unit
DRU	Diluent Recovery Unit
DLVO	Derjaguin, Landau, Verwey and Overbeek's theory on colloidal interaction
CPS	Colloidal Particle Scattering
HFB	Hydrodynamic Force Balance
Re	Reynolds number
SEM	Scanning Electron Microscope

Symbols

κ^{-1}	Thickness of the electric double layer (m)
ϵ	Dielectric constant of the medium
ϵ_0	Permittivity of vacuum, 8.854×10^{-12} C/Vm
k	Boltzmann constant, 1.381×10^{-23} J/K
T	Temperature (K)
e	Elementary charge, 1.602×10^{-19} C
z	Valence of electrolyte
n_∞	Ionic number concentration
N_A	Avogadro number, 6.022×10^{23} mol ⁻¹
M	Molarity (mol)
∇^2	Laplacian Operator

$\bar{\nabla}$	Gradient Operator
ψ	Potential (V)
ψ_0	Surface potential (V)
ψ_m	Potential midway between two parallel plates (V)
ζ	Zeta potential (V)
p	Osmotic pressure (kPa)
x, y, z	Cartesian coordinates
\mathbf{F}_{el}	Electrostatic force (N)
h	Separation distance between two colloidal bodies (m)
a	Radius of a droplet (m)
\mathbf{F}_s	Steric force (N)
A	Hamaker constant (J)
A_{ij}	Hamaker constant of body i interacting with body j in vacuum (J)
A_{ijk}	Hamaker constant of body i interacting with body k in medium j (J)
L_s	Steric layer thickness (m)
δ	Thickness of two flat plates (m)
V_{vdw}	London-van der Waals potential energy (J)
\mathbf{F}_{vdw}	London-van der Waals force (N)
$\mathbf{f}(p)$	Retardation function for \mathbf{F}_{vdw}
p	Dummy variable function of h and λ
λ	Retardation wavelength (m)
V_{el}	Electrostatic potential energy (J)
\mathbf{r}	Position vector of the mobile droplet (m)
\mathbf{M}	Mobility tensor ($s \cdot kg^{-1}$)
\mathbf{F}_{hydr}	Hydrodynamic force vector (N)
$\mathbf{F}_{colloidal}$	Colloidal force vector (N)
μ	Fluid viscosity ($kg \cdot m^{-1} \cdot s^{-1}$)
\mathbf{v}	Fluid velocity vector ($m \cdot s^{-1}$)
\mathbf{v}^0	Undisturbed fluid velocity vector ($m \cdot s^{-1}$)
$\mathbf{f}(y)$	Force density ($N \cdot m^{-2}$)

τ	Oseen tensor ($\text{m}^2 \cdot \text{s} \cdot \text{kg}^{-1}$)
S	Surface of a particle (m^2)
$\mathbf{F}_{\text{resist}}$	Hydrodynamic resistance force exerted on a mobile droplet in a quiescent fluid (N)
\mathbf{u}	Velocity vector of the mobile sphere ($\text{m} \cdot \text{s}^{-1}$)
f_i	Component of the force vector acting in direction i (N)
t_i	Component of the torque vector acting in direction i (N)
u_i	Translational velocity in direction i ($\text{m} \cdot \text{s}^{-1}$)
w_i	Rotational velocity in direction i ($\text{rad} \cdot \text{s}^{-1}$)
G	Shear rate (s^{-1})
t	Time (s)
t_b	Time at which the doublet break-up occurred (s)

Parameters Specific to Given Models

Disk Model

L	Disk thickness (m)
r	Disk radius (m)
A_{s-s}	Hamaker constant for the interaction between two spheres in aqueous medium (J)
A_{d-s}	Hamaker constant for the interaction between a disk and a sphere in aqueous medium (J)
A_{d-d}	Hamaker constant for the interaction between two disks in aqueous medium (J)

Steric Repulsion and Enhanced Electrostatic Repulsion Models

L	Thickness of layer of adsorbed polymeric chains (m)
-----	---

Multiple Spherical Caps Model

$F_{\text{sph.caps}}(h_i)$	Electrostatic force between two spherical caps separated by a distance h_i (N)
a_c	Radius of the sphere from which the spherical caps is taken (m)
r	Spherical cap radius (m)
L	Thickness of spherical caps (m)
z	Radial distance from centre of spherical caps (m)
v	Electrolyte valence

Shell and Core Model

L	Thickness of clay layer (m)
L_s	Thickness of steric layer (m)
A_{b-b}	Hamaker constant for the interaction between two bitumen bodies in water (J)
A_{c-c}	Hamaker constant for the interaction between two clay bodies in water (J)

CHAPTER 1

INTRODUCTION

1.1 Oil Sands

Energy resources have greatly contributed to the development of the industrial world in the last century. Gas and oil are among the most commonly used energy sources and their consumption is steadily increasing [1]. However, as the easily exploitable conventional oil pools are depleting, it is becoming more difficult to technically and economically process this non-renewable conventional resource. Natural Resources Canada estimates the Canadian crude oil reserves at only 769 million cubic meters as of 1999 [1]. Alberta Energy and Utilities Board (EUB) stated that in 1997 the remaining established reserves of Conventional Crude Oil for Alberta was 327 million cubic meters [2]. However, the total amount of bitumen in Alberta, including bitumen from oil sands, is estimated at 1.3 trillion barrels (≈ 210 billion m^3) [3]. Thus, it is expected that Canada's energy supply would be assured for at least one century if oil sands production is further developed.

Alberta has the largest known oil sands deposit in the world, namely the Athabasca deposit, which is located in the northeastern part of the province. This deposit alone contains 830 billion barrels (≈ 130 billion m^3) of bitumen [3]. The province of Alberta also has three other major deposits: Wabasca, Peace River and Cold Lake. However, only 15% of Alberta's bitumen is considered surface-mineable. In fact, the Alberta Energy and Utilities Board [2] estimates the total amount of surface-mineable bitumen to be approximately 24.1 billions cubic meters. Considering a minimum saturation and thickness criteria and applying an economic-strip-ratio criteria within the surface-mineable area, the EUB estimates that 11.2 billions cubic meters of bitumen is economically mineable.

Oil sands consist of an unconsolidated mineral sand matrix covered with bitumen. Bitumen can be considered as a viscous hydrogen-deficient petroleum, often composed of molecules containing more than two thousands carbon atoms. It is commonly known that minerals form the major part of the oil sands mined in the Athabasca deposit with approximately 85% silica sand, clays and silts, 10% by weight bitumen and 5% water. Fines form roughly 10 to 35% of the total mineral content [4]. The bitumen content may vary greatly within a deposit. An ore containing more than 12% by weight bitumen is considered a rich oil sand and one having between 6 to 9% of bitumen is rated as a lean ore [5]. When the bitumen content is within the 9 to 12% range, the ore is regarded as one of moderate quality. When the bitumen content is lower than 6%, it is generally not considered an “ore-grade” quality.

Bitumen is usually extracted from oil sands by the Clark Hot Water Process, although there is currently a shift in the industry towards a lower temperature and caustic-free process. Figure 1.1 gives a simplified representation of Syncrude’s extraction process [5]. First, oil sands are mined and transported to the extraction plant where the oil sands ore is mixed with water, air and caustic soda to yield a pH of 8 to 8.5. Through agitation and thermal energy input, the layers of bitumen are warmed and sheared away until the bitumen completely separates from the sand grain and forms droplets. In the process, the droplets also attach to air bubbles. The slurry is fed to a separation unit that is called the “primary separation vessel” (PSV).

Once in the PSV, the aerated bitumen floats to the surface of the vessel to form a froth. The bitumen froth is recovered by skimming before being de-aerated in towers. To prevent solids build-up, a stream is retrieved from the middle of the PSV. This stream is called the “middlings”. It contains most of the fines and a valuable amount of the smaller and poorly aerated bitumen droplets that do not float easily. The bottom stream of the primary separation, called the primary tailings, contains coarse

solids and residual bitumen. Both the middlings and the primary tailings are combined and sent to a tailings oil recovery (TOR) unit and to flotation cells for further treatment.

The combined froth from the PSV and the flotation cells contains roughly 60% bitumen, 30% water and 10% solids [5]. Further treatment of this froth consists of removing the excess fine solids and water. The froth is thus diluted with a solvent such as naphtha (1:0.7 by weight) and centrifuged. Finally, the solvent and water are removed and bitumen becomes ready for upgrading. Overall, more than 90% of the bitumen contained in the oil sands is recovered.

The bottom streams from the flotation processes are called “tailings”. They contain mostly solids and water, but also approximately 2% of emulsified bitumen. These tailings are sent to tailing ponds where the solids are allowed to settle.

1.2. Problem Definition

The bitumen droplets remaining in the tailings stream form a very stable bitumen-in-water emulsion. The amount of bitumen lost in this stream depends on the quality of the ore. For a good-processing ore, the separation process produces droplets having a diameter of the order of several hundred microns. These larger droplets adhere more easily to the air bubbles in the flotation part of the process and thus, more bitumen is recovered. For a poor-processing ore, the droplets have a diameter as small as microns or tens of microns and tend to stay in suspension rather than adhere to air bubbles [6]. Since a poor ore usually contains more fines than a good ore, it is strongly believed that fines (clay, silica and other minerals smaller than 44 μm in size) play a role in the stabilisation of the bitumen emulsion.

The extraction process allows for the removal of nearly all the solid particles but when the diluted bitumen leaves the last centrifuge, it still contains 2 to 3 % water and 0.5% solid particles [4]. The water will be removed in the diluent recovery unit (DRU), but the salts that were in the water droplets and the solids remain with the bitumen. These solids have a sub-micron size and they do not settle. In addition, bitumen itself contains some precipitable materials, known as asphaltenes.

Asphaltenes are the insoluble part of bitumen in pentane (C5-Asphaltenes), hexane (C6-Asphaltenes) or heptane (C7-Asphaltenes). They are large aromatic polycyclic compounds containing mostly carbon and hydrogen, but also sulphur, nitrogen, oxygen and metals. The molecular weight of petroleum asphaltenes is usually in the 1500 to 2500 range [5]. Asphaltenes form aggregates in bitumen. These aggregates are considered surface-active and therefore have an important effect on the interaction between the bitumen droplets [7].

Another important issue in bitumen extraction from oil sands is that optimum operating conditions depend on the ore quality. For example, the liberation step of the bitumen from the sand grains requires very little sodium hydroxide for a rich ore whereas a much higher amount is needed for leaner grades. The sodium hydroxide addition helps in neutralising the bitumen organic acids to produce surfactants. These surfactants lower the bitumen-water interfacial tension, which favours the liberation step. The surfactants are more easily produced in a good ore. However, too much surfactant has an adverse effect of covering the air bubbles and the bitumen droplets surfaces, which makes them more hydrophilic and consequently has a negative effect on bitumen-air attachment. It can also favour bitumen emulsification by lowering the interfacial tension. Thus, the free surfactant concentration is an important parameter to optimise for maximum recovery [8]. Furthermore, for a given electrolyte concentration, adding sodium hydroxide increases the negative potential of bitumen and solids interfaces, which enhances bitumen liberation but also increases the repulsion between the bitumen droplets. Again, the addition of sodium hydroxide has

an effect on the stability of the emulsion. Thus, presence of electrolyte and pH level used in the bitumen extraction process influence bitumen recovery.

1.3. Specific Objectives

To improve the current overall recovery rate of bitumen, it is necessary to understand how a water-bitumen-fines system is stabilised and how to destabilise it. This study was performed with this goal in mind. The study emphasises the problem of bitumen losses in the tailings stream, losses due to the existence of a stable oil-in-water emulsion. The current investigation complements previous studies by Wu *et al.* [6, 9, 10] on the measurement of interaction forces between bitumen droplets in an aqueous medium.

More specifically, the objectives of this study are:

1. To observe the effect of electrolyte and pH by comparing the results obtained in the presence of KCl to those obtained with a combination of NaCl and NaHCO₃, a system closer to the actual plant operating conditions.
2. To study the influence of clays by adding asphaltenes-treated clays to an aqueous solution containing bitumen droplets.
3. To investigate the effect of asphaltenes by comparing the interaction forces between deasphalted bitumen droplets and the forces between untreated bitumen droplets.
4. To model the interaction forces and attempt to characterise the surface of the bitumen droplets.

Emulsion stability was investigated through the measurement of interaction forces between individual droplets, using a microcollider apparatus that will be described later.

1.4 Colloidal State

The bitumen droplets carried out in the tailing stream are usually very small and are considered of colloidal range. A colloidal state involves small particles or systems for which the ratio of surface area to volume is large. In fact, colloidal particles are defined as particles having a size ranging from 1 nm to 1 μm . The definition is sometimes extended to a higher limit of 10 μm . The lower limit of the size-based definition corresponds to the molecular level boundary whereas the higher limit corresponds to a size beyond which the Brownian motion is not observed. It is worth to note that both the dispersed and the continuous phases can be solids, liquids or gases. The properties of a colloidal system strongly depend on the interaction between the two phases. This interaction between the two phases is in turn a function of the geometry and size of the particles and of the chemical and physical properties of both the surface and the continuous phase. In some cases, more than two phases may be involved. Mists, paints, inks, froths, pigmented plastics, blood, milk and silica gels are a few examples of colloidal systems.

Colloids play a major role in many aspects of technology and biology. Although humans have used colloids and made use of their special properties since the earliest days of civilisation, their existence was only proven in the 19th century. In fact, colloidal science is still a relatively new discipline that dates back to the middle of the 19th century. This is probably due to the difficulty of proving their existence and studying their behaviour. In fact, the dimensions of most colloidal particles, i.e. those below 1 μm , are below the limits of resolution of simple optical microscope. Hence,

“seeing” colloids and measuring their size only became possible after the electron microscope was invented in the 1930s.

Reference [11] provides a good historical review of colloidal science that is summarised below. The first experimental studies of colloidal systems were made by Selmi in 1845 when he prepared suspensions of sulphur and silver halides. Faraday in 1856-1857 systematically studied colloidal gold. He observed that when small amounts of salts are added to colloidal gold dispersions, their colour irreversibly changes from ruby to blue. He also observed that the blue solution tended to produce solid deposits. He stated that changing conditions didn't modify the gold itself but rather influenced the relations between the gold particle surface and the surrounding medium. He concluded that gold was present in a finely divided form and that the change of colour was due to the association of many colloidal gold particles. His ideas are still used in modern theories of stability of dispersions. Another colloidal science pioneer, Thomas Graham (1861) studied diffusion through membranes of matter soluble in water. He named those retained by the membranes (proteins and glue) “colloids” from the Greek $\kappa\omicron\lambda\lambda\alpha$, i.e. glue.

The stability of a colloidal system depends greatly on the particle surface properties. A colloidal emulsion system is thermodynamically unstable¹. However, the coalescence rate can be so low that the colloidal system may appear to stay stable for months and even years. From a practical perspective, such systems are considered stable.

Stability can also be related to the tendency of droplets or particles to aggregate, as it is the case for the present study. Aggregation can be prevented by certain means, as it will be seen later. In addition, in order to form an aggregate, a collision between two particles or aggregates must occur. Collisions are aided by the thermal (or Brownian) motion of the molecules of the dispersion medium or by mechanical agitation.

¹ It may not be so for some sterically stabilised colloidal systems.

Stability can be a desired or an undesired property, depending on the application on hand.

1.5. Literature Review

1.5.1. Colloidal Forces

Before discussing any specific force model, it is necessary to understand the forces encountered in colloidal systems. Common forces such as gravity, buoyancy and hydrodynamic forces may be present. However, these forces are not considered colloidal forces. Three major forces are typical to colloidal particles or droplets. These forces are the electrostatic, steric and London-van der Waals forces [12]. In a bitumen system, the first two forces are repulsive and consequently stabilise the particles against aggregation (by flocculation or coagulation). The third force is attractive and is responsible for bringing particles together. All the forces will be described shortly. Structural forces such as solvation and hydration forces may also be present at very small surface-to-surface distances.

1.5.1.1. Electrostatic Forces

Electrostatic forces arise due to a charged surface and the presence of an associated diffuse atmosphere of counter-ions, called the “electric double-layer”. When a colloidal particle or a droplet is immersed in an aqueous solution, it acquires a charge at its surface. This surface charge induces an electric field. More counter-ions of the electrolyte solution are present near the surface whereas more co-ions are pushed away. Since a colloidal dispersion in itself is electronically neutral, the concentration of ions having a charge opposite to that of the particle will be higher close to the surface than in the bulk phase. This difference in the ionic concentration creates a

potential difference between the vicinity of the particle surface and the bulk of the solution and produces the electric double-layer.

As two colloidal particles approach each other, their double layers begin to overlap, which destroys the symmetric distribution of the ions and potential. The asymmetric distribution of the potential creates electrical asymmetrical stresses and consequently, the particles experience a force that is related to the thickness of the diffuse layer.

Gouy in 1910 [13] and Chapman in 1913 [14] independently derived the first realistic model of the double-layer. The model, referred to as the Gouy-Chapman model, accounts for thermal diffusion. In the Gouy-Chapman model for the diffuse layer, the concentration of the ions decays exponentially from the surface to the bulk. There is no charge neutrality within this diffuse layer. Equilibrium is instead related to attraction/repulsion and diffusion forces arising from concentration gradients.

For a symmetric electrolyte ($z : z$), the thickness of the double-layer, κ^{-1} , also called the Debye length, is defined as [12]:

$$\kappa^{-1} = \left[\frac{\epsilon \epsilon_0 kT}{2e^2 z^2 n_\infty} \right]^{1/2} \quad (1.1)$$

where the ionic number concentration $n_\infty = 1000 N_A M$, in which N_A is the Avogadro number, $6.022 \times 10^{23} \text{ mol}^{-1}$, ϵ is the dielectric constant of the medium, ϵ_0 is the permittivity of vacuum, k is the Boltzmann constant, T is the absolute temperature, e is the elementary charge and z is the valence of the symmetric electrolyte.

To calculate the electrostatic force, the Poisson-Boltzmann equation for the potential distribution has to be solved along with the momentum equation. These two equations, without fluid flow and neglecting gravity, are respectively [12]:

$$\varepsilon\varepsilon_0 \nabla^2 \psi = - \sum_{i=1}^N n_{i\infty} z_i e \exp\left(-\frac{z_i e \psi}{kT}\right) \quad (1.2)$$

$$\bar{\nabla} p = \varepsilon\varepsilon_0 \nabla^2 \psi \cdot \bar{\nabla} \psi \quad (1.3)$$

where p is the osmotic pressure, i is one of the electronic species (for example: K^+ , Ca^{++} , Cl^-) and ψ is the potential.

The force per unit area driving two plane surfaces away from each other is given by the difference between the pressure midway from the surfaces and the pressure at an infinite distance. The force is thus evaluated by integrating the pressure term of the momentum equation over the entire surface of the planes. For two identical parallel flat plates placed in a symmetric electrolyte solution, the solution of Equations 1.2 and 1.3 based on the Gouy-Chapman analysis is given by [15]:

$$\psi = \frac{2kT}{ze} \ln \left[\frac{1 + \tanh\left(\frac{ze\psi_o}{4kT}\right) \exp(-\kappa x)}{1 - \tanh\left(\frac{ze\psi_o}{4kT}\right) \exp(-\kappa x)} \right] \quad (1.4)$$

$$F_{el} = 2kTn_{\infty} \left[\cosh\left(\frac{ze\psi_m}{kT}\right) - 1 \right] \quad (1.5)$$

where ψ is the potential, ψ_o is the potential at the surface of the plates, x is the normal distance (with $x = 0$ corresponding to the surface of one of the plates), F_{el} is the electrostatic force and ψ_m is the potential midway from the plates.

Equation 1.5 was first derived by Langmuir (1938) [16] and Derjaguin (1940) [17].

The potential midway between the plates, ψ_m is calculated as the sum of the potential

of each plate at a distance $h/2$, where h is the separation distance between the plates [18]. The assumption is valid for small potentials.

When $ze\psi_m/kT$ is much lower than 1, the hyperbolic cosine term of Equation 1.5 can be expanded using Taylor's series expansion and the force between two plates as given by Equation 1.5 becomes [15]:

$$F_{el} = 32\kappa^2 \epsilon\epsilon_o \left(\frac{kT}{ze}\right)^2 \tanh^2\left(\frac{e\psi_o}{4kT}\right) \exp(-\kappa h) \quad (1.6)$$

To calculate the force between two spherical particles, a useful procedure is adopted. This procedure is called the Derjaguin approximation [19]. This approximation is acceptable when the range of interaction is small in comparison to the radius of the particles. The Derjaguin approximation consists of replacing particles with curved boundaries by a series of parallel flat strips and integrating over the entire surface using the flat plate equation previously shown.

Based on this approximation, the force between parallel cylinders and then between parallel cylindrical strips were calculated. The results are subsequently used to evaluate the electrostatic force between two spheres [15]:

$$F_{el} = 32\pi a \epsilon\epsilon_o \kappa \left(\frac{kT}{ze}\right)^2 \tanh^2\left(\frac{ze\psi_o}{4kT}\right) \exp(-\kappa h) \quad (1.7)$$

The Gouy-Chapman model for the diffuse layer gives good quantitative results when the surface potential and the electrolyte concentration are low. However, one major drawback of this model is that it assumes that ions are point charges and thus, they can approach the surface without limit. Therefore, the predicted concentration of

counter-ions at the surface is physically unrealistic. In reality, a minimum separation of one ionic radius is present.

Stern in 1924 [20] modified the Gouy-Chapman model for the double-layer to account for the finite size of the ions. He found that most of the error arising from the Gouy-Chapman model could be attributed to the first layer of adsorbed ions and that it is acceptable to consider the remainder of the ions as point charges. Stern thus divided the diffuse layer in two parts: a stationary layer of ions of finite thickness, and a diffuse layer identical to that of Gouy and Chapman. The immobile layer is called the Stern layer and is held in place by electrostatic and van der Waals forces (to be discussed shortly). The Stern layer is only able to contain a maximum number of counter-ions per unit surface area.

Figure 1.2 gives a conceptual representation of the Stern model. The figure is adapted from Schramm [5]. The Stern model accounts for a shear plane between the Stern layer and the diffuse layer. In fact, the shear plane and the Stern layer are not at the same position. However, due to the difficulty in finding the actual location of the Stern plane, it is usually assumed to be at the shear plane. The potential at the shear plane is called the zeta potential. As shown by Figure 1.2, the zeta potential is slightly different from the Stern potential. Thus, the Stern model is still a rough approximation of real systems, but it nonetheless provides an adequate representation of the experimental results.

The procedure presented above to develop the force equations from the Gouy-Chapman model is still valid when the Stern model is used. In this case, the zeta potential has to be specified instead of the surface potential. Furthermore, the distance between the two particles or plates has to be taken as the distance between their shear planes and not between their surfaces. Finally, the no-slip condition is assumed to apply at the shear plane.

1.5.1.2. Steric Forces

Repulsion can occur by other means than electrostatic interaction. Steric forces, for example, are repulsive forces that occur when long polymeric chains adsorbed on the colloidal particle surfaces begin to overlap. These polymeric chains prevent a close approach of the colloidal particles and their effectiveness strongly depends on the continuous phase. In a good solvent, the long polymeric chains extend far from the surfaces, making the colloids “sterically” stabilised. On the other hand, when a poor solvent is used, the chains stay closer to the surface and the steric effect is limited. Another mechanism is believed to contribute to the repulsive force. Upon close approach, the concentration of the polymeric chains becomes high, leading to a higher osmotic pressure in the overlap region. This osmotic effect pushes the particles away from each other.

Steric forces are usually not included in colloidal interaction models, with the exception of polymer-coated particle systems. In fact, although some theories for steric interaction exist, these steric interaction theories are based on thermodynamic calculation for equilibrium systems [21] and are best suited to static interactions rather than to dynamic interactions.

The reason as to why so few steric force theories exist for dynamic interaction is that very little is known on the system behaviour, apart from the fact that the steric force-distance curves show a steep increase in the force as the gap between the two particles becomes small. Wu *et al.* [10] proposed the following high-order polynomial expression to model the steric force.

$$F_s = \frac{c}{h^7} = \frac{8AaL_s^5}{3h^7} \quad (1.8)$$

The parameter c was defined in such a way that the addition of the steric force given by Equation 1.8 to the unretarded van der Waals equation (cf. Equation 1.11 of the next section) gives a total force of zero at a distance of $2L_s$, where L_s is the thickness of the steric layer. Figure 1.3 provides a representation of the steric force model and defines the parameters of the model.

1.5.1.3. London-Van der Waals Forces

The London-van der Waals forces, also known as dispersion forces, act on neutral molecules or atoms. The London-van der Waals forces are due to induced dipoles originating from the spontaneous fluctuations in the electronic clouds of the atoms [12,15]. When there is fluctuation of one electronic cloud in a given material, it induces a corresponding fluctuation in the electronic cloud of a neighbour material. These relative electronic fluctuations create a force. From an energetic perspective, antiparallel dipole orientations are more likely to occur and thus, dipoles are more frequently in these configurations. Hence, statistically attraction dominates and the London-van der Waals forces are always attractive. The London-van der Waals forces are exclusively quantum mechanical forces. Therefore, they can be written using the same oscillatory strengths used in the equations of light.

Two approaches have been used to calculate the dispersion forces. The first one, based on a molecular model, was developed by Hamaker in 1937 [22]. The second approach, based on a molar model of condensed media, was developed by Lifshitz in 1956 [23]. Hamaker's model sums the attractive energy of all possible pairs of molecules in two distinct bodies. The free energy of interaction between the two bodies is calculated by multiplying a material-dependent constant, the Hamaker constant A , and a geometry-dependent integral.

For two infinite flat plates of the same material with a thickness δ , the potential energy is given by [12]:

$$V_{\text{vdw}} = -\frac{A}{12\pi} \left(\frac{1}{h^2} + \frac{1}{(h+2\delta)^2} - \frac{2}{(h+\delta)^2} \right) \quad (1.9)$$

where V_{vdw} is the London-van der Waals potential energy, A is the Hamaker constant of the plates and h is the separation between the two flat plates. When the plate thickness is large compared to the separation distance Equation 1.9 reduces to the first term only.

For two spheres of the same material with radius of a_1 and a_2 much larger than their separation distance, the attractive potential energy, V_{vdw} , is given by [12]:

$$V_{\text{vdw}} = -\frac{Aa_1a_2}{6h(a_1+a_2)} \quad (1.10)$$

where A in this case refers to the Hamaker constant of the spheres.

Finally, the force is given by:

$$F_A = -\frac{dV_{\text{vdw}}}{dh} = -\frac{Aa_1a_2}{6(a_1+a_2)h^2} \quad (1.11)$$

Hamaker [12, 22] made a few assumptions to derive expressions for the forces. He first assumed that multibody forces could be ignored and that these forces were spontaneous and due to a single dominant frequency only. He also assumed that the bodies were in vacuum, that they had a uniform density up to the interface and that

attractive forces did not distort them. In addition, the effect of free charge and permanent dipoles were neglected.

As mentioned, these expressions were developed for particles in vacuum. When the medium is a dielectric, a correction must be applied to the Hamaker constant. This correction for bodies 2 and 3 separated by a medium 1 is given by [12]:

$$A_{312} = [A_{33}^{1/2} - A_{11}^{1/2}][A_{22}^{1/2} - A_{11}^{1/2}] \quad (1.12)$$

where A_{312} is the corrected Hamaker constant accounting for the presence of the medium, A_{11} is the Hamaker constant of the medium, A_{22} is the Hamaker constant of body 2 and A_{33} is the Hamaker constant of body 3.

In addition, Hamaker [22] assumed that the electromagnetic interactions were spontaneous, i.e. the speed of the electromagnetic signal (speed of light) is infinite. This assumption is acceptable for very small separation distances. However, the energy decays more steeply at large separation distances because the fluctuating electric moments become slightly out of phase due to the finite time for electric field propagation. To account for this effect, the force expressions obtained by Hamaker have to be multiplied by a retardation function.

Schenkel and Kitchener [24] gave an expression for the retardation function, $f(h)$, between two identical spheres:

$$f(p) = \frac{1 + 3.54p}{(1 + 1.77p)^2} \quad \text{if } p \leq 1$$

$$f(p) = \frac{0.98}{p} - \frac{0.434}{p^2} + \frac{0.67}{p^3} \quad \text{if } p > 1 \quad (1.13)$$

In Equation 1.13, $p = 2\pi h/\lambda$ where h is the separation distance and λ the retardation wavelength, usually assumed to be 100 nm.

For two flat plates, the following expression obtained by Overbeek [25] can be used:

$$f(h) = 0.168 - 0.093\left(\frac{\pi h}{\lambda}\right) + 0.019\left(\frac{\pi h}{\lambda}\right)^3 - 0.005\left(\frac{\pi h}{\lambda}\right)^4 \quad (1.14)$$

Equations 1.13 and 1.14 apply to the van der Waals force equation. Thus, the retarded van der Waals force is given by:

$$F_{\text{vdw,retarded}} = F_{\text{vdw,unretarded}} f(h) \quad (1.15)$$

In Lifshitz's approach [12, 23] for the van der Waals interaction, the decrease of the zero-point energy of a particle is calculated from quantum electrodynamics. This decrease in the zero-point energy of a particle is caused by the co-ordination of the particle electric moments with those of a particle located nearby. To use Lifshitz's theory for the calculations of the van der Waals interaction, the complete range of dielectric susceptibilities with respect to frequency must be known. With the exception of a few materials, these dielectric susceptibilities are usually not known. Ninham and Parsegian (1970) [26] developed a numerical method to approximate the value of the dielectric susceptibilities. However, the susceptibility relationship with frequency is still only available for common materials. Therefore, this exact theory is not very frequently used and will not be further discussed here.

1.5.2. Force Models

1.5.2.1. DLVO Theory

The most commonly used theory in colloidal science is called the DLVO theory, based on the researchers who independently proposed it: Derjaguin and Landau (USSR) [27], and Verwey and Overbeek (Netherlands) [18]. The DLVO theory assumes that the two most important contributions to colloidal interaction are the electrostatic interaction and the London-van der Waals interaction. The theory also assumes that both contributions are additive. Hence, the total potential energy of interaction based on the DLVO theory is given by:

$$V_{\text{Total}} = V_{\text{el}} + V_{\text{vdw}} \quad (1.16)$$

Similarly, the interaction force is given by:

$$F_{\text{Total}} = F_{\text{el}} + F_{\text{vdw}} \quad (1.17)$$

Figure 1.4 shows some typical interaction curves calculated from the DLVO theory for two identical spherical droplets. Figure 1.4a presents the potential energy profile whereas Figure 1.4b gives the force profile. As it can be observed from these two figures, the interaction varies significantly with the separation distance. The potential energy curve possesses two important features that may or may not be present depending on the relative magnitude of the electrostatic and van der Waals interactions. The first feature is a minimum in the potential profile, referred to as the secondary minimum. If the secondary minimum energy well is sufficiently deep, two droplets separated by a distance corresponding to the position of the secondary minimum will aggregate. However, the aggregates formed at the secondary minimum are loose and can be easily re-dispersed by simple agitation. The second

characteristic of the potential energy profile is the presence of a maximum, called the energy barrier. The energy barrier is an indication of the stability of the colloidal system: the higher the barrier, the more stable the colloidal system will be. If the barrier is not too high, the droplets or particles may overcome the energy barrier and form stable aggregates at the primary minimum.

The force profile may also show a barrier and/or a secondary minimum, as it is the case for the force profile plotted on Figure 1.4. For the force profiles, however, the barrier and minimum refer respectively to a maximum repulsive force and a maximum attractive force. It should be noted that a negative force corresponds to attraction.

1.5.2.2. Modified DLVO theories

The theory presented above is often referred to as the “classical DLVO theory”. It assumes that the colloidal surfaces are perfectly smooth and uniformly charged. It thus only predicts forces normal to the surface of the interacting bodies. Since real colloids have both chemical and morphological heterogeneities, the DLVO theory fails to explain many experimental results. Therefore, several authors developed theories accounting for surface roughness or surface charge heterogeneity. These authors proved that heterogeneities had an important influence on the interaction profile. An overview of some of the studies made on surface heterogeneity is presented below. Walz [28] provides a more detailed review of these effects. Surprisingly, only one of the studies referred to here investigated both effects simultaneously. In addition, for the most part, the theoretical results were not validated experimentally.

1.5.2.2.1. Effect of Surface Roughness

Czarnecki and Dabros [29] studied the effect of roughness on the van der Waals interaction between a rough particle and a half-space for both the unretarded and retarded case. They modelled the rough particle as a solid core and a rough shell having a radial thickness distribution. Czarnecki and Dabros [29] found that roughness could be accounted for by using a simple correction factor. Their results indicate that the van der Waals attraction energy is attenuated by the roughness, especially at small separations.

Whereas Czarnecki and Dabros [29] concentrated their study on the van der Waals interaction, Suresh and Walz [30] and Bhattacharjee *et al.* [31] studied the total interaction between a rough sphere and a smooth plate. Suresh and Walz [30] modelled the roughness as hemispherical asperities of fixed radius. They found that roughness made the secondary minimum shallower and that this minimum occurred at a larger separation distance than for a smooth sphere. They also realised that the energy barrier was much smaller in presence of roughness. This energy barrier is also seen at larger separation distances than for a smooth sphere. Finally, Suresh and Walz [30] found that roughness had a greater impact on retarded interactions.

Bhattacharjee *et al.* [31] instead modelled the roughness as a uniform sinusoidal surface. To calculate the interaction, they used surface element integration, a technique that allowed them to study not only protruding asperities, but also depressions. They found that for a constant frequency, an increase in the roughness amplitude lowered the energy barrier. The same effect was noted for an increase in frequency at constant amplitude. In addition, the interaction energy of a rough particle and a plate does not exhibit a deep attractive minimum near contact. Bhattacharjee *et al.* [31] also studied the total interaction between two plates, one of them having hemispherical asperities (protrusions and depressions) on its surface. Their study was limited to the unretarded van der Waals interaction and the

electrostatic interaction. Bhattacharjee *et al.* [31] found that for the same surface coverage, an increase in the standard deviation of the size of the protrusions resulted in a smaller repulsive energy barrier or primary maximum. A smaller energy barrier was also found when the surface coverage was increased and the standard deviation remained constant. The authors also showed that for the parameters they used, the effect of roughness was much smaller or even negligible at larger separations. A noteworthy feature of their results is that the potential energy becomes insensitive to the size distribution of the protrusions when the standard deviation is higher than a certain value. Finally, they performed a short study of the orientation effects for the unretarded van der Waals interaction. They concluded that although intrusion (protrusion facing a depression) was energetically favourable, the probability of such an orientation was low.

Herman and Papadopoulos [32] showed that the geometry of the protrusions also had an important effect on the interaction. They used two flat plates, one of them having spherical or conical asperities, on its surface and studied the total interaction (electrostatic and unretarded van der Waals forces) between these two flat plates. For a more complete geometric study, Herman and Papadopoulos [32] used both whole and truncated asperities. They found that the effect of conical asperities was much lower than that of spherical asperities. Their results show that in most cases, spherical asperities should be considered. The results also indicate that surface roughness has a much more significant influence on the double-layer interaction than on the van der Waals interaction.

1.5.2.2.2. Effect of Charge or Potential Heterogeneities

The effect of charge or potential heterogeneities was also the focus of many investigations in the last three decades. Richmond [33] conducted a theoretical investigation of the interaction between two plates having charge heterogeneities. He used a discrete periodic lattice structure using both a smeared out uniform charge

distribution and a square lattice of point charges. Richmond [33] found that for charges of similar sign, the resulting force was always repulsive and that the energy barrier was flattened. However, the magnitude of the repulsion greatly depended on the relative configuration of the lattices. At large separation, the effect of charge irregularities on the interaction became negligible. Richmond [33] also made calculations for the case of equal but opposite charges and found that the free energy of interaction was always attractive at large separations but that at close separation, the free energy of interaction could be attractive or repulsive depending on the configuration of the lattices. As the lattices moved from a perfectly aligned configuration to an offset one, the energy diverged from attractive to repulsive.

The potential energy dependence on orientation was also observed by Kuin [34] when he studied the diffuse layer interaction between two plates having an inhomogeneous surface potential. In his study, Kuin [34] modelled the potential by a two-dimensional Fourier series. To simplify his calculations, Kuin [34] assumed that the surface potential distribution was constant and used a linearised Poisson-Boltzmann equation. He also used the superposition approximation, which is valid for large separation distances only. Kuin [34] averaged the free energy of interaction over all possible relative configurations of the plates. He found that since the local charge increases with periodicity, the attraction at short distances becomes higher as the wavelength of the potential profile decreases. He also found that for small wavelengths the lateral screening was relatively high. Kuin [34] concluded, as did Richmond [33], that for equal size negative and positive patches, the interparticle interaction is always attractive. When small heterogeneities occurred on a uniformly charged plate of opposite charge, the electrostatic interaction showed a maximum. Nevertheless, attraction always occurs at small separation distances.

Experimental validation of Kuin's [34] model was made by Vreeker *et al.* [35] using nickel hydroxy carbonate particles. Vreeker *et al.* [35] found that the dispersions were less stable when the surface potential was heterogeneous due to the additional

attractive forces between the opposite charges. They also showed that their experimental results agree better with their theory than with the DLVO theory.

Miklavic *et al.* [36] used a potential distribution similar to the one used by Vreeker *et al.* [35] to study the total force interaction profile between two plates. However, the treatment used by Miklavic *et al.* [36] is more general since the superposition approximation was not used. In addition, Miklavic *et al.* [36] considered both the constant potential and the constant charge cases. Their results confirmed the already known behaviour of inhomogeneous surfaces, i.e. that the force is attractive for a constant potential and repulsive for a constant charge. At constant potential, Miklavic *et al.* [36] found that the attractive double layer forces coming from the patches could be greater than the van der Waals interaction when the background potential was high. They also found that for two net neutral surfaces, the sign of the interaction energy due to the charge patches depended on the relative alignment of the charges on the plates. Finally, they made a full statistical mechanical average for the case where the charges are free to migrate and found that for large separations, the interaction is always attractive.

1.5.2.2.3. Combined effect of surface roughness and charge heterogeneity

The combined effect of surface roughness and charge heterogeneity has not been frequently studied. Czarniecki and Warszynski [37] studied this effect on the magnitude of tangential forces, which can strongly affect particle deposition. They investigated the resulting net interaction energy (electrostatic and retarded van der Waals) for a system composed of a smooth sphere and a smooth plate on which many small spheres of randomly selected radii were deposited. A Gaussian distribution of potentials was assumed for the deposited spheres. Czarniecki and Warszynski [37] found that tangential forces are determined by surface roughness rather than by heterogeneities in the surface charge distribution or by the alternations in the surface potential values. They concluded that when the separation distance between the

smooth sphere and the plate is of the order of the radii of the small deposited spheres, the tangential forces are of the order of the hydrodynamic force and thus, should be considered.

Based on these studies and on the review made by Walz [28], some general conclusions can be drawn. Although it is clear that surface roughness has a tremendous effect on the interaction, the magnitude of this effect depends strongly on the geometry of the surface asperities, which is not always well known. Qualitatively, surface roughness affects both the energy barrier and the secondary energy minimum by making them smaller. It is particularly true for the energy barrier, which can be lowered by orders of magnitude. Although the effect of surface roughness on the van der Waals contribution becomes insignificant at large separation distances, its effect on the electrostatic interaction does not seem to disappear.

Charge heterogeneities also affect the behaviour of colloidal systems, by changing the electrostatic contribution. The effect of discrete charge sites is smeared out when the separation between the surfaces becomes greater than the characteristic spacing between the charges. The influence of charge heterogeneities depends on the orientation of the charge heterogeneities. However, averaging over all possible orientations greatly reduces the magnitude of the electrostatic force. When the net surface charge is zero, the orientation averaging always yields an attractive force. For colloidal dispersions, a distribution in potential or charge lowers the stability. The same effect is seen in deposition experiments, where the deposition rate can be increased by orders of magnitude when charge heterogeneities are present. In both cases, non-uniformity in charge or potential makes the colloidal forces less sensitive to a variation of ionic strength.

1.5.3. Colloidal Force Measurement Techniques

The stability of emulsions is directly related to the interaction forces between the emulsified droplets. The same can be said for deposition where particles interact with a collector. Measuring colloidal forces is thus a good way to monitor the stability of emulsions and dispersions. Hence, many colloidal force measurement techniques were developed over the last three decades. A brief overview of several force measurement techniques is provided in Table 1.1.

Among these force measurement techniques, the surface force apparatus [38, 39, 40] and atomic force microscopy [41, 42] are the most commonly used. However, neither of these two techniques is sufficiently sensitive to measure the force close to the secondary minimum, an important point for stability studies. In addition, the surface force apparatus [38, 39, 40] uses two macroscopic surfaces to measure the force and does not involve colloidal bodies. Although the atomic force microscope [41, 42] can measure the force between a colloidal particle and a surface as well as the force between two colloidal particles, one of the colloidal particles must be glued to the tip of the probe. In addition, the other particle must be deposited on a surface to measure the interaction force between two particles. This impedes its applicability for bitumen in water emulsions.

Total internal reflection microscopy [43], evanescent wave scattering [44] and reflection interference contrast microscopy [45] show better promises in terms of their sensitivity. However, all these techniques measure the force between a particle and a flat glass wall, meaning that only one body is of colloidal dimensions. In addition, these force measurement techniques can only allow the study of static interactions. Finally, the particle has to have an index of refraction different from that of the solution.

The osmotic pressure technique [46], the Kossel diffraction technique [47], the capillary technique [48] and the optical tweezers [49] can be applied to two particles. However, their characteristics make them unsuitable for bitumen-in-water emulsions. The differential electrophoresis technique [50] can be applied to emulsions but the zeta potential of the two droplets must be different, which is not the case for bitumen emulsions for which the zeta potential is relatively constant.

The travelling microtube techniques for particle-particle collisions [51, 52] and for doublet break-ups [53] could be used for this study. However, particles or droplets are submitted to a Poiseuille capillary flow and tend to move away from the same focal plane, resulting in errors. In addition, the chance of observing particle collisions or doublet break-ups in a microtube is very low. Colloidal particle scattering [54] and hydrodynamic force balance [9] share the same basic principles as the two previous techniques but instead of using a capillary flow, they submit the particles or droplets to a wall shear flow. This wall shear flow provides a better control of the interaction between the particles or droplets and thus, improves the results in both quality and quantity. Therefore, the colloidal particle scattering and hydrodynamic force balance techniques were used for this study. Detailed principles and experimental procedures are described in Chapter 2.

1.5.4. Previous Studies of Bitumen-in-Water Emulsions

Very few studies exist on the interaction forces between colloidal bitumen droplets in water. Among these few studies is an investigation made by Salou *et al.* [55]. They measured the zeta potential, determined the radius of the bitumen droplets and calculated the Hamaker constant from the critical coagulation concentration. Using these three parameters, Salou *et al.* [55] calculated the potential energy profile from the classical DLVO theory and from what they called an extended DLVO theory accounting for the hydrophilic and hydrophobic interaction energies. They found that a bitumen having a high resin to asphaltene ratio tended to give stable emulsions,

whereas a bitumen having a low resin to asphaltene ratio gave unstable emulsions. However, their results were obtained in a strongly acidic environment, unlike the plant conditions used in oil sands extraction.

Wu *et al.* [6, 9] studied the interaction between bitumen droplets in water using colloidal particle scattering [6] and hydrodynamic force balance [9]. In reference [6], they used different electrolyte concentrations at a pH of 7 to study the resulting repulsive force between the bitumen droplets. Wu *et al.* [6] found that the main stability mechanism was electrostatic repulsion. They also showed that bitumen droplets had isolated protrusions that further increased the electrostatic repulsion. Wu *et al.* [9] supplemented the previous study [6] by measuring the maximum attractive force around the secondary minimum and found that again protrusions enhanced the electrostatic repulsion or reduced the van der Waals attraction. In another study, Wu *et al.* [10] measured the maximum attractive force for filtered bitumen and showed that the surface of the filtered bitumen droplets was smoother.

Many aspects of the stability of bitumen-in-water emulsions are still not completely understood. This thesis was compiled with the expectation of gaining a better understanding of the factors governing the interaction between colloidal bitumen droplets. The study focuses mostly on experimental results and uses previously developed models [6, 9, 10] to interpret these results.

Since asphaltenes are believed to play an important role in the stability of bitumen emulsions [56], the first part of this thesis will compare the interaction forces between deasphalted bitumen droplets and between bitumen droplets in an aqueous solution containing potassium chloride.

The interaction force obtained between bitumen droplets in the presence of potassium chloride will then be compared to the interaction force obtained for bitumen droplets

in a mixed sodium chloride and sodium bicarbonate solution. The goal of this aspect of the thesis is to investigate the effects of pH and different electrolytes.

Finally, the effect of clays will be investigated by adding asphaltenes-treated clays to the bitumen-in-water emulsion. A combination of sodium chloride and sodium bicarbonate will be used as the electrolyte.

For a more comprehensive study, both the colloidal particle scattering and the hydrodynamic force balance techniques will be used. Finally, different colloidal force models will be applied to the experimental data and their validity will be discussed. The experimental data interpreted based on these force models reveal useful information such as the value of the Hamaker constant of bitumen-water-bitumen and the surface roughness characteristics of a bitumen droplet.

Chapter 2 gives detailed information on the experimental procedures and techniques involved in this study. The results obtained from colloidal particle scattering and from hydrodynamic force balance are included in two different chapters (Chapters 3 and 4) to account for the particularities of each technique. Chapter 5 provides a reconciliation of the results obtained from the two methods. Chapter 5 summarises the most important findings of this research and emphasises the need for further research.

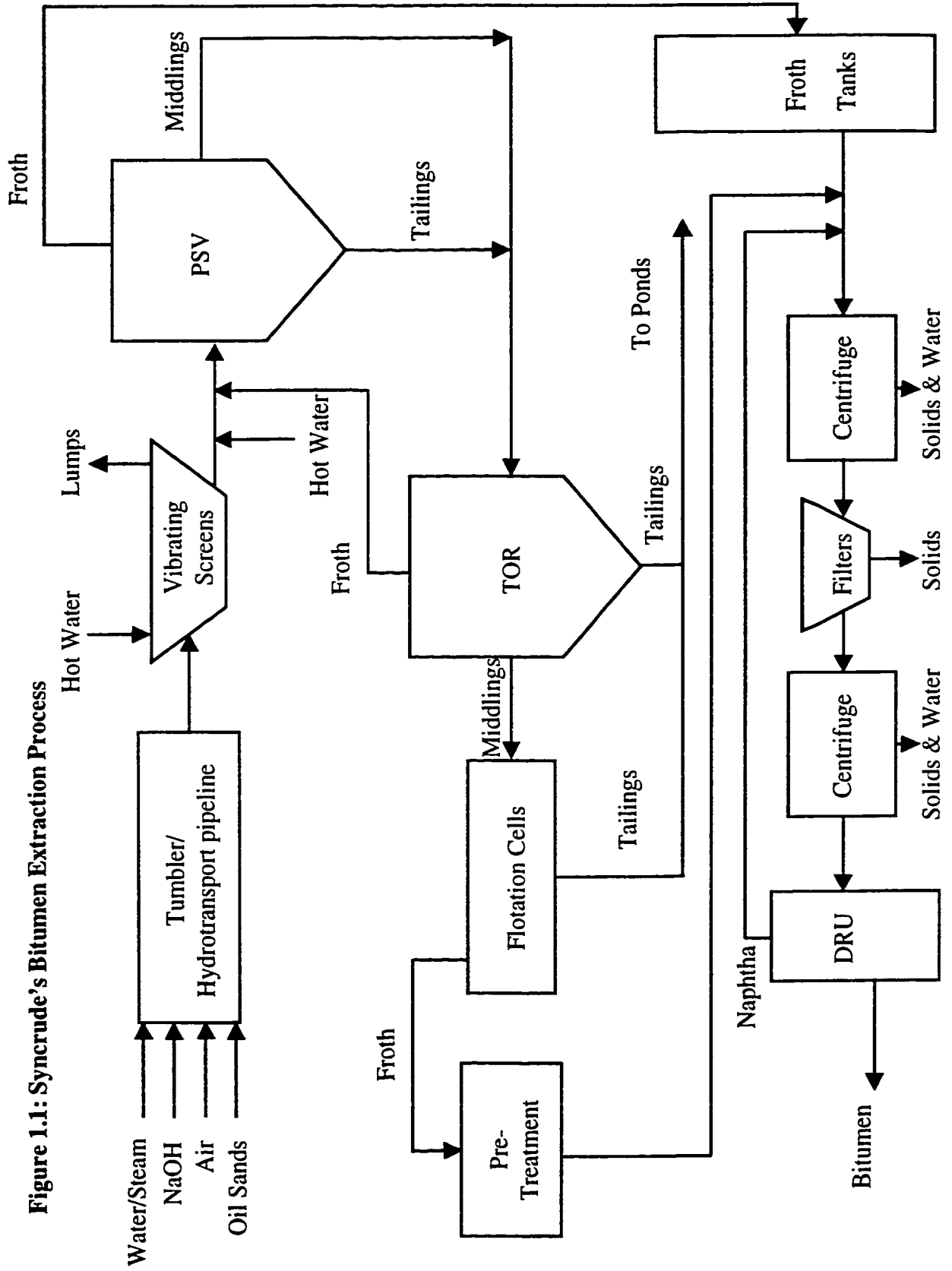


Figure 1.1: Syncrude's Bitumen Extraction Process

Figure 1.2.: Stern Model for the Diffuse Electric Layer

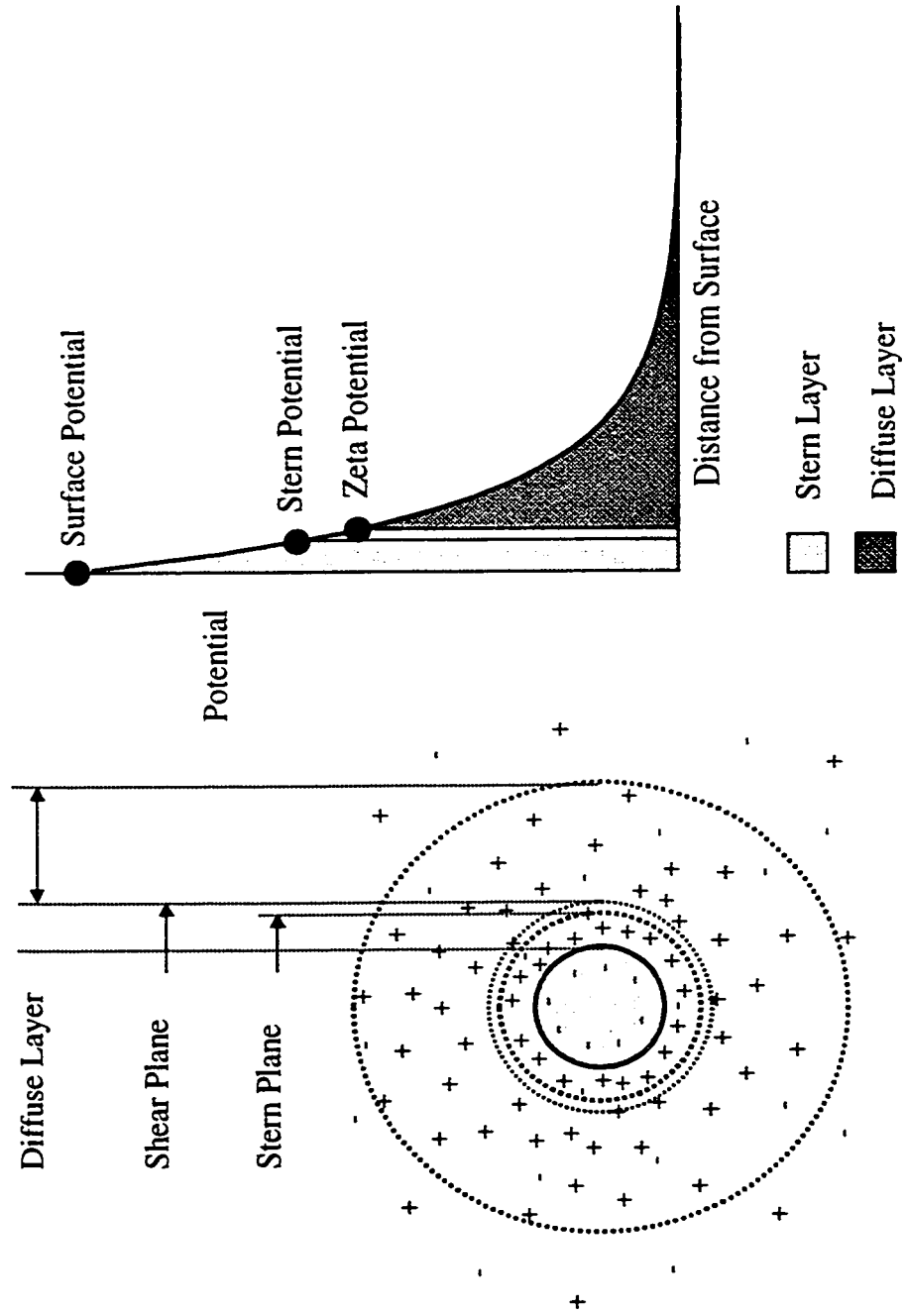


Figure 1.3: Steric Force Model

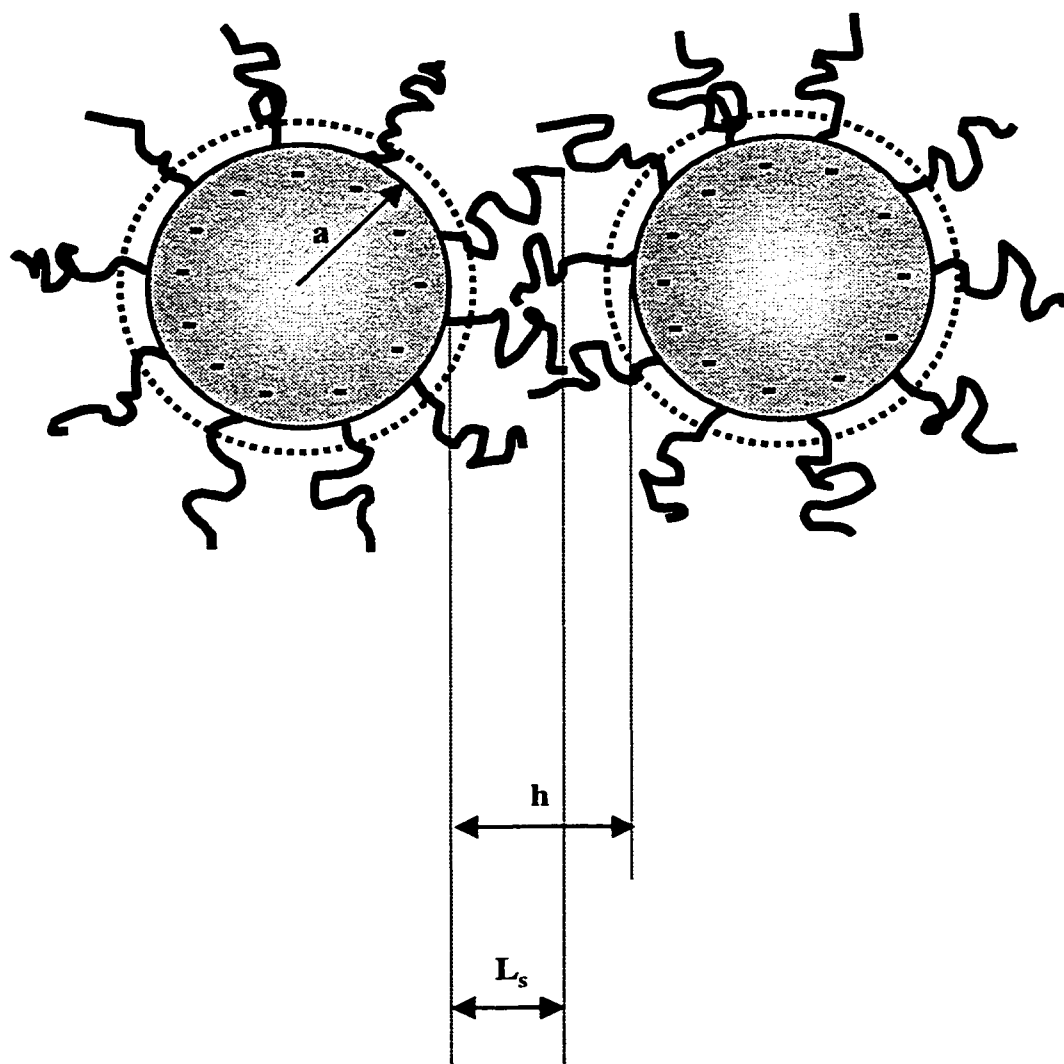


Figure 1.4: Typical Force and Energy Graphs

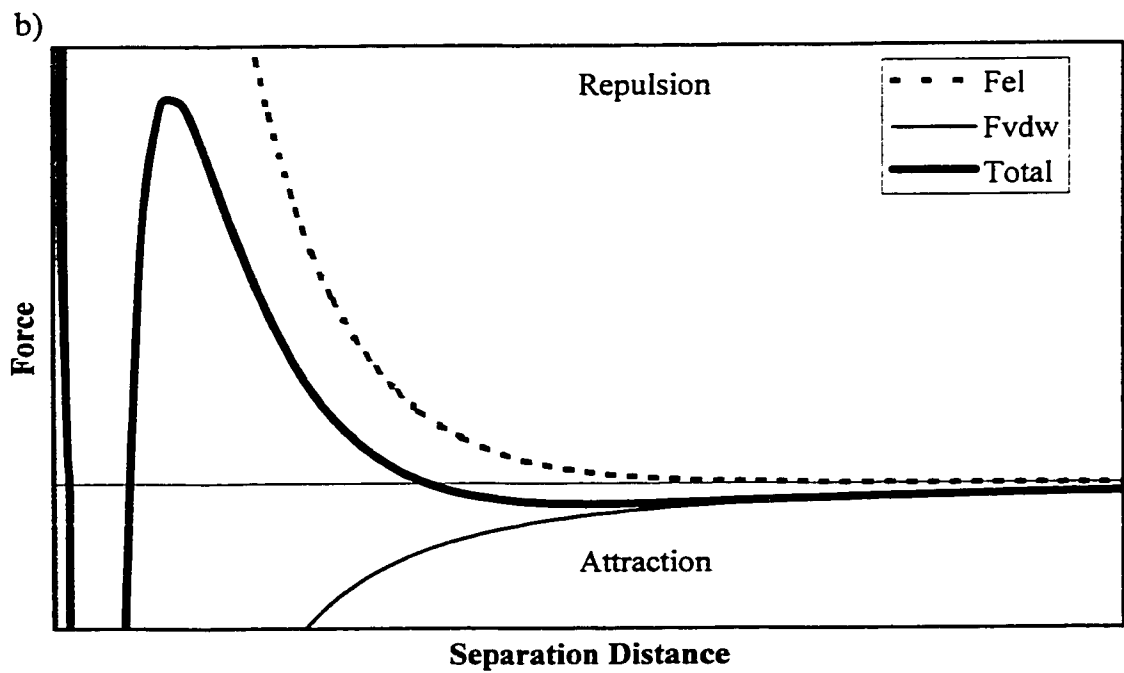
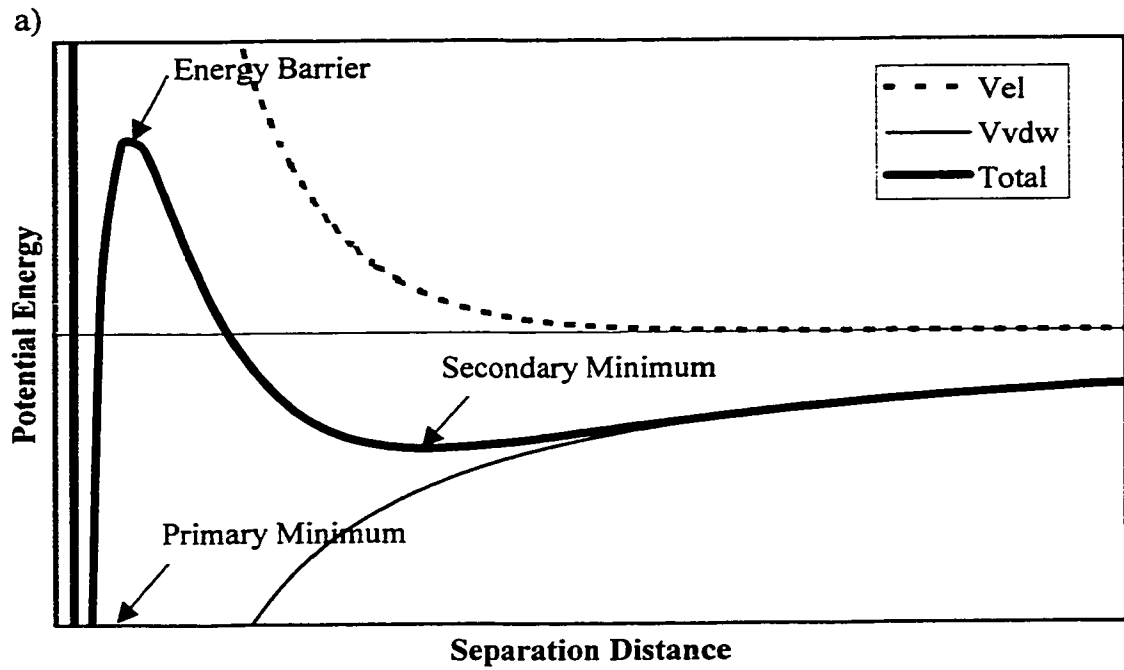


Table 1.1: Summary of Force Measurement Techniques

Technique	Surface Force Apparatus ^{38,39,40}	Atomic Force Microscope ^{41,42}	Total Internal Reflection Microscopy ⁴³
Surfaces Involved	Two crossed mica cylinders	Particle glued to probe and flat plate; Particle glued to probe and particle deposited	Spherical particle and glass plate
Basic Principle	Force measured by deflection of a cantilever and distance measured by multiple beam interference fringes	Deflection of a cantilever beam having a ultra-small mass	Light scattering
Applicability	<ul style="list-style-type: none"> - Direct measurement of various forces - Possibility of coating the mica cylinders with substrates - Gas or liquid medium 	<ul style="list-style-type: none"> - Direct measurement of various forces - Determination of force profile 	<ul style="list-style-type: none"> - Measurement of weak forces - Brownian motion studies - Weight determination of single microscopic sphere - Reversible adsorption dynamics
Colloid Dimensions	Crossed macroscopic cylinders of radii of curvature of ≈ 1 cm	Micron size	$> 1-5 \mu\text{m}$
Sensitivity	Distance: < 0.1 nm Force: 10 nm	Distance: sub-nm Force: sub- nN	Distance: 1 nm Force: sub-nN
Interaction Mode	Static, Dynamic	Static	Static
Limitations	<ul style="list-style-type: none"> - Force between macroscopic surfaces - Smooths short-range forces - Not sensitive enough for force close to secondary minimum - Substrate must be semi-transparent 	<ul style="list-style-type: none"> - Not sensitive enough for force close to secondary minimum - Oscillations of the cantilever may lead to an apparent hysteresis - Difficulty in measuring long-range interactions 	<ul style="list-style-type: none"> - Only gives relative changes in distance \Rightarrow relative potential only - Limited to large, spherical, non adsorbing particles whose index of refraction differs from the solution - Only one colloidal surface - Direct measurement of part of the profile only

Technique	Travelling Microtube for Particle Collisions ^{51,52}	Colloidal Particle Scattering ⁵⁴	Osmotic Pressure ⁴⁶
Surfaces Involved	Colloidal Particles or Aggregates	2 spherical particles or droplets	Colloidal Particles
Basic Principle	Interaction of spherical particles in a Poiseuille capillary flow	Trajectory inversion of collisions in a wall shear flow	Interaction from osmotic pressure and packing structure
Applicability	<ul style="list-style-type: none"> - Interaction force of 2 particles - Aggregation studies - Discriminating primary and secondary doublet - Determination of separation distance in a secondary doublet 	<ul style="list-style-type: none"> - Dilute suspensions and emulsions - Interaction around the secondary minimum 	<ul style="list-style-type: none"> - Electrostatically stabilised monodispersed and concentrated dispersions - Indirect determination of interaction profile - Very small particles
Colloid Dimensions	≈ 4 to $10\ \mu\text{m}$	≈ 4 to $10\ \mu\text{m}$	Submicron size or smaller
Sensitivity	10^{-13} N	10^{-13} N	Not available
Interaction Mode	Dynamic	Dynamic	Static
Limitations	<ul style="list-style-type: none"> - Results depend on a force model and on hydrodynamic calculations - Particles must be in the same focal plane and have a low relative velocity - Only 10% of the encounters result in true collisions - Extremely time-consuming 	<ul style="list-style-type: none"> - Limited to repulsion-dominant systems - Profile determination depends on the model assumed and on hydrodynamic calculations - Neutral buoyancy of particles required - At least two equal-sized droplets required - Time-consuming 	<ul style="list-style-type: none"> - Takes days to reach the osmotic equilibrium - Dispersion must be concentrated - Force profile depends on the assumed crystal model whereas real concentrated suspensions contain both ordered and disordered structures

Technique	Capillary Technique ⁴⁸	Evanescent Wave Scattering ⁴⁴	Reflection Interference Contrast Microscopy ⁴⁵
Surfaces Involved	Particles	Particle and flat plate	Spherical particle and flat plate
Basic Principle	Capillary pressure between two approaching meniscuses using the light differential interferometric technique	Light scattering	Light scattering: absolute distance found from changes of interference fringe pattern (Newtonian rings)
Applicability	<ul style="list-style-type: none"> - Interaction between coarse and fine particles in concentrated dispersions - Non-spherical particles - Polydispersity in size - Structural or depletion contribution 	<ul style="list-style-type: none"> - Direct measurement of forces - Brownian motion studies - Deposition of submicroscopic particles 	<ul style="list-style-type: none"> - Direct measurement of forces - Brownian motion studies - Absolute distance dependence of the potential around the potential minimum - Hydrodynamic friction measurement
Colloid Dimensions	Micron and submicron size	Micron size	Micron size
Sensitivity	Not available	Not available, probably identical to total internal reflection microscopy	Distance: 1 nm Force: For latex: 10^{-12} N For giant vesicles: 10^{-15} N
Interaction Mode	Dynamic	Static	Static
Limitations	<ul style="list-style-type: none"> - Only provides the threshold capillary pressure and not the complete force profile 	<ul style="list-style-type: none"> - Data not sufficiently accurate to obtain the particle concentration profile near the wall directly from the scattering data - Direct measurement of part of the profile only - Only one colloidal surface 	<ul style="list-style-type: none"> - Particle must be spherical - Repulsive interaction only - Direct measurement of part of the profile only - Only one colloidal surface

Technique	Optical Tweezers ⁴⁹	Travelling Microtube for doublet break-up ⁵³	Hydrodynamic Force Balance ⁹
Surfaces Involved	1 spherical particle, 2 spherical particles or one particle and a wall	2 spherical particles	2 spherical particles/droplets
Basic Principle	Radiation pressure of laser beams traps particles and controls their movement. Displacement measured from light scattering	Break-up of a doublet made of rigid spheres by an accelerating capillary flow	Secondary doublet break-up by an increasing wall shear flow
Applicability	<ul style="list-style-type: none"> - Force from trajectories obtained by turning on/off the tweezers - Single particle dynamics - Determination of diffusion coefficient 	<ul style="list-style-type: none"> - To track rotation and translation displacements of a doublet in a capillary flow - Biological systems 	<ul style="list-style-type: none"> - Determination of maximum attractive force in an energy minimum - Dilute emulsions and suspensions
Colloid Dimensions	Nanometer to micron size	≈ 4 to $10 \mu\text{m}$	≈ 4 to $10 \mu\text{m}$
Sensitivity	Not available	Probably 10^{-12} N	Force: 10^{-13} N
Interaction Mode	Dynamic	Dynamic	Dynamic
Limitations	<ul style="list-style-type: none"> - Agreement between theories of optical trapping and experimental force measurements is generally unsatisfactory 	<ul style="list-style-type: none"> - Particles must be spherical - Deviation from the medium plane results in considerable error in radial distance measurement - Determination of attractive force in an individual doublet is not possible (Only forces range or mean forces were measured) 	<ul style="list-style-type: none"> - Attraction-dominant systems only - Limited to secondary doublets with a maximum attractive force in the range of 10^{-13} to 10^{-11} N - At least two equal-sized droplets required

Technique	Differential Electrophoresis ⁵⁰	Kossel Diffraction Technique ⁴⁷
Surfaces Involved	2 spherical particles/droplets	Spherical particles
Basic Principle	Electrophoretic translation and rotation of a doublet	Back-light scattering, Kossel diffraction
Applicability	<ul style="list-style-type: none"> - Determination of normal and tangential forces between two particles in a doublet - Determination of primary or secondary doublet 	<ul style="list-style-type: none"> - Determination of energy profile for colloidal dispersions - Polydispersed systems
Colloid Dimensions	Micron size	Submicron size
Sensitivity	Not available	Not available
Interaction Mode	Dynamic	Static
Limitations	- The particles/droplets must have different zeta potentials	

CHAPTER 2

EXPERIMENTAL

2.1. Materials

The bitumen used was a topped-bitumen (also referred to in the oil sands industry as a coker-feed bitumen) extracted by Syncrude Canada Ltd. from the Athabasca oil sands deposit. No solids were removed prior to its utilisation. The topped-bitumen has a density of approximately 1020 kg/m^3 at ambient temperature.

Kaolinite forms the major part of clays in oil sands. Therefore, a commercial grade of kaolinite was used in the experiments, namely ECCA-TEX 510 provided by ECC International – Performance Minerals. The mean particle size was $0.3 \text{ }\mu\text{m}$, with 92% of the particles smaller than $2 \text{ }\mu\text{m}$. Kaolinite ECCA-TEX 510 contains mostly SiO_2 (45.0%) and Al_2O_3 (38.4%).

Asphaltenes were obtained from the topped-bitumen, following a procedure described in section 2.3.

Three different electrolytes were used for this study. Potassium chloride was the most commonly used and was an A.C.S. certified reagent, supplied by Sigma-Aldrich Chemical Co. The purity of the potassium chloride used is assessed at 100.0%. In some experiments, sodium chloride and sodium bicarbonate were used instead of potassium chloride. Sodium chloride was obtained from BDH Inc. and was an A.C.S. certified analytical reagent having a minimum assay of 99.0%. Sodium bicarbonate was provided by Fisher Scientific and its purity is assessed at 99.9% or better.

Deuterium oxide (D_2O) was used as a density regulator. It was supplied by Acros Organics and had a density of 1100 kg/m^3 and at least 99.8% deuterium atoms.

Finally, all solutions and emulsions were prepared using de-ionised ultra-filtered water, supplied by Fisher Scientific.

2.2. Equipment

2.2.1. Microcollider

All the results presented in this thesis were performed using a surface collision apparatus [54], later called a microcollider [6]. Figure 2.1 gives a schematic representation of the experimental set-up. In this apparatus, a x-y motorised stage (Newport UTM50CC.5HA) supports a sample cell made from a flat mirror bottom and four glass walls. The solution of interest is poured into this cell. A steel cylindrical tube with a glass plate glued at its bottom is partially immersed into the sample solution. This cylindrical tube is firmly held in place by a holder. The gap width between the top surface of the flat mirror and the bottom surface of the glued glass plate can be adjusted by lowering or raising the motorised stage. A gap width of $120 \mu\text{m}$ is preferred to minimise flow oscillation.

Two independent motors control the x-y motorised stage. Since the top glass plate is stationary, any displacement of the motors would move the mirror plate whereby creating a wall shear flow in the gap. Since the gap width is of a fixed value, the shear rate will be directly related to the velocities of the motorised stage. The moving stage can be controlled either by a joystick or by a Pentium computer. The joystick is used to locate the droplets whereas only the computer is used during an experimental run.

A microscope is used to monitor the movement of the emulsion droplets. The microscope objective is placed above the glass surface of the cylindrical tube and can be raised or lowered to adjust the focal plane. Displacement of the droplets is recorded by a CCD video camera (SONY DXC-950) and a VCR (SONY SVO-9500MD). The computer, through a software, also controls the VCR to ensure synchronisation of the recording. In addition, the computer is equipped with a frame grabber (Imaging Technology IC-PCI/AM-CLR) to digitise video images.

During an experimental run, the computer controls the direction of movement and the velocity of the motorised stage. The movement of the lower stage generates a displacement of the emulsion droplets. The displacement of the droplets is magnified by the microscope, recorded by the camera and stored on a videocassette using the VCR. At the same time, the computer stores the time, at which the image was recorded, as well as the velocity of the motorised stage. The images recorded are later analysed using the frame grabber and appropriate software kindly provided by Dr. Alex Wu and Syncrude Canada Ltd.

2.2.2. Micro-Electrophoresis Apparatus

The zeta potential of the emulsified bitumen droplets was measured with a commercial micro-electrophoresis apparatus (Lazer Zee Meter™ Model 501) from Pen Kem Inc. A rotating prism coupled with a video monitor allowed easy determination of the zeta potential through a digital reading. The electrophoresis apparatus is equipped with a rectangular cell having a depth of 1.5 mm and a width of 15 mm. The electrodes are made of molybdenum (anode) and plated-palladium (cathode). This micro-electrophoresis equipment can measure zeta potential values from -100 mV to 100 mV with accuracy within 5%. To neglect any electro-osmotic effect, measurements were taken at the stationary flow planes.

2.3. Manipulations

To homogenise the bitumen, it was heated at 80 °C for 30 minutes and stirred every 2 minutes during the heating period. It was then placed in a dark bottle to minimise any potential ageing from light exposure.

Emulsions were prepared by spreading a thin layer of bitumen (about 0.4 to 0.5 g) onto the bottom of a 20-ml vial and adding approximately 10 ml of solution. The closed vial was then placed into a sonicator bath containing water at 60 ± 3 °C for 80 seconds. This procedure created an emulsion of droplets having a diameter in the range of 4 to 8 microns.

Deasphalted bitumen was prepared by removing the asphaltenes, using *n*-heptane. The weight ratio of *n*-heptane to bitumen was 40:1, corresponding to a volume ratio of roughly 60:1. Although some authors [56] used a lower ratio, Speight and Moschopedis [58] stated that, by definition, asphaltenes belong in “a solubility class that is precipitated from petroleum and bitumens by the addition of a minimum of forty volumes of the liquid hydrocarbon”². In fact, the 1996 ASTM Book of Standards [59] even suggests adding 100 mL of *n*-heptane per 1 g of bitumen.

The *n*-heptane-bitumen mixture was stirred until all bitumen was dissolved and left undisturbed for two hours. The mixture was then filtered with a 25-nm filter and left to dry for at least 48 hours, until all solvent evaporated. The solids (asphaltenes) obtained were rinsed three times with *n*-heptane and dried at room temperature, before being used to treat clays.

Asphaltene-treated clays were prepared using a method similar to that described by Yan and Masliyah [57]. First, 1.0 g of kaolinite clay was added to approximately 100

² The definition was taken from the 1975 ASTM Book of Standards.

ml of a heptol³ solution containing 1g/L of asphaltenes. The solution was left aside for 24 hours, with occasional stirring. It was then centrifuged for 10 minutes. The treated-clay was recovered, cleaned with pure heptol and centrifuged for another 10 minutes. Finally, the clay particles were left to dry before being stored. Based on the results of Yan and Masliyah [57], the asphaltenes concentration used should give a contact angle of 125 to 130°, making the clay hydrophobic. Since the only goal of this study is to have hydrophobic clays that will attach to bitumen, no measurement was made to verify the exact value of the contact angle.

2.4. Experimental Methods

The microcollider apparatus described in section 2.2.1 can operate in two different modes referred to as “Colloidal Particle Scattering (CPS)” [6, 54] and “Hydrodynamic Force Balance (HFB)” [9]. CPS and HFB are two complementary techniques to measure the colloidal forces between a pair of droplets. The former technique is used when the droplets repel, or very slightly attract, each other, whereas the hydrodynamic force balance method can only be used when there is sufficient attraction between the pair of droplets.

2.4.1. Colloidal Particle Scattering

The colloidal particle scattering (CPS) technique was developed at McGill University (Montreal, Canada) in 1994 by van de Ven *et al.* [54] to determine the colloidal forces between two individual particles by observing their collision trajectories in a low Reynolds number flow. The CPS technique is especially useful in determining the interaction forces between liquid droplets, which pose a challenge to force measurement. Colloidal particle scattering also has the advantage of being able to measure the dynamic interaction between colloidal particles. In addition, it is a

³ Heptol is a 1:1 volume mixture of n-heptane and toluene.

sensitive technique that can detect forces corresponding to energies of a single kT . This sensitivity makes the determination of the force-distance profile near the secondary minimum possible.

van de Ven *et al.* [54] provided the detailed principles of colloidal particle scattering. The emulsions to be studied are first poured into the cell of the microcollider. The solution used has to have a slightly higher density ($\approx 10 \text{ kg/m}^3$) than the colloidal droplets. The small buoyancy force makes the droplets rise slowly towards the glass surface. Because of the short duration of an experimental run (roughly 1 to 4 seconds), this buoyancy force has no effect on the results. After a few minutes, some droplets are fixed to the top glass surface and cannot be displaced by the low hydrodynamic forces used. Once such a stationary droplet is located, the motorised-stage is moved until a mobile droplet of equal size is found and positioned close to the fixed one. It is sometimes necessary to wait a few minutes until the mobile droplet becomes close enough to the top glass surface.

Once the droplets are well positioned they are forced to collide a number of times (typically 200 to 300 times) by making the mobile droplet go around the stationary droplet using a wall shear flow generated by the displacement of the motorised stage. A representation of such a collision⁴ is provided by Figure 2.2. In this figure, the stationary droplet corresponds to droplet B. At first, the mobile droplet is located far from the stationary one, as indicated by droplet C, on the left side of Figure 2.2. The initial position of its centre is projected on a plane normally referred to as a “scattering diagram”. A scattering diagram for the collision presented in Figure 2.2 is shown at the far right of the figure. A detailed description of this diagram will be given shortly. During an experimental run, the mobile droplet moves towards the stationary droplet and glides around it. Once past the fixed droplet, it realigns with

⁴ Although the instrument used in this technique is called “microcollider”, the word “collision” is different from the common meaning implying surface contact. In this experiment, the two droplets do not actually touch each other in the process but rather remain separated at all times by a layer of solution of several nanometers.

the flow. Far from the stationary droplet, the mobile droplet resumes its straight trajectory, moving parallel to the glass surface. From this straight trajectory, the final position can be obtained, as indicated on the figure by the droplet D, at the right. As it can be observed from Figure 2.2, this final position is also projected on the scattering diagram. In addition, the projection of the stationary droplet on the scattering diagram is shown by the dotted circle. The shaded part of the scattering diagram corresponds to a part that cannot be occupied by the centre of the mobile droplet since the droplets are of nearly equal size and non-deformable [6]. Therefore, this region is not indicated on any of the scattering diagrams presented in this study. It should be noted that the scattering diagrams that will be shown in Chapter 3 are inverted for easy reading.

As it was mentioned earlier, the colloidal force is obtained by observing the trajectory followed by the mobile droplet during a collision. If there is no colloidal interaction between the two droplets, the trajectory followed by the mobile droplet will be symmetrical with respect to the stationary droplet. This symmetric trajectory is represented on Figure 2.3 by a dotted line. On the other hand, if there is a colloidal interaction between the droplets, there will be a deflection in the path followed by the mobile droplet, as shown by the solid line. The degree of asymmetry in the trajectory is an indication of the magnitude of the interaction force.

The force profile is obtained by a procedure called trajectory inversion. First, a force-distance relationship (e.g. DLVO theory) including adjustable parameters is assumed. The parameters giving the best fit of the collision trajectory are then used to plot the force profile. In Figure 2.3, a theoretically calculated trajectory using a certain force model is given by a dashed line. If the model is a perfect representation of the interaction, the experimental and the theoretical trajectories should be indistinguishable. However, due to Brownian motion and experimental errors, deviations are likely to occur. Therefore, many experimental trajectories are needed to minimise the error.

Results obtained with colloidal particle scattering are plotted on a scattering diagram, which gives a cross-sectional representation of what happens during a collision. A typical scattering diagram is provided in Figure 2.4. As it was mentioned before, the half-circle on the diagram is the projection of the lower half of the stationary droplet shown in Figure 2.2. The x-axis represents the lateral position with respect to the stationary droplet whereas the z-axis represents the depth of the centre of the mobile droplet. This z-axis has its origin at the glass surface. On a scattering diagram, the initial and final positions of the centre of the mobile droplet are indicated respectively by open (white) circles and filled (black) circles. Some of the pairs of initial/final positions are numbered and joined by arrows on Figure 2.4 for a clearer understanding. Numbers and arrows are usually not provided in typical scattering diagrams. The locations of the final experimental positions yield important information on the interaction. The farther a final position of the mobile droplet from the stationary droplet, the more repulsive the interaction.

In Figure 2.4, the grey filled triangles are the theoretical final positions calculated from an assumed model following a procedure that will be described shortly. As it can be observed from Figure 2.4, the theoretical final positions form a ring. Again, if the theoretical model is a perfect representation, the experimental final positions will be identical to the theoretical final positions. Therefore, it can easily be judged only by looking at a scattering diagram whether or not the model assumed is adequate. It should be noted that all values presented in a scattering diagram are scaled by dividing each coordinate by the average radius of the droplets.

The basic principles of trajectory inversion are provided by van de Ven *et al.* [54] and Dabros and van de Ven [60]. Trajectory inversion consists of solving the trajectory equation along with the hydrodynamic and colloidal force equations. Only the main characteristics of the calculations are presented here. If the Brownian

motion of the mobile particle is neglected, the trajectory equation can be written as [54]:

$$\frac{d\mathbf{r}}{dt} = \mathbf{M} \cdot (\mathbf{F}_{\text{hydr}} + \mathbf{F}_{\text{colloidal}}) \quad (2.1)$$

where \mathbf{r} is the position vector of the centre of the mobile droplet, \mathbf{F}_{hydr} is the hydrodynamic driving force, $\mathbf{F}_{\text{colloidal}}$ is the colloidal interaction force and \mathbf{M} is the mobility tensor.

Since the Reynolds number is very low ($Re \ll 1$) for most colloidal systems, inertia is negligible. Therefore, the mobility tensor and the hydrodynamic force can be calculated using the Stokes equation for creeping flow rather than the full Navier-Stokes equation.

Equation 2.1 provides the relative position of the mobile droplet with time. Thus, to calculate the absolute final position, it is only necessary to know the absolute initial position and to solve the differential equation.

Figure 2.5 summarises the calculation procedure. The first step is to numerically solve the Stokes and the continuity equations, accounting for the wall, the fixed droplet and the mobile droplet at its initial position. This provides the hydrodynamic driving force that would act on the mobile sphere if it were held stationary in the flow. The initial position was defined as the position at which the distance between the two droplets (before collision) is equal to six times the radius of the droplets. The initial position was chosen because the path followed by the droplet beyond this position is not affected by the presence of the stationary droplet. The Stokes and continuity equations are given by [54]:

$$\begin{aligned}\mu \nabla^2 \mathbf{v} &= \nabla p \\ \nabla \cdot \mathbf{v} &= 0\end{aligned}\tag{2.2}$$

where \mathbf{v} is the fluid velocity vector and p is the pressure.

For two solid particles and a wall boundary, the solution of these equations is given by [54]:

$$\mathbf{v}(\mathbf{x}) = \mathbf{v}^0(\mathbf{x}) + \sum_{j=1}^2 \int_{\mathcal{S}_j} \boldsymbol{\tau}(\mathbf{x}, \mathbf{y}) \cdot \mathbf{f}(\mathbf{y}) d\mathcal{S}(\mathbf{y})\tag{2.3}$$

In this expression, $\mathbf{v}(\mathbf{x})$ is the fluid velocity vector at point \mathbf{x} , $\mathbf{v}^0(\mathbf{x})$ is the undisturbed flow field, $\mathbf{f}(\mathbf{y})$ is the force per unit area at a point \mathbf{y} of the particle surface, $\boldsymbol{\tau}$ is the Oseen tensor and \mathcal{S} is the surface of a particle. The summation sign indicates that the integral has to be calculated over the surface of the two particles.

Note that the conservation of energy equation is not needed because the process is isothermal.

The total force, \mathbf{F}_j , and torque, \mathbf{T}_j , exerted on the fluid by particle j are [54]:

$$\begin{aligned}\mathbf{F}_j &= \int_{\mathcal{S}_j} \mathbf{f}(\mathbf{y}) d\mathcal{S}(\mathbf{y}) \\ \mathbf{T}_j &= \int_{\mathcal{S}_j} (\mathbf{y} - \mathbf{r}_j) \mathbf{f}(\mathbf{y}) d\mathcal{S}(\mathbf{y})\end{aligned}\tag{2.4}$$

where \mathbf{r}_j is the position vector of the centre of the spherical particle j .

Although this solution was derived for solid spherical particles, it can also be used for liquid bitumen droplets in this study inasmuch as the no-slip boundary conditions are still valid and the bitumen droplets are not deformable. For the bitumen droplets

used, both conditions are satisfied [10] and thus, the colloidal particle scattering technique can be used in the present study.

The hydrodynamic equations can be reduced to a discrete form, allowing the forces to be calculated by the multisubunit method. In this method, each particle is represented by discrete points to which an appropriate Stokes radius is assigned. The main advantage of this technique is that no integration over surface elements is needed. In addition, when the moving particle is very close to the stationary particle or the wall, an asymptotic analytical lubrication theory is used to improve the results. In other words, when the mobile particle is farther than a given limit, the hydrodynamic forces are found based on the multisubunit method [cf. ref. 60] only. When the particle is within that limit, the same procedure is used but the mobility tensor elements are determined by a cubic splines interpolation method, considering both the numerical and analytical solutions.

The mobility tensor, \mathbf{M} , depends on the geometry of the system and on the viscosity of the fluid. For the system presented here, its elements can be determined by the response of a droplet to a unit force and torque in a quiescent fluid. Detailed calculations for the mobility tensor elements are provided by Dabros and van de Ven [60].

The next step in solving the trajectory equation requires the calculation of the hydrodynamic resistance force, $\mathbf{F}_{\text{resist}}$. The force is obtained from a force balance given by:

$$\mathbf{F}_{\text{resist}} = \mathbf{F}_{\text{hydr}} + \mathbf{F}_{\text{colloidal}} \quad (2.5)$$

The resistance force, i.e. the drag force exerted upon the mobile droplet in a quiescent fluid, is related to the mobile sphere velocity, \mathbf{u} , (calculated at the centre of the sphere) by the expression:

$$\mathbf{F}_{resist} = \mathbf{M}^{-1} \cdot \mathbf{u} \quad (2.6)$$

In Equation 2.6, $\mathbf{F}_{resist} = (f_1, f_2, f_3, t_1, t_2, t_3)$ and $\mathbf{u} = (u_1, u_2, u_3, w_1, w_2, w_3)$ where f_i are the forces, t_i are the torques, u_i are the translational velocities and w_i are the angular velocities. From Equation 2.6, it is obvious that the velocity of the moving droplet can be found by [54]:

$$\mathbf{u} = \mathbf{M} \cdot \mathbf{F}_{resist} \quad (2.7)$$

Using this calculated velocity, the new position of the mobile sphere can be obtained. The calculation procedure continues until the final position is reached. This final position corresponds to a distance of six times the radius of the droplets after collision ($h = + 6a$). This separation distance was chosen because both experimental observations and theoretical calculations prove that beyond that point, the trajectory is a straight line, with constant x_f and z_f .

As it was mentioned earlier, it is necessary to know the exact initial positions of the droplets in order to solve the trajectory equation. The x and y positions are directly determined since the direction of observation is perpendicular to the x-y plane. Their exact position is determined by an image analysis software. Finding the z-coordinate requires more calculations. First, the velocity of the mobile droplet has to be found by determining the y-position as a function of time from a series of consecutive images. From the mobile droplet velocity and the known constant shear rate, it is possible to calculate the initial and final z-coordinates for a single particle moving in a wall shear flow based on the work by Goren and O'Neill [61] using the following equation:

$$V_p = f(H)Gz \quad (2.8)$$

where V_p is the velocity of the mobile sphere close to the wall, $f(H)$ is a correction factor that accounts for the effect of the wall on the movement of the mobile sphere (note that $H = (z - a)/a$) and G is the shear rate.

The experimental data are submitted to two screening procedures. The first screening consists of plotting the approaching and receding trajectories of the mobile droplet and removing the experimental points for which the trajectories show abnormal behaviour. This screening allows the removal of collisions that may have been disturbed by the other droplets of the emulsion within $20a$. The influence of other droplets is observed by fluctuation or oscillation in the trajectory followed by the mobile droplet. The second screening uses a deviation factor defined by Wu and van de Ven [62] as:

$$f_{\perp} = \frac{r_{th} \Delta\theta}{\Delta r} \quad (2.9)$$

where f_{\perp} is the deviation factor, r_{th} is the distance between the centre of the stationary droplet and a theoretical final position, $\Delta\theta$ is the difference in scattering angle between the experimental and theoretical final positions and Δr is the distance between the initial position of the mobile droplet and the theoretical final position. Note that a graphical representation of the deviation factor is shown in reference [62].

The deviation factor is an indication of the magnitude of the tangential displacement (with respect to the surface of the stationary droplet) compared to the radial displacement. Applying the deviation factor criteria to the experimental results removes the collisions for which tangential displacements due to surface roughness or to large Brownian motion were too significant. The computer algorithms used in

the hydrodynamic and in the screening calculations were provided courtesy of Dr. P. Warzyski and Dr. T.G.M van de Ven (McGill University, Canada) and of Dr. Alex Wu (Syncrude Canada Ltd.).

Finally, it should be mentioned that the χ^2 -minimisation procedure described in [54] was not used in this study due to the different colloidal forces experienced in each collision caused by surface heterogeneity. Therefore, the parameters used in the colloidal force model were not fitted but rather provided by the author and their adequacy was judged simply by observation from the scattering diagrams.

2.4.2. Hydrodynamic Force Balance Technique

The hydrodynamic force balance (HFB) technique is a recently developed technique that complements the colloidal particle scattering method. Wu *et al.* [9] developed the technique at Syncrude Research Centre (Edmonton, Canada) in 1999. In HFB, the microcollider apparatus described in section 2.2.1 is operated in a different mode to directly determine the maximum attractive force (near the secondary minimum – cf. Figure 1.4 for definition of secondary minimum) between two equal-sized colloidal particles. As with colloidal particle scattering, the HFB technique can be applied to emulsions, as long as the liquid droplets do not deform and the no slip velocity boundary conditions on their surfaces still hold.

The HFB technique can generally only be used to measure the maximum attractive force near the secondary energy minimum. Figure 2.6 indicates the location of the maximum attractive force (also referred to as the secondary force minimum) on a typical force-distance curve. Note that for bitumen droplets in water, as in most colloidal systems, the force near the energy barrier (cf. Figure 1.4) exceeds by far the range of applicability (in terms of force) of the microcollider apparatus. In addition, the energy barrier is quite high for bitumen droplets in water under the conditions

used in the present study (10). Thus, all doublets of bitumen droplets created in this study were secondary doublets.

Since HFB requires microscopic observation, the droplets or particles under investigation must have diameters of about 4 to 8 μm . Using larger droplets is possible but the sensitivity of detection of colloidal forces becomes lower for large droplets. This lower sensitivity can be explained by the fact that the hydrodynamic forces increase more rapidly with particle size than colloidal forces. When the size of the droplets is in the 4-8 μm range, forces as low as 10^{-13} N can be accurately measured. In fact, the range of measurable forces is from approximately 0.2 pN to 10 pN. The lower limit corresponds to an energy minimum of about 0.5 kT.

Figure 2.7 presents the basic principles of the HFB technique. The hydrodynamic force balance method consists of creating and breaking a doublet made of a “free⁵” droplet and of a stationary one fixed to the bottom surface of the glass plate of the steel cylindrical tube. This doublet is created by using the joystick of the microcollider to produce a weak shear flow of approximately 2 s^{-1} . Once the doublet is created, it is submitted to an increasing wall shear rate until the doublet separates or until the physical limits of the apparatus are reached. At the onset of break-up, i.e. at the time the break-up occurred (cf. t_b in Figure 2.7), the colloidal force, $F_{\text{colloidal}}$, is approximately equal to the hydrodynamic drag force, F_{hydr} .

$$\mathbf{F}_{\text{colloidal}} = \mathbf{F}_{\text{hydr}} \quad (2.10)$$

The hydrodynamic force balance technique requires that droplets coagulate at a small separation distance. In order to do so, a higher electrolyte concentration may have to be used. In addition, due to calculation issues, the droplets must be spherical and of equal size. In practice, a tolerance of 5-10% difference in droplet diameter is allowed.

⁵ The term “free droplet” refers to a droplet that was mobile before the doublet was created and that will become mobile again once the doublet is separated.

To simplify the force calculations, the mobile droplet is placed directly behind the stationary one. Thus, any lateral force can be neglected in the calculations. The lack of importance of lateral forces was shown by Wu *et al.* [9] who estimated the resulting error to be less than one percent. Regardless, a slightly off-centre “free” droplet will usually realign itself with the flow prior to separating from the stationary droplet, unless there are tangential forces caused by surface roughness.

A doublet is created immediately before application of shear to neglect any kinetic effect on possible adhesion. Before an experiment is started, a shear flow of about 0.5 s^{-1} is used to test the mobility of the newly formed doublet in both x and y directions (cf. Figure 2.2 for the coordinate system). The amplitude of the movement is very small, normally less than $0.5 \mu\text{m}$. Since the doublets created are secondary doublets (i.e. doublets having an energy of approximately the secondary energy minimum), the mobility of the “free” droplet should be in the x -direction only. When there is mobility in both directions, it means that either no doublet was created or that the energy well is lower than 1 kT . When this is the case, another collision is generated and the mobility is re-tested. No mobility would mean that both droplets are attached to the top wall.

Once the mobility is tested, a relatively high shear is generated. To prevent flow oscillations, the shear rate is increased by small steps. The shear is stopped after the doublet has separated and the mobile droplet has moved far away from the stationary droplet. The process is represented in Figure 2.7. If the “free” droplet has not stuck to the glass surface after break-up, the same pair may be reused for another attempt. In most cases, however, a new pair has to be found.

The break-up experiments are recorded on videocassette and subsequently analysed. Image analysis software is used to determine the frame at which the break-up occurs. From that data and the information stored in a computer file, it is possible to

determine the time elapsed since the beginning of the experiment as well as the shear rate at which the doublet separated.

The hydrodynamic drag force can be calculated using the hydrodynamic theory. The first step consists of calculating the fluid velocity vector, $v(x)$, by solving the Stokes and the continuity equations (cf. Equation 2.2 [54]) for a system composed of a solid wall and two rigid spheres attached together. In the system, one of the spheres, referred to as the stationary droplet, is attached to the wall (cf. Figure 2.7). As with colloidal particle scattering, the solution to the Stokes and the continuity equations is given by Equation 2.3 [54]. The final step consists of calculating the total force and torque acting on the fluid by particle j using Equation 2.4 [54]. More details on the solution of the hydrodynamic equations are provided in reference [60].

In order to calculate the hydrodynamic drag force, it is necessary to determine the initial coordinates of the droplets. As it was the case for CPS, the dimensionless coordinates for the stationary droplet are given by $(0, 0, 1)$. The x -coordinate of the free droplet has to be zero otherwise the doublet aligns with the flow before breaking-up. Therefore, the effect of a slight deviation in the x -direction is negligible and the hydrodynamic drag force in that direction is taken as zero. The y -coordinate could be obtained directly from image analysis. However, it is technically difficult to do so due to the proximity of the two droplets. A study of the variables showed that the force in the y -direction was almost independent of the y -coordinate as long as $y < 2.04$, which corresponds to $h < 120$ nm or more depending on z [9]. The range of $y < 2.04$ is almost always satisfied in the experiment. Therefore, an arbitrary y value was used, namely 2.005. Finally, the z -coordinate is calculated from Equation 2.8 at a point far away from the stationary droplet, using the shear rate and velocity stored in the computer file for this particular point. Only z values lower than 2 are kept since it is difficult to accurately determine the break-up frame when the free droplet is deeper. Reference [9] discusses the validity of those assumptions in more details.

Based on the above, z is the only variable coordinate and F_y and F_z are the only non-zero force components. Note that F_y and F_z are the dimensionless components of the hydrodynamic drag force. Figure 2.8 provides a graphical representation of the forces involved. Assuming the forces are balanced in the normal direction, i.e. through the droplet centres, the dimensionless maximum attractive colloidal force is given by [9]:

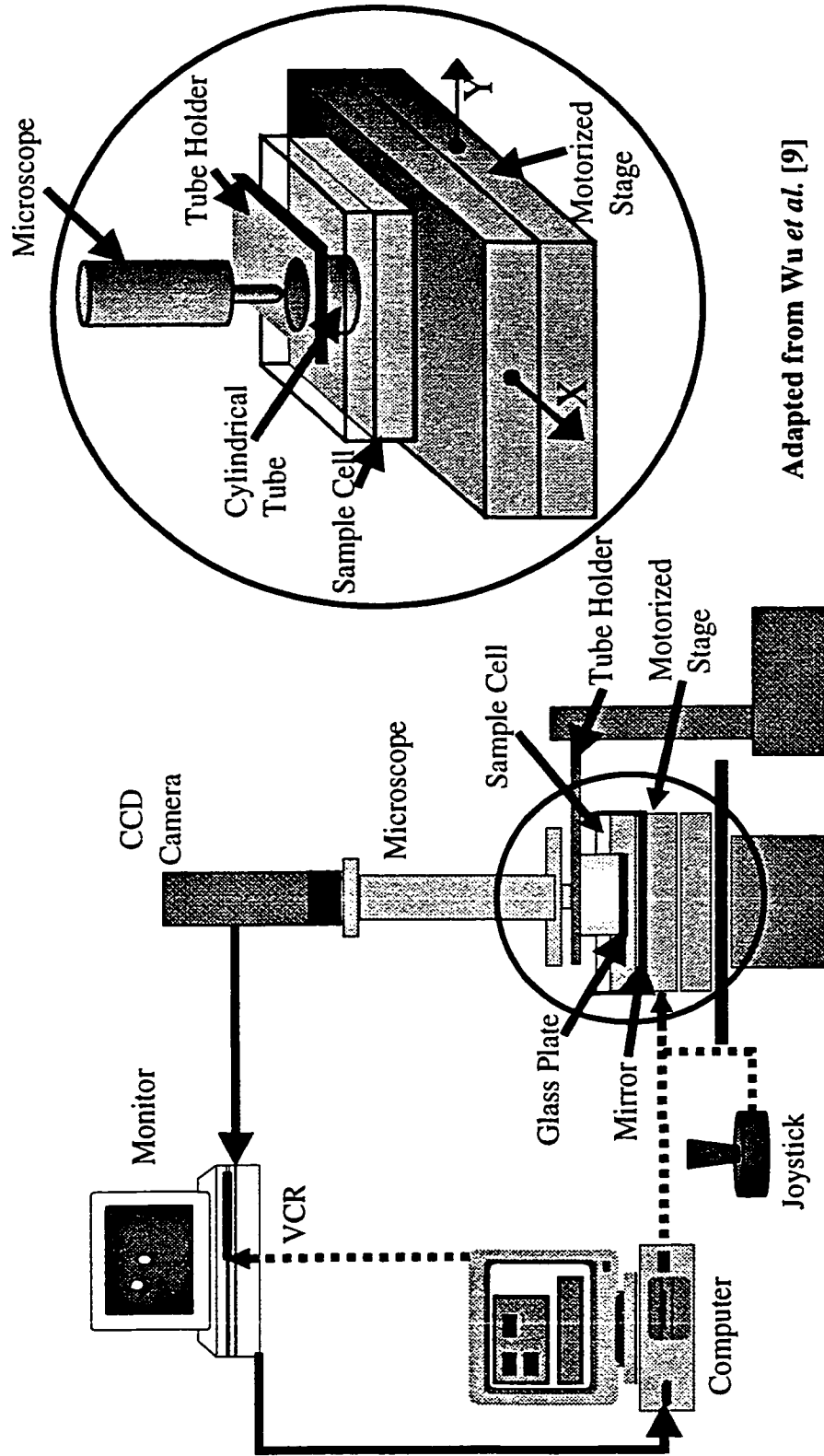
$$F_{\text{coll}} = F_y(z_b) \frac{y_b}{\sqrt{y_b^2 + (z_b - 1)^2}} + F_z(z_b) \frac{z_b - 1}{\sqrt{y_b^2 + (z_b - 1)^2}} \quad (2.11)$$

Equation 2.11 was derived directly from geometric considerations (cf. Figure 2.8). The subscript b refers to the position of the mobile droplet at break-up.

The colloidal force is finally obtained by multiplying the dimensionless colloidal force calculated by Equation 2.11 by the scaling factor, namely $6\pi\mu G_b a^2$, where μ is the solution viscosity and G_b is the shear rate at break.

The colloidal force calculated can be related to a colloidal force model, such as the DLVO theory, to determine the adjustable parameters (e.g. Hamaker constant, retardation wavelength, etc.) of the colloidal force model. In particular, surface roughness can be estimated in such a way. More information on surface roughness characterisation using the HFB technique will be provided in Chapter 4. In summary, both techniques described above are well covered by Wu *et al.* [6, 9, 10].

Figure 2.1: Microcollider Apparatus



Adapted from Wu *et al.* [9]

Figure 2.2: Basic Principles of Colloidal Particle Scattering

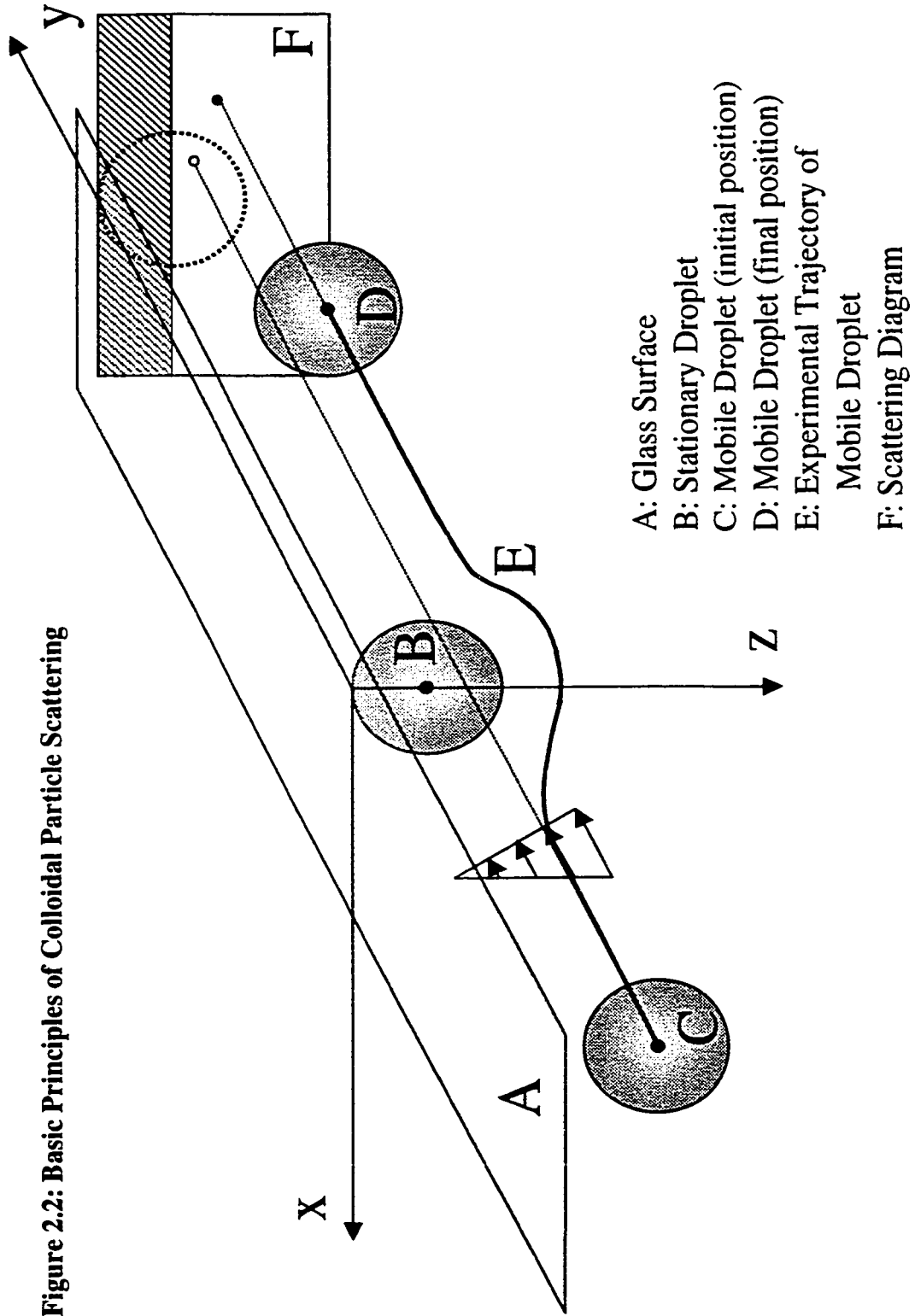
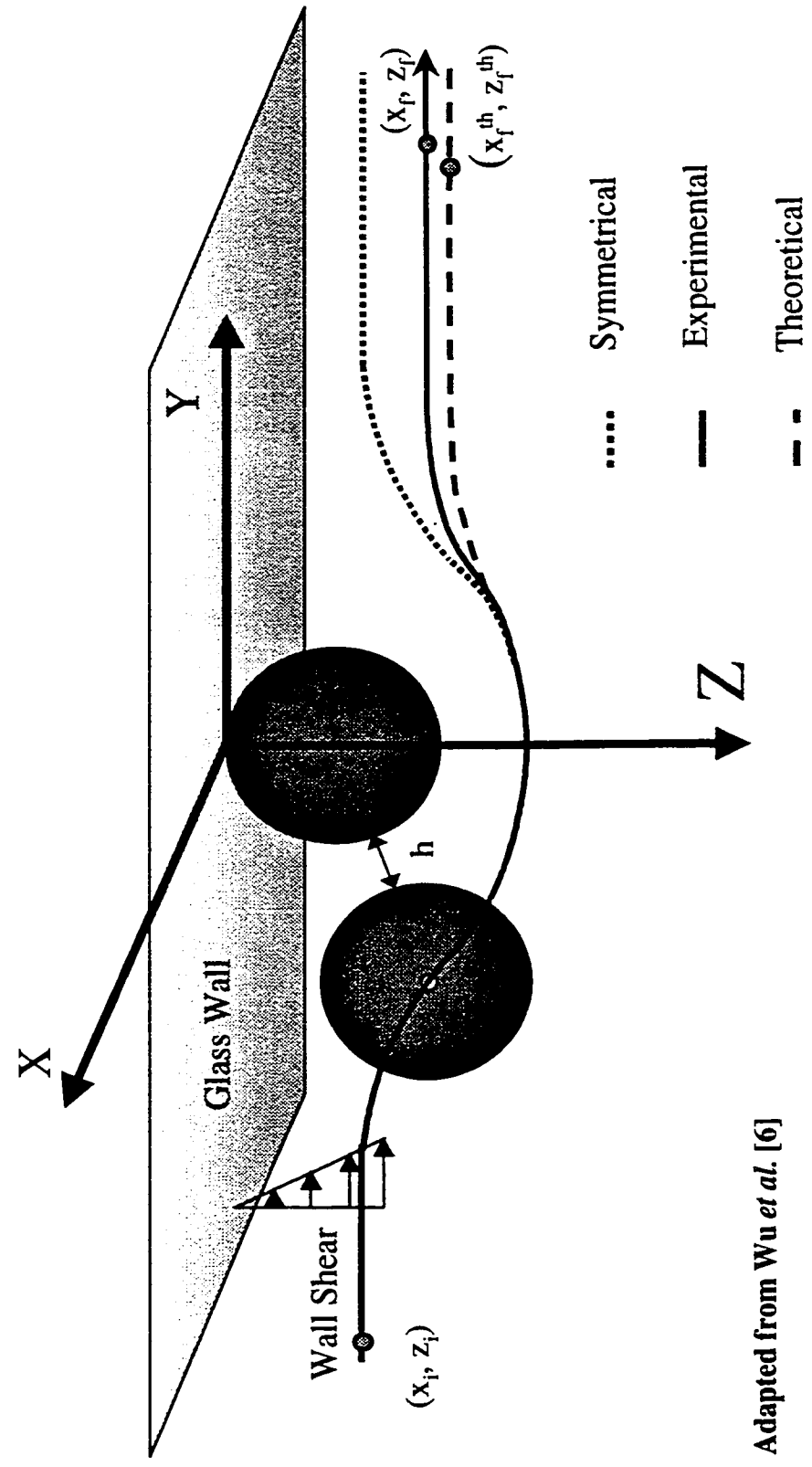


Figure 2.3: Particle Trajectories in Colloidal Particle Scattering



Adapted from Wu *et al.* [6]

Figure 2.4: Typical Scattering Diagram

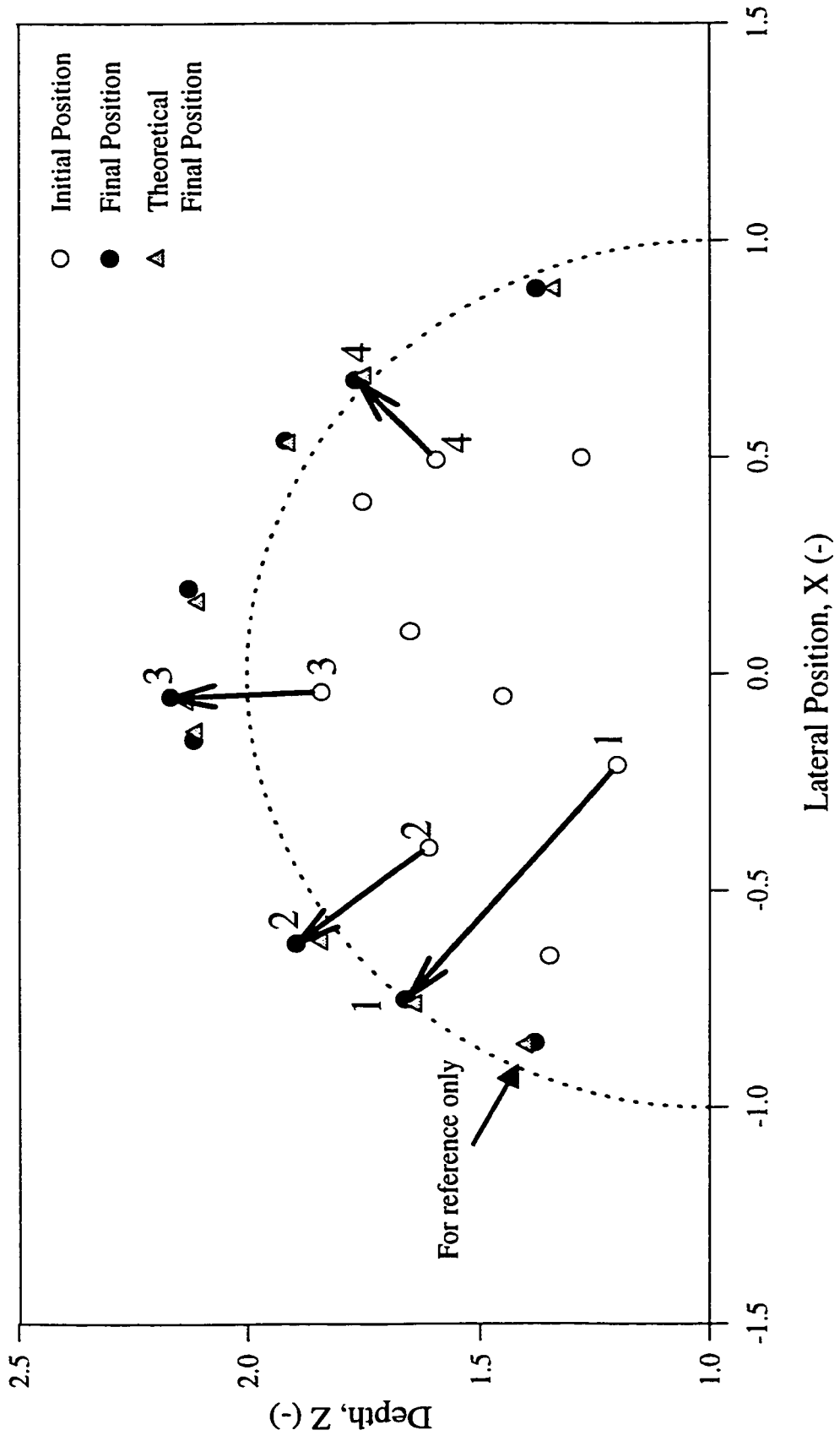


Figure 2.5: Calculation Scheme for Colloidal Particle Scattering

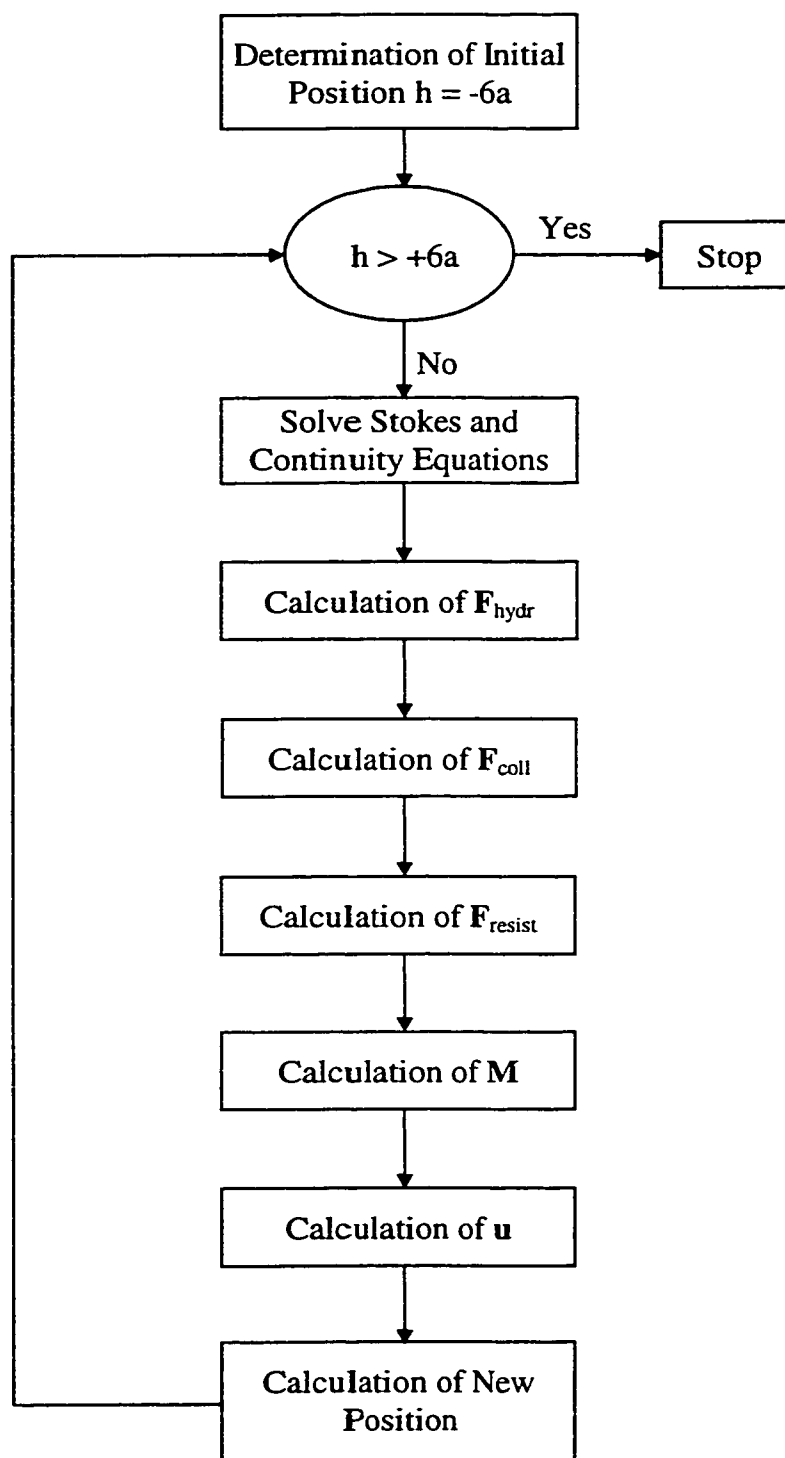


Figure 2.6: Location of the Maximum Colloidal Attractive Force on a Typical Force-Distance Curve

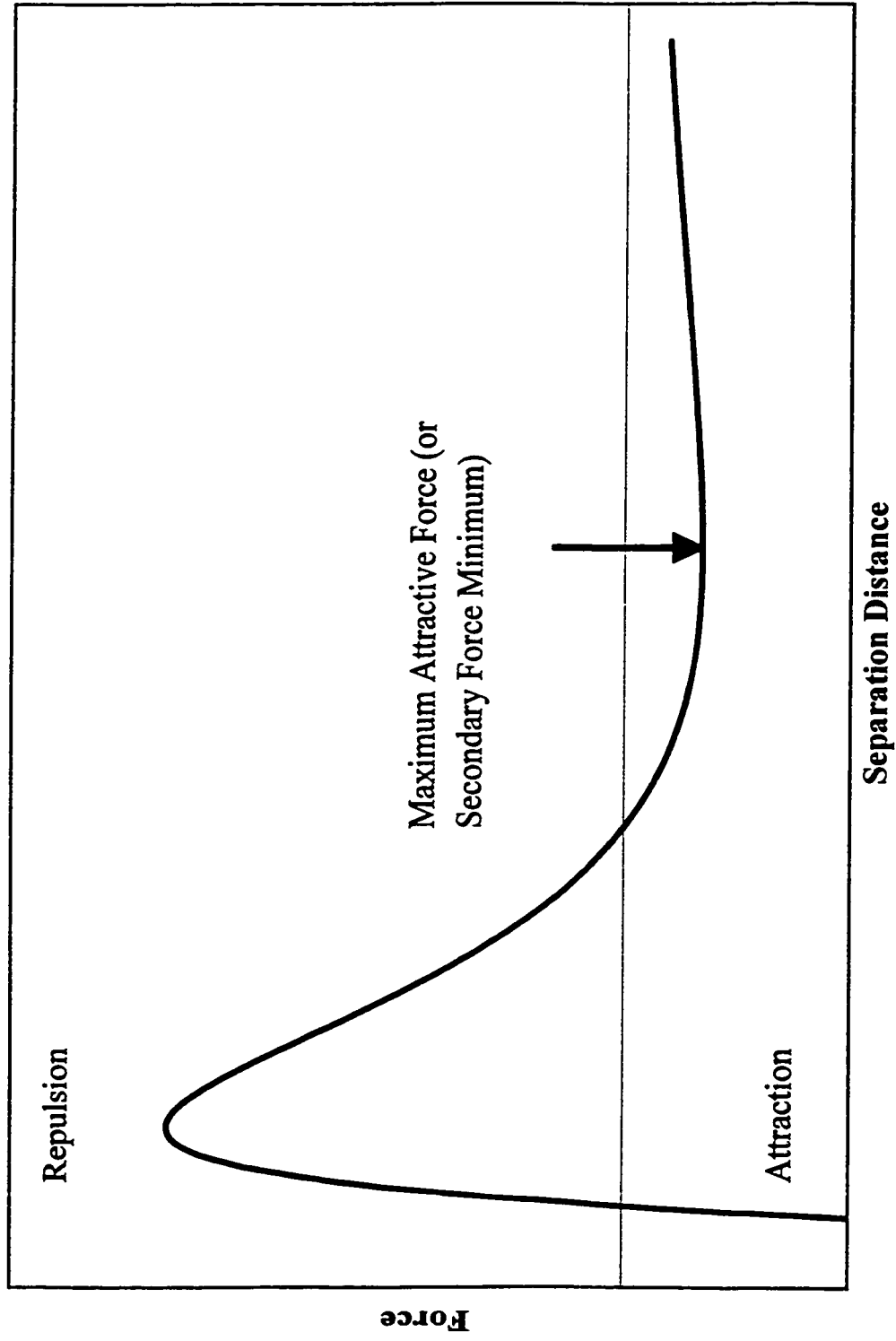


Figure 2.7: Principles of Hydrodynamic Force Balance Technique

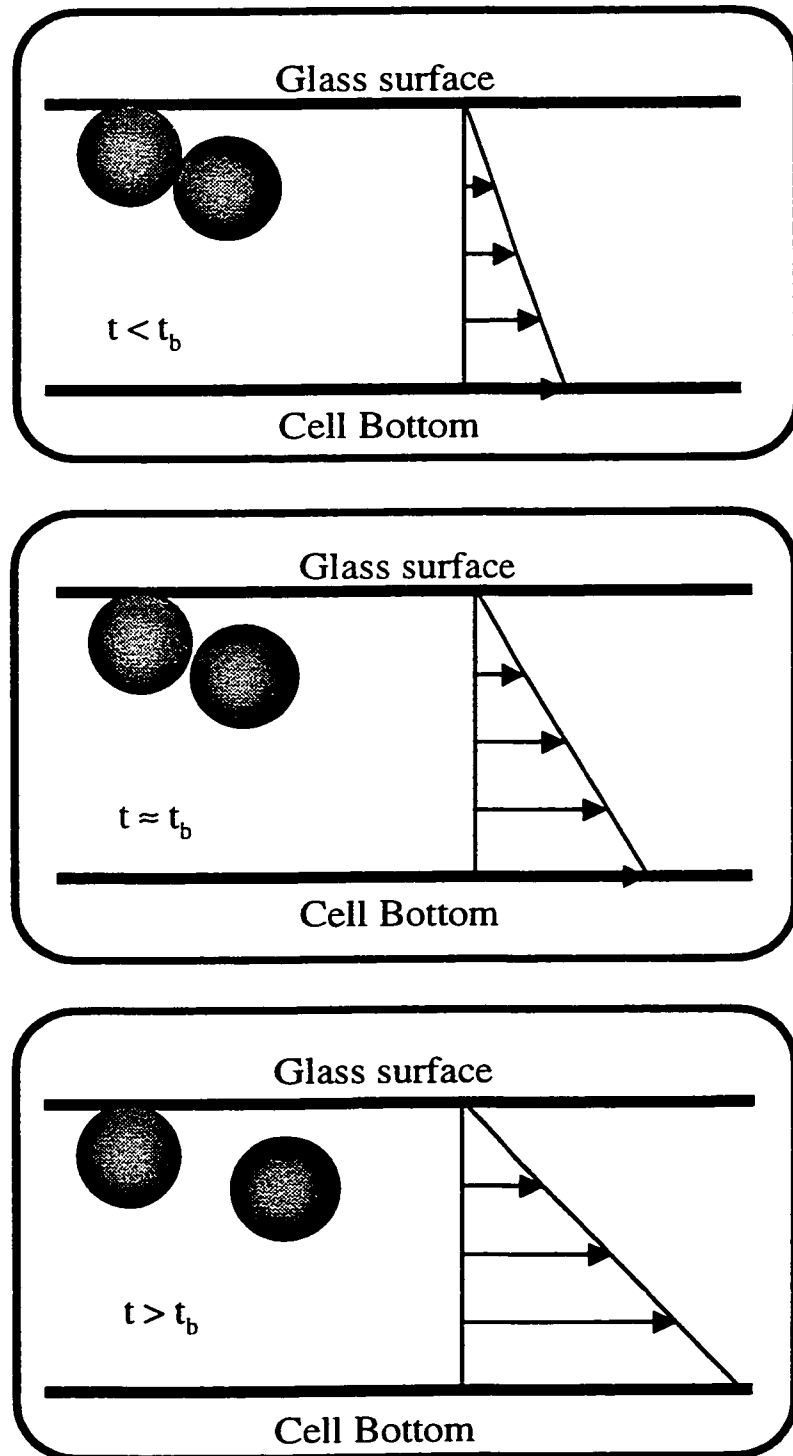
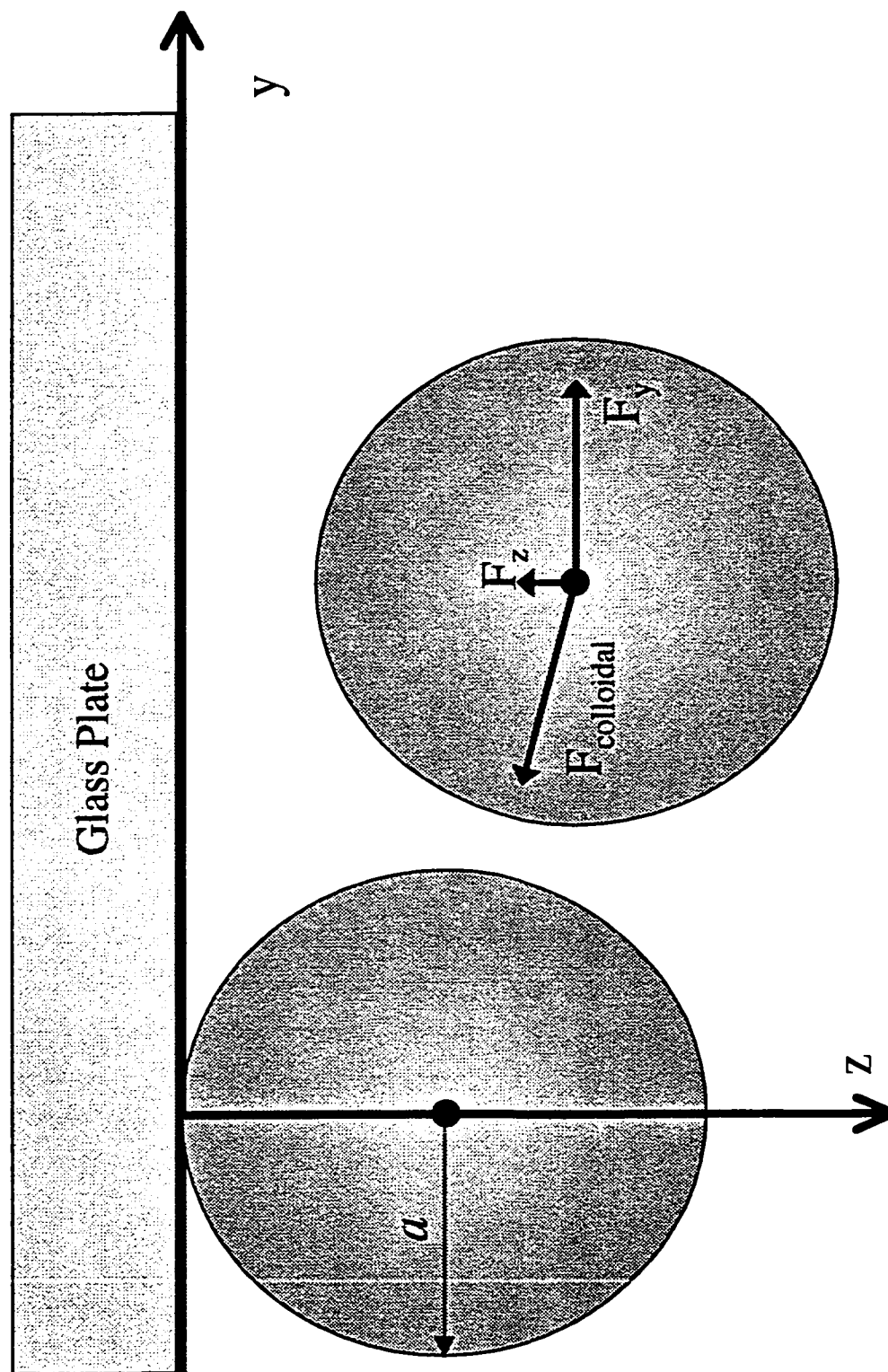


Figure 2.8: Representation of the Forces Involved in the Hydrodynamic Force Balance Technique



CHAPTER 3

INTERACTION OF BITUMEN DROPLETS USING COLLOIDAL PARTICLE SCATTERING

3.1. Effect of Asphaltenes

Bitumen has many components, one of them being asphaltenes. As mentioned in Chapter 1, asphaltenes are the insoluble part of bitumen in low molecular weight alkanes, usually *n*-heptane. Asphaltenes are known to form aggregates at the water-crude oil interface [7]. It is quite probable that asphaltenes also form aggregates on the surface of bitumen droplets in an aqueous solution. Since the behaviour of colloidal systems depends, to a great extent, on the surface chemistry of the colloidal particles or droplets, asphaltenes may play a role in the stability of bitumen emulsions. Indeed, some studies [7, 55, 57] indicate that asphaltenes have a great effect on the stability of bitumen and petroleum emulsions. In addition, bitumen from oil sands contains a small amount of residual solids that can also affect the behaviour of the emulsion. The effect of the residual solids was studied by Wu *et al.* [10]. They found that the removal of these solids with a 25-nm filter resulted in a more attractive force near the secondary minimum and made the bitumen droplets smoother. It is believed that some of the asphaltenes were also removed in the process. The present study focuses on the effect of asphaltenes. First, asphaltenes were removed from bitumen, following a procedure described in Chapter 2, to produce an asphaltene-free bitumen sample referred to as « deasphalted bitumen ». Note that the deasphalting process also removes the fine solids and that the word “asphaltenes” used in this study includes these fine solids. The effect of asphaltenes was studied by comparing the interaction between droplets of deasphalted bitumen with the interaction between bitumen droplets. Results obtained using the colloidal particle

scattering technique are presented in this chapter whereas those obtained with the hydrodynamic force balance method will be presented in Chapter 4.

3.1.1. Interaction between Deasphalted Bitumen Droplets in 0.04M KCl

The results obtained for two droplets of deasphalted bitumen in an aqueous solution containing 0.04 M of KCl are given in Figure 3.1. The droplets used had an average radius of 4.5 μm . Since the final positions of the mobile droplet are located farther from the centre than the initial positions, it is clear that the effective force is repulsive. The theoretical final positions calculated by the DLVO colloidal force model are also represented on this graph by gray triangles. The parameters used in the calculations are given in the Figure Caption. As a reminder, the DLVO theory combines only two contributions, the van der Waals and the electrostatic interaction, which for two equal-size spheres are given respectively by:

$$F_{\text{vdw}} = -\frac{Aa}{12h^2} f(h) \quad (3.1)$$

$$F_{\text{el}} = 32\pi a \epsilon \epsilon_0 \kappa \left(\frac{kT}{ze} \right)^2 \tanh^2 \left(\frac{ze\psi_0}{4kT} \right) \exp(-\kappa h) \quad (1.7)$$

where $f(h)$ is the retardation function given by Equation 1.13.

The DLVO force model has many parameters that need to be specified. Among these, the radius of the spheres was determined by image analysis, the Debye length was calculated from the known electrolyte concentration (Equation 1.1) and the zeta potential was measured by electrophoresis. The retardation wavelength was fixed at 100 nm according to the literature [24]. The Hamaker constants of common materials can be found in the literature as well. However, in the case of deasphalted bitumen, the Hamaker constant has to be assumed, as reliable literature data are not available.

It will be shown later that results obtained from CPS and HFB experiments can occasionally be used to determine the Hamaker constant value.

As it can be observed from the scattering diagram presented in Figure 3.1, the DLVO model predicts much lower repulsion forces than those indicated by the experimental final positions (black circles).

One of the possible explanations for the high repulsion observed in Figure 3.1 is the presence of surface roughness on the droplets. However, since deasphalted bitumen is expected to be quite smooth, this would be a surprising result. To ensure that surface roughness is not a factor causing the increased repulsion, images of deasphalted bitumen droplets were taken by a scanning electron microscope (SEM) equipped with a cryo-stage. Images of two different droplets were taken both of them show the same surface structure. One of the SEM images is shown in Figure 3.2. It is clear from the image that the droplet is indeed relatively smooth and that the proportion of surface covered by the small protrusions observed is low. This low surface coverage by the protrusions makes collisions between two smooth parts of the droplets likely. It is thus assumed that a collision showing the highest attraction corresponds to a smooth-sphere collision since surface roughness reduces the attractive force around the secondary minimum. For deasphalted bitumen, the arrow on Figure 3.1 indicates the most attractive collision.

For this data point, the smooth sphere-sphere interaction follows the DLVO force model. Therefore, the Hamaker constant can be determined from the observed trajectory. To do so, the theoretical final position corresponding to the data point indicated by the arrow on Figure 3.1 was calculated for different Hamaker constant values, keeping all other parameters constant. Note that the data point located at the right of the one pointed by the arrow could not be used for this calculation since its deviation factor was too high (cf. section 2.4.1). The best fit yielded a Hamaker constant of 2.7×10^{-21} J. This Hamaker constant was used to calculate the rest of the

theoretical final positions shown on Figure 3.1. The Hamaker constant of bitumen-water-bitumen calculated from literature values is roughly 2.8×10^{-21} J. [6] Previous experiments using the colloidal particle scattering [6] and the hydrodynamic force balance [9] techniques reported Hamaker constant values of 3.0×10^{-21} J and 3.2×10^{-21} J, respectively. Therefore, the Hamaker constant value for deasphalted bitumen-water-deasphalted bitumen is quite close to that of untreated bitumen.

Although smooth-spheres interactions are likely to occur, some small protrusions are nevertheless visible on Figure 3.2. The radius of these protrusions is estimated as 25 nm on average. In Chapter 1 the importance of surface roughness was discussed. Thus, the presence of these protrusions may be sufficient to explain the results. A force model accounting for roughness was attempted. This model was developed by Wu *et al.* [6] and is represented in Figure 3.3. It assumes that roughness can be represented by two disks, one on each of the droplets surface. Since the force model considers only one disk per droplet, the model is referred to as the “single disk model”. The model is adequate for surfaces with a small number of protrusions. The two disks are assumed to be in the centre of the gap width between the two droplets and to directly face each other. Offset configurations (i.e. when one disk is moved off the centre of the sphere surface within the gap width) are believed to exist. Wu *et al.* [9] estimated that up to 1.5 times the radius of the disk, the offset configuration has a relatively low influence on the interaction force. The force difference due to off-centred disks increase up to 40% beyond the 1.5 times the radius limit.

As it can be noted from Figure 3.3 the separation distance, h , is defined in the disk model as the distance between the surfaces of the two disks and not between the surfaces of the two droplets. Hence, the two droplets are separated by a distance of $h + L_T$ where L_T is the total thickness of the two disks. It should be noted that the disk model is incapable of determining the thickness of the individual protrusions. Therefore, the total thickness may indicate two disks of equal thickness $\frac{1}{2}L_T$ or a single disk of thickness L_T . For calculation purposes, it is assumed that both disks

have the same thickness, $L = \frac{1}{2} L_T$. In the single disk model for colloidal forces, the shear plane used in the hydrodynamic calculations is assumed to be spherical and located on the outer surface of the disk protrusion.

The interaction force for the disk model is calculated by assuming that the interaction coming from the disks can be modelled as an interaction between two flat plates. The electrostatic force or double-layer force is calculated using a combination of sphere-sphere interactions and plate-plate interactions, as indicated by the following expression [6]:

$$F_{cl} = B\pi a\kappa^{-1}e^{-\kappa(h+2L)} + B\pi r^2 \left[e^{-\kappa h} - e^{-\kappa(h+2L)} \right]$$

$$\text{where } B = 32 \tanh^2 \left(\frac{e\psi_0}{4kT} \right) \epsilon_0 \epsilon \kappa^2 \left(\frac{kT}{ze} \right)^2 \quad (3.2)$$

In Equation 3.2, the first term corresponds to the electrostatic contribution arising from the two spheres. The second term is the interaction between the two disk protrusions whereas the third term is subtracted to prevent overestimating the electrostatic force. This third term corresponds to the part of the spherical surfaces covered by the disk. Due to the fast decay of the double layer force, the disks to spheres interactions are neglected. Note that when the thickness L is equal to zero, Equation 3.2 reduces to the DLVO expression for smooth spheres interaction.

The van der Waals retarded forces are calculated by Hamaker's pairwise addition method [22], assuming that the contributions from the two spheres, the two disks and the disks to spheres are additive. This yields the following expression [9]:

$$F_{vdw} = -\frac{A_{s-s}a}{12(h+2L)^2} f_1(p) - 2A_{d-s}r^2 \left[\frac{f_2(h+L)}{(h+L)^3} - \frac{f_2(h+2L)}{(h+2L)^3} \right] - A_{d-d}r^2 \left[\frac{f_2(h)}{h^3} - 2\frac{f_2(h+L)}{(h+L)^3} + \frac{f_2(h+2L)}{(h+2L)^3} \right] \quad (3.3)$$

In Equation 3.3, $p=2\pi(h+2L)/\lambda$, r is the radius of the disk protrusion, f_1 is the retardation function for two spheres given by Equation 1.13 whereas f_2 is the one for two plates, given by Equation 1.14. A_{d-s} is the Hamaker constant corresponding to the disk to sphere interaction and A_{d-d} refers to the Hamaker constant for the two protrusions. Both Hamaker constants are for bodies in aqueous media. It should be mentioned that the disk to sphere interaction is modelled as a flat plate-half space interaction. This simplification is acceptable since the condition $r \ll a$ is always satisfied. The expression for the interaction between the two disks was derived by Wu *et al.* [9] and provides results within 10% of the actual van der Waals force values obtained from numerical integration over the volume of the disk protrusions.

The Hamaker constant values A_{d-d} and A_{d-s} depend on the composition of the protrusions. Wu *et al.* [6] discussed two different cases for the van der Waals interaction calculations. The first case assumes that the disks are made of 100% bitumen in which case Equation 3.3 reduces to:

$$F_{vdw} = -\frac{A_{s-s}a}{12(h+2L)^2} f_1(p) - A_{s-s}r^2 \left[\frac{f_2(h)}{h^3} - \frac{f_2(h+2L)}{(h+2L)^3} \right] \quad (3.4)$$

The second case Wu *et al.* [6] mentioned assumes that the disks are made of 100% water. One must not assume that this latter case is equivalent to no disk at all. The situation rather refers to water trapped by long chains with charge groups at the tips. The van der Waals forces between these chains are negligible due to the low mass of the chains (<10%). The repulsion calculated from this model is even higher than that in the case of 100% bitumen protrusions. Note that for disks made of 100% water, A_{d-d} and A_{d-s} are equal to zero. Thus, the van der Waals force is calculated using the

first term only in Equation 3.3. The actual material composition of the protrusions is not known, but most certainly lies between those two extremes and will depend on the degree of hydration of the protrusions. In fact, if the surface asperities were made of pure bitumen, they would most likely not protrude. On the other hand, if they were made of pure water they would not be seen on the SEM images.

The results obtained with the disk model assuming 100% water in protrusions are plotted in Figure 3.4. As it can be observed from the figure, the single disk model provides a much better fit than the DLVO model. However, it is not sufficiently repulsive to fit all the experimental points obtained. In the case of 100% bitumen in protrusions, the theoretical predictions are less repulsive than those for 100% water in protrusions and are thus farther away from the experimental results. They are not shown in Figure 3.4.

Note that on Figure 3.4, only results for a 20-nm thickness are reported. Calculations were also performed for some larger protrusion thickness but they all yielded theoretical final positions very close to those obtained using a 20-nm disk thickness. Therefore, the thickness of the disk cannot completely explain the experimental results.

A larger disk radius could enhance the repulsion force. Calculations were thus made for radius values of 25 nm and 40 nm, but no significant effect on the repulsion was observed. Larger radius values are unlikely (cf. Figure 3.2).

In Chapter 1, it was mentioned that the geometry of the protrusions (flat plates, spherical caps, etc.) affects the interaction forces. However, it is impossible to determine the exact geometry of the protrusions from the SEM image. Since the disk geometry has more surface area at close separation distance than any other possible geometric shapes, it is likely to give the most repulsive case.

There are several other hypotheses that might explain why the experimental results are more repulsive than what is predicted by the classical DLVO and the single disk theories. One may be tempted to explain the difference by charge heterogeneities. However, as discussed in Chapter 1, charge heterogeneities, when considering all possible orientations, reduce the electrostatic force. Since an increased repulsive force is observed here, charge heterogeneity cannot be a possible explanation. Other tentative explanations are related to the possible existence of long polymeric chains adsorbed on the surface of the deasphalted bitumen droplets. Two situations need to be considered and they are illustrated in Figure 3.5. The first situation suggests that several charged polymeric chains are adsorbed on the surface of the droplets. It is assumed here that all charges are on the chains and not on the surface of the droplets. For calculation purposes, water within the layer of chains is assumed to be “trapped” and the shear plane is taken at the outer limit of the layer. This situation will be referred to here as “enhanced electrostatic repulsion”. Note that the chains do not contact during a collision. In this enhanced electrostatic repulsion model, the colloidal force is simply calculated by the classical DLVO theory using Equations 3.1 and 1.7. However, the location of the charges and the shear plane have to be changed from the surface of the droplets to the outside limit (i.e. to $a + L$, where L is the thickness of the layer of chains) of the layer of adsorbed polymeric chains.

Another type of repulsion due to chains, called steric repulsion, occurs when some uncharged chains are adsorbed on the bitumen droplets. With a steric type of interaction, the chains come in contact during a collision and the repulsion is due to the interpenetrating and compression of the polymeric chains. Note that in this case the solvent is not “trapped” by the chains and the shear plane is somewhere in between the tip of the chains and the droplet surface. Calculations for the steric layer case are more difficult due to the difficulty of accurately determining the position of the shear plane. However, it is believed that this shear plane is very close to the surface of the droplet and for calculation purposes, it was simply assumed that the shear plane is located at the surface of the bitumen droplet. Calculations for a steric

type of interaction follow the scheme presented in Figure 2.5. In this case, however, the colloidal force is calculated by summing the electrostatic (Equation 1.7), the steric (Equation 1.8) and the van der Waals (Equation 3.1) forces and not only the electrostatic and van der Waals forces. Note that although the thickness of the layer of adsorbed chains is assumed to be uniform (to simplify the calculations), the actual length of the chains most likely varies from one chain to another.

Calculations were made for both the enhanced electrostatic repulsion and the steric repulsion force models and the final theoretical positions obtained with these models are plotted, respectively, on Figures 3.6 and 3.7. As it can be observed from these two scattering diagrams, both the steric layer and enhanced electrostatic repulsion models provide a much better fit of the experimental final positions. The calculations for the enhanced electrostatic repulsion model were made using two different layer thicknesses, namely 15 nm and 30 nm. Both thicknesses provided approximately the same theoretical ring of final positions, which fits more of the experimental data points than either the DLVO or the disk models. The enhanced electrostatic repulsion model is however incapable of fitting all the positions.

The theoretical final positions obtained from the steric force model seem to indicate an even better fit than the enhanced electrostatic repulsion model. The theoretical rings were calculated for a layer thickness of 7 nm and 20 nm. Most of the experimental data points are comprised between the DLVO ring and the 7 nm thickness ring, which seems to indicate that a thin steric layer is sufficient to explain the results. Finally, nearly all the experimental final positions are within or very close to the 20-nm thickness ring. Therefore, steric interaction is able to explain the repulsion observed experimentally.

Determining which of the enhanced electrostatic repulsion and the steric repulsion models is more likely is challenging since both models provide relatively good fits.

Looking at the tangential deviation⁶ seen in the collisions may help though. When the main repulsion mechanism is enhanced electrostatic repulsion, neither the droplets nor the layers touch each other during a collision. Therefore, the tangential deviation in the initial and final experimental positions should be very low. On the other hand, for a steric interaction to occur, the chain layers have to get in contact, which may be indicated on a scattering diagram by a greater number of odd points with large deviations or changes in the direction of displacement. For deasphalted bitumen, looking at the “unscreened” initial and final positions indicates that only a few collisions exhibited an unlikely behaviour. Most of the collisions were in fact very good collisions, as indicated by the great number of points that passed the two screening procedures. Thus, if chains are adsorbed on the bitumen droplets, they will most likely enhance the repulsion between the droplets by an enhanced electrostatic interaction mechanism.

3.1.2. Interaction between Bitumen Droplets in 0.04M KCl

To understand the effect of asphaltenes, it is necessary to compare the results presented in section 3.1.1 for the deasphalted bitumen droplets to those obtained for the untreated bitumen droplets. Therefore, experiments using the colloidal particle scattering technique were made for two different pairs of droplets having an average radius of 2.7 microns.

Scanning electron microscopy images were first recorded for two different bitumen droplets. One of them is shown in Figure 3.8. As it can be observed from this image, the bitumen surface is much rougher than the surface of deasphalted bitumen. In fact, the bitumen surface is entirely covered with protrusions having an estimated radius of 60 nm.

⁶ Tangential deviation refers to the distance between the experimental and the theoretical final positions in the direction tangent to the surface of the stationary droplet.

The scattering diagrams obtained for bitumen droplets are provided in Figure 3.9. The scattering diagram of Figure 3.9a provides the data points that passed the first screening procedure (to remove collisions disturbed by the presence of other droplets) whereas the one on Figure 3.9b gives the data points that passed both screening procedures. The second screening procedure discards collisions for which the deviation factor is too large. See section 2.4.1 for details about the screening procedures. Comparing the number of data points in Figures 3.9a and 3.9b show that many collisions exhibited a strong tangential deviation and were thus discarded by the second screening procedure. From the experimental final positions, it is clear that bitumen droplets repel each other much more than deasphalted bitumen droplets. Due to the large number of collisions observed for both deasphalted bitumen and bitumen, this effect is not caused by statistical errors. Hence, it can be concluded that the presence of asphaltenes in bitumen enhances the repulsion.

Additional information can be obtained by fitting the experimental results with a colloidal force model. For comparison purposes, the models used to analyse the results for deasphalted bitumen, i.e. the DLVO theory and the disk models, were applied to the bitumen results as well. Note that Figure 3.8 shows that smooth-spheres interaction are unlikely. Therefore, it is not possible to fit the Hamaker constant in a satisfactory manner using the experimental results. A value of 3.0×10^{-21} J was used in the calculations. This value is an average of the theoretical value calculated from literature data [6] (2.8×10^{-21} J) and of the value obtained from previous bitumen experiments [6, 9] (3.0×10^{-21} J and 3.2×10^{-21} J). Using a Hamaker constant value of 3.0×10^{-21} J along with the other measured parameters yields the theoretical final positions shown in Figures 3.9a and 3.9b. Calculations were first made using the classical DLVO theory, which predicts aggregation at the secondary minimum for all the collisions analysed. Thus, two disk thickness values (5 nm and 20 nm) were used to investigate the effect of roughness. Again, a disk thickness higher than 20 nm resulted in a ring at approximately the same position as

the 20-nm thickness ring. Note that calculations were made for the most repulsive case, i.e. for disks made of 100% water.

As it can be observed from Figure 3.9, very few experimental points can be explained by this disk model. The poor fit might be a result of the following errors. First, the assumed parameters of the Hamaker constant and the retardation wavelength may be incorrect. This possibility was tested by independently varying these two parameters. Lowering the Hamaker constant by an order of magnitude had a certain effect on the 5-nm thickness ring, but not on the 20-nm one. Therefore, even if a very low (and unlikely) Hamaker constant were used, the disk model would not be able to explain the results. The retardation wavelength was also changed. Usually, a value of 100 nm is used in the calculations. It was found that using values of 50 nm and 200 nm had a slight influence on the 5-nm ring but only a negligible effect on the 20-nm ring. Therefore, the previously used values, i.e. an Hamaker constant of 3×10^{-21} J and a retardation wavelength of 100 nm were kept for subsequent calculations.

A second possible explanation for the poor fit provided by the single disk model may be that this model is not representative of the surface roughness of bitumen droplets. From Figure 3.8, it is clear that the protrusions on the surface are densely populated, too numerous to be considered “single”. In addition, the protrusions look like truncated spheres instead of disks. Thus, a new spherical cap model was developed to better represent the surface structure observed in Figure 3.8. The model accounts for three different levels of asperities. The protrusions beyond the third level are neglected due to the fast decaying feature of the forces. The complete development is provided in Appendix A. To simplify the calculations, it is assumed that the spherical caps are directly facing each other. The electrostatic interaction was derived using Derjaguin approximation and a treatment similar to one described in reference [15]. The final expression obtained for a symmetric electrolyte is (cf. Figures A.1 and A.2 for a geometric representation):

$$F_{el} = F_{\text{sph.caps}}(h_0) + 6F_{\text{sph.caps}}(h_1) + 12F_{\text{sph.caps}}(h_2) \quad (3.5)$$

where:

$$F_{\text{sph.caps}}(h) = 2B \left(\frac{\pi}{\kappa} \right)^{1/2} \exp(-\kappa h) \int_0^r (a_c^2 - z^2)^{1/4} \exp\left(\frac{-\kappa z^2}{a_c} \right) dz \quad (3.6)$$

and $B = 32 \epsilon \epsilon_0 \kappa^2 \left(\frac{kT}{ve} \right)^2 \tanh^2 \left(\frac{e\psi_0}{4kT} \right)$

In expression 3.6, a_c is the radius of the sphere comprising the spherical caps (cf. Appendix A), r is the radius of the spherical caps, z is the radial distance from the centre of the spherical cap and v is the valence of the solution electrolyte. It should be noted that expression 3.6 is only valid for a certain range of spherical caps geometry and electrolyte concentrations, i.e. when $r (\kappa/a_c)^{1/2} \geq 2.75$. This condition is satisfied for the samples studied here. In fact, the error in the force calculated is less than 3% as long as $r (\kappa/a_c)^{1/2} \geq 1.6$.

The retarded van der Waals interaction was calculated by pairwise additivity and numerical integration using a program provided by Wu *et al.* [9] with modified lower and upper limits of the integrals. All possible contributions (sphere to sphere, spherical cap to spherical cap and spherical cap to sphere) were considered for all three levels of protrusions.

Applying this spherical cap model to the experimental results yields the force profiles plotted in Figure 3.10. Figure 3.10a focuses on the maximum repulsive force range (around the energy barrier) whereas the Figure 3.10b shows the results for the maximum attractive force area (around the secondary minimum). Also plotted are the force profiles for the DLVO theory and for the single disk model. In all these calculations, the disks and spherical caps were assumed to be made of 100% water since this case provides the highest repulsion (cf. 3.1.2). The two plots of Figure 3.10

clearly show that roughness has a large influence on the interaction. However, as it can be seen, the multiple spherical caps model gives a force profile that is a lot less repulsive than the single disk model for all the sets of parameters used.

Since the geometry of the spherical caps was estimated from the scanning electron microscope images, a study was made to study how strongly the results depend on the physical dimensions of the spherical caps. The “*Cap-Geometry*” curve plotted in Figure 3.10 was obtained by using physically plausible geometric parameters giving the most repulsive force profile. A radius of protrusion of 100 nm and a thickness of 5 nm were thus used. As it can be seen, the repulsion is enhanced when this geometry is assumed, but it is still definitely much lower than the repulsion given by the single disk model. Another sensitivity study was made for the zeta potential of the bitumen droplets. Although a value of -30 mV was actually measured, calculations were made using a value of -50 mV to study how an error in the zeta potential measurement would have affected the force profile. The force profile obtained using the -50 mV zeta potential value is referred to as “*Cap-Zeta Potential*” in Figure 3.10. As it can be observed from the figure, the resulting interaction is even lower than that shown by the Cap-Geometry curve. Hence, the spherical cap model, which is more likely to represent the surface roughness of the bitumen droplets, is incapable of explaining the highly repulsive interaction observed from the bitumen droplet collisions.

From Figures 3.9 and 3.10, it is clear that surface roughness alone is incapable of explaining the repulsion observed between the bitumen droplets. Therefore, the possibility of having an enhanced electrostatic repulsion or a steric repulsion was investigated. The results are plotted in Figures 3.11 and 3.12. It can be seen from Figure 3.11 that the enhanced electrostatic repulsion model (cf. Figure 3.5) provides a better fit than the single disk model but even a layer of chains 30 nm thick cannot fit all the points. The steric layer model (cf. Figure 3.5) provides an even better fit than the enhanced electrostatic repulsion model. Still, it is not possible to fit all the points with this model, even when a steric layer of 22 nm is used. In fact, a steric

layer of 30 nm was also assumed (results not shown) without being able to explain all the experimental final positions. The theoretical final positions obtained for a layer thickness of 30 nm were very close to the 22-nm ring and thus, no calculations using higher thicknesses were made. From the large deviation seen from the experimental positions and from the great number of points discarded by the tangential deviation screening (cf. Figure 3.9a and 3.9b), a steric interaction seems more likely.

In summary, from the scattering diagrams presented in this section and in section 3.1.1, the DLVO theory is clearly unable to correctly represent the interaction between bitumen droplets and between deasphalted bitumen droplets. Several colloidal force models were applied to the experimental results in an attempt to better understand the causes of the deviations from the DLVO theory. For deasphalted bitumen droplets, it is unclear whether roughness of enhanced electrostatic repulsion is the main contributor to the repulsion. However, steric interaction, which involves interpenetrating and compression of the adsorbed chains, is unlikely since the collisions showed very little tangential deviation. On the other hand, steric interaction seems to be the main mechanism for repulsion between untreated bitumen droplets.

Since colloidal particle scattering is an indirect method, a model is essential to determine the complete force profile. This force profile can be plotted using the parameters providing the best fit of the experimental results. With the exception of Figure 3.10, no force profiles are provided due to the difficulty of determining which model is most likely. However, all force profiles could easily be plotted using the appropriate equations for the different models and the sets of parameters provided underneath each graph.

The scattering diagrams contain valuable information. When comparing the scattering diagram obtained with deasphalted bitumen to that obtained from untreated bitumen, it is clear that untreated bitumen droplets repel each other more strongly than deasphalted bitumen droplets. Hence, it is possible to state that

asphaltenes contribute to the stability of a bitumen-in-water emulsion by enhancing the repulsion between the droplets of the emulsion. Examination of the experimental results would indicate whether a sample shows attraction or repulsion and gives a magnitude of the interaction under the hydrodynamic conditions applied during the experiments (a hydrodynamic force of roughly 1 pN is used). The analysis of the scattering diagrams with a force model provides additional information about attractive and repulsive forces.

Bitumen is known to be a highly heterogeneous material and scattering of the results is to be expected. Figures 3.4 and 3.9 indeed indicate that the experimental final positions are distributed over a considerable area on the scattering diagrams for both deasphalted bitumen and untreated bitumen. It is thus not surprising to observe that a single set of parameters is unable to fit most of the experimental data points for a given colloidal force model. Nevertheless, it is clear that the predictions from the DLVO theory are not representative of the experimental results. It is believed that surface roughness plays a role in the repulsion observed. From the scattering diagrams, it can be seen that deasphalted bitumen is smoother than bitumen. This is indicated by the fact that more data points are located within the 20-nm thickness ring calculated from the single disk model for deasphalted bitumen than for bitumen. The smoother surface of deasphalted bitumen was also observed from the SEM images.

3.2. Effect of Electrolyte on Bitumen Droplet Collision

Different electrolytes have different conductivities and can thus affect the diffuse electronic layers differently. In addition, since bitumen is a heterogeneous material composed of many ionisable compounds, the pH of the solution has an important effect on the surface charges of bitumen droplets. Therefore, the effect of a different electrolyte was investigated using a combination of 0.025M NaCl and 0.015M

NaHCO₃ yielding a pH of roughly 8.5, which is close to the process water chemistry used in bitumen extraction. Collisions for bitumen droplets in that solution were observed and compared with those of bitumen in a 0.04M KCl solution (unadjusted pH of 7) (cf. section 3.1.2).

Ideally, one set of collision experiments only includes collision data from one pair of droplets. However, the experimental conditions used for the bitumen in presence of NaCl and NaHCO₃ resulted in a strong bitumen-to-glass attraction. It became a challenging task to produce a sufficient number of collisions using a single pair of droplets since the mobile droplet easily attached to the glass surface. Here, three pairs of droplets were needed in order to get sufficient information. Their average radii were 2.5, 2.8 and 3.6 microns. Because their radii differ significantly, it is impossible to plot the experimental and theoretical positions obtained on a single scattering diagram. Therefore, three scattering diagrams will be presented for each colloidal force model. Calculations of the theoretical final positions were performed using models already discussed in section 3.1.2.

The three scattering diagrams plotted for the DLVO and the disk models are provided on Figures 3.13a, b and c. Again, the Hamaker constant had to be assumed rather than experimentally determined. A value of 3.0×10^{-21} J was chosen for the reasons already explained in section 3.1.2. As can be seen from the experimental data points shown on the three scattering diagrams of Figure 3.13, the bitumen droplets generally repelled each other when in a NaCl and NaHCO₃ aqueous solution. However, five collisions showed attraction between the droplets, a phenomenon that was not observed for the two other bitumen samples. The experimental results clearly indicate that a higher pH reduces the repulsion between the bitumen droplets. Since the same Hamaker constant was used for both samples and since the zeta potential of the bitumen sample in the presence of KCl is less negative than the bitumen sample in the presence of a combination of NaCl + NaHCO₃, the opposite should be observed. Note that the difference cannot be attributed to size effects since two pairs of bitumen

droplets in the NaCl and NaHCO₃ solution have a size similar to that of bitumen droplets in the KCl solution (cf. Figures 3.9 and 3.13).

The presence of adsorbed chains on the surface of the bitumen droplets cannot explain the different magnitude of repulsion, as their respective repulsion would follow the trend of the electrostatic force. In other words, the enhanced electrostatic repulsion would be higher for the bitumen droplets in a NaCl and NaHCO₃ solution since the chains for this bitumen sample are more negatively charged. Steric repulsion would also be higher for the bitumen in presence of NaCl and NaHCO₃ since uncharged chains should not be affected by the pH and thus, the steric contribution should be constant and independent of the pH. Thus, the presence of chains on the surface of bitumen droplets is likely but they cannot explain the weaker repulsion observed for bitumen droplets in the NaCl and NaHCO₃ solution.

Although the emulsions were prepared with the same bitumen, pH may affect the surface characteristics of the bitumen droplets. In fact, bitumen is a highly heterogeneous material that is made of many ionisable compounds and natural surfactants. Resins and asphaltenes, which are natural surfactants of bitumen, are especially important since they can form rigid films at the water-bitumen interface. Irrespective of the different electrolyte used, pH can affect the chemistry and the characteristics of the rigid film formed by these two components since both resins and asphaltenes contain basic and acidic functional groups. Thus, pH may affect the stability of bitumen-in-water emulsions. Studies made by McLean and Kilpatrick [7] and Strassner [63] indicated that pH had indeed a great effect on the stability of crude oil-water emulsions. Strassner [63] found that stability was related to the pH of the solution and that a minimum stability was usually seen at a pH of about 10 to 12. Strassner [63] also found that when a strong buffer such as sodium bicarbonate was added to the water phase, the pH at which the minimum stability occurred was lowered to about 6 or 7. McLean and Kilpatrick [7] mentioned that the state of dispersion of asphaltenes was very important and that these asphaltenes were only

able to stabilise the emulsion when they were above or very close to the point of incipient flocculation. In fact, McLean and Kilpatrick [7] pointed out that molecularly dispersed asphaltenes had very little effect on the stability compared to colloidal aggregates of asphaltenes. They also mentioned that resins enhance the solubility of asphaltenes by forming resin-solvated asphaltenes aggregates. McLean and Kilpatrick [7] also studied the effect of pH and found that a higher pH favoured the ionisation of the polar resins and asphaltenes, which produces an oil surface having a higher charge and a lower mechanical strength due to internal repulsion within the film. The effects of pH on the stability of crude oil-water emulsions are believed to apply to bitumen in water emulsions as well. Thus, a different electrolyte associated with a higher pH seems to facilitate the molecular dispersion of asphaltenes at the bitumen-water interface, which lowers the stability of the bitumen emulsion.

The results for the collision of bitumen droplets in the presence of NaCl and NaHCO₃ indicate that the disk model fits the results much better than for bitumen droplets in KCl alone. However, as discussed in section 3.1.2, the single disk model does not provide the best possible representation of the surface structure of bitumen droplets. The more “realistic” spherical caps model yields even poorer theoretical results than the single disk model.

As it was the case for bitumen and deasphalted bitumen in a KCl solution, calculations of the final positions predicted by the enhanced electrostatic repulsion and the steric repulsion models were also performed. The results obtained for all three pairs of droplets are plotted, respectively, in Figures 3.14 and 3.15. In all cases, the enhanced electrostatic repulsion model gives a higher repulsion than the single disk model. The theoretical final positions rings, although providing a better fit than the disk model are not able to represent all the experimental final positions. In opposition to the enhanced electrostatic repulsion model, the steric model is capable of fitting all

the experimental final positions, except for four data points. In addition, the steric layer needed is thinner than the one needed for bitumen in the presence of KCl alone.

Thus, using a solution of NaCl and NaHCO₃ at an unadjusted pH of 8.5 instead of a solution of KCl at an unadjusted pH of 7 lowers the repulsion between the bitumen droplets. The difference cannot be due to the electric properties of the systems because, from the experimentally determined zeta potentials, the repulsion should be more pronounced for bitumen in a NaCl/NaHCO₃ solution than for bitumen in a KCl solution. The lower repulsion between the bitumen droplets in a NaCl/NaHCO₃ solution is tentatively explained by the effect of pH and electrolyte on the distribution of natural surfactants on the bitumen water interface. More detailed discussion will be given in section 4.2.

It is believed that polymeric chains are adsorbed at the surface of the bitumen droplets and that these chains play a role in the high repulsion observed. From the tangential deviation observed in the experimental positions, the steric interaction mechanism is more likely than the enhanced electrostatic repulsion mechanism for bitumen droplets.

3.3. Effect of Clay

As mentioned in Chapter 1, the presence of fine clays in a bitumen-in-water emulsion increases the stability of the emulsion. It is therefore important to understand how clay interacts with the bitumen droplets. Since most of the clays found in oil sands are kaolinite clays, this type of clay will be used for the present study.

Experiments were first attempted with bitumen in a 0.04M KCl solution containing kaolinite (unadjusted pH of 7). It was found that the untreated kaolinite clay tended to quickly form large aggregates that made the colloidal particle scattering and the

hydrodynamic force balance experiments impossible to perform. Nevertheless, some experiments performed at a very low clay concentration of 20 to 40 ppm were successful using both colloidal particle scattering and hydrodynamic force balance techniques. Preliminary results obtained (not included in the thesis) indicate that, under these conditions, no or very little clay was adsorbed on the bitumen droplets. In addition, no difference in the interaction was observed. Therefore, it was decided to modify the contact angle of the kaolinite clay by treating it with asphaltenes extracted from the bitumen. The modification procedure is described in Chapter 2. A contact angle of approximately 125 to 130° was obtained, making the clay highly hydrophobic and thereby allowing the clays to partition more strongly on the bitumen/water interface.

The modification of the contact angle serves two purposes. First, it forces the clay to adhere to the bitumen droplets and second, it provides a kaolinite clay that is probably more similar to the surface-active clays (sometimes called biwettable clays) encountered in oil sands. In addition, the greater hydrophobic character of the asphaltenes-treated kaolinite clay reduces the aggregation problem and allows the use of a higher concentration of clay.

Colloidal particles scattering experiments were thus made using a bitumen emulsion containing the asphaltenes-treated clay. A solution of sodium chloride and sodium bicarbonate was used to better represent the conditions used in the extraction plant. More precisely, 0.025M of NaCl and 0.015M of NaHCO₃ were used, yielding a pH of approximately 8.5. The bitumen emulsion was prepared using a solution containing the electrolyte concentrations mentioned above and 400 ppm of the asphaltenes-treated clay. Once the bitumen emulsion was made, it was diluted with an approximately equal volume of a solution containing the same electrolyte concentrations but no clays. The mixture was then poured into the sample cell of the microcollider. The goal of this dilution step is to prepare an emulsion that has a relatively high amount of clay adsorbed on the bitumen droplets without having to

deal with the problems related to the suspended clay (opacity, aggregation of clay particles, etc.).

Using asphaltenes-treated clays and diluting the emulsion did not solve all the problems related to the aggregation of the clay particles. However, it allowed approximately thirty minutes of experimental work before the clay aggregates start to disturb the flow. This narrow window of operation time was fully exploited to generate 20-30 acceptable collisions, sufficient for data analysis.

The results obtained for bitumen in a 0.025M NaCl and 0.015M NaHCO₃ solution containing asphaltenes-treated kaolinite clay are given in Figure 3.16. The bitumen droplets used had an average radius of 2.4 μm. Based on the initial and final positions of the mobile droplet, clay does not seem to have a major effect on the repulsion forces. It is possible to detect a slightly higher repulsion, but at the same time, the results for the bitumen sample with clay are more scattered than for the bitumen sample without clay (cf. Figure 3.13). Therefore, it is not possible to conclude on the effect of clay simply by observing the scattering diagrams.

Although the effect of clay is not clearly visible on the scattering diagrams, clay was definitively adsorbed at the surface of the bitumen droplets. This adsorption was detected by the fact that 55% deuterium oxide (heavy water) was needed to make the bitumen droplets in presence of clay neutrally buoyant whereas an amount of 30 to 35% of deuterium oxide was sufficient in the absence of clay. Assuming that clay covers the bitumen droplet in a uniform layer, a force balance calculation using a kaolinite clay density of 2.63 kg/m³ [64] indicates that the clay layer would be approximately 15 nm thick. That thickness value means that if clay formed a uniform layer, only the very fine clay particles attached to the bitumen droplets. It is also possible that bigger clay particles or aggregates attached to the bitumen. In such a case, the clay would cover only part of the surface of the bitumen droplets. Obviously, the distribution of clay at the surface will affect how the bitumen droplets

interact with each other. Thus, an attempt was made to analyse the surface directly under a cryo-scanning electron microscope. Unfortunately, due to the presence of salt, the bitumen surface was obscured. It would have been possible to observe the bitumen surface using a solution free of any salt. However, experiments showed that the salt concentration had a large effect on the degree of adsorption of clay. For example, 70% deuterium oxide was needed to make bitumen droplets neutrally buoyant in a 0.01M KCl solution whereas 95% deuterium oxide was not sufficient for bitumen droplets in a 0.04M KCl solution. Therefore, due to concerns regarding the validity of SEM results obtained without any electrolyte in the solution, no such experiments were attempted.

Since the detailed information on the surface structure of the bitumen droplets in the presence of clay is not available, it was assumed that the bitumen surface is covered by a uniform layer of clay for simplicity. A new colloidal force model was developed to account for this geometry. It is referred to as the “shell and core” steric model, where the core refers to the bitumen droplet and the shell refers to the clay layer covering the droplet. Figure 3.17 gives a representation of the shell and core model.

The shell and core model was programmed to account for the electrostatic force, the van der Waals force and the steric force. The electrostatic force was calculated using Equation 1.7. In this case, the charge plane was placed on the outside surface of the clay. The steric force was obtained by Equation 1.8. The Hamaker constant in Equation 1.8 was assumed to be the average value of the Hamaker constants of clay-water-clay and bitumen-water-bitumen. The shear plane was assumed to be located at the outside surface of the clay layer. Finally, the van der Waals force was simply calculated by summing the contributions from two spheres of radius a made of bitumen and from two spheres of radius $a + L$ made of clay and subtracting the contribution from two spheres of radius a made of clay. It consists of an approximate calculation that neglects the clay to bitumen interactions. Since the actual distribution of clay at the bitumen/water interface is unknown, numerical integration

was disregarded. The van der Waals interaction based on the shell and core steric model can be written as:

$$F_{vdw} = -\frac{A_{b-w-b}a}{12(h+2L)^2}f\left(\frac{2\pi(h+2L)}{\lambda}\right) - \frac{A_{c-w-c}(a+L)}{12h^2}f\left(\frac{2\pi h}{\lambda}\right) + \frac{A_{c-w-c}a}{12(h+2L)^2}f\left(\frac{2\pi(h+2L)}{\lambda}\right) \quad (3.7)$$

In Equation 3.7, A_{b-w-b} is the Hamaker constant of bitumen-water-bitumen, A_{c-w-c} is the Hamaker constant of clay-water-clay, a is the radius of the bitumen droplet, L is the thickness of the clay layer, h is the separation distance between the outside surfaces of the two clay layers and $f(h)$ is the retardation function given by Equation 1.13.

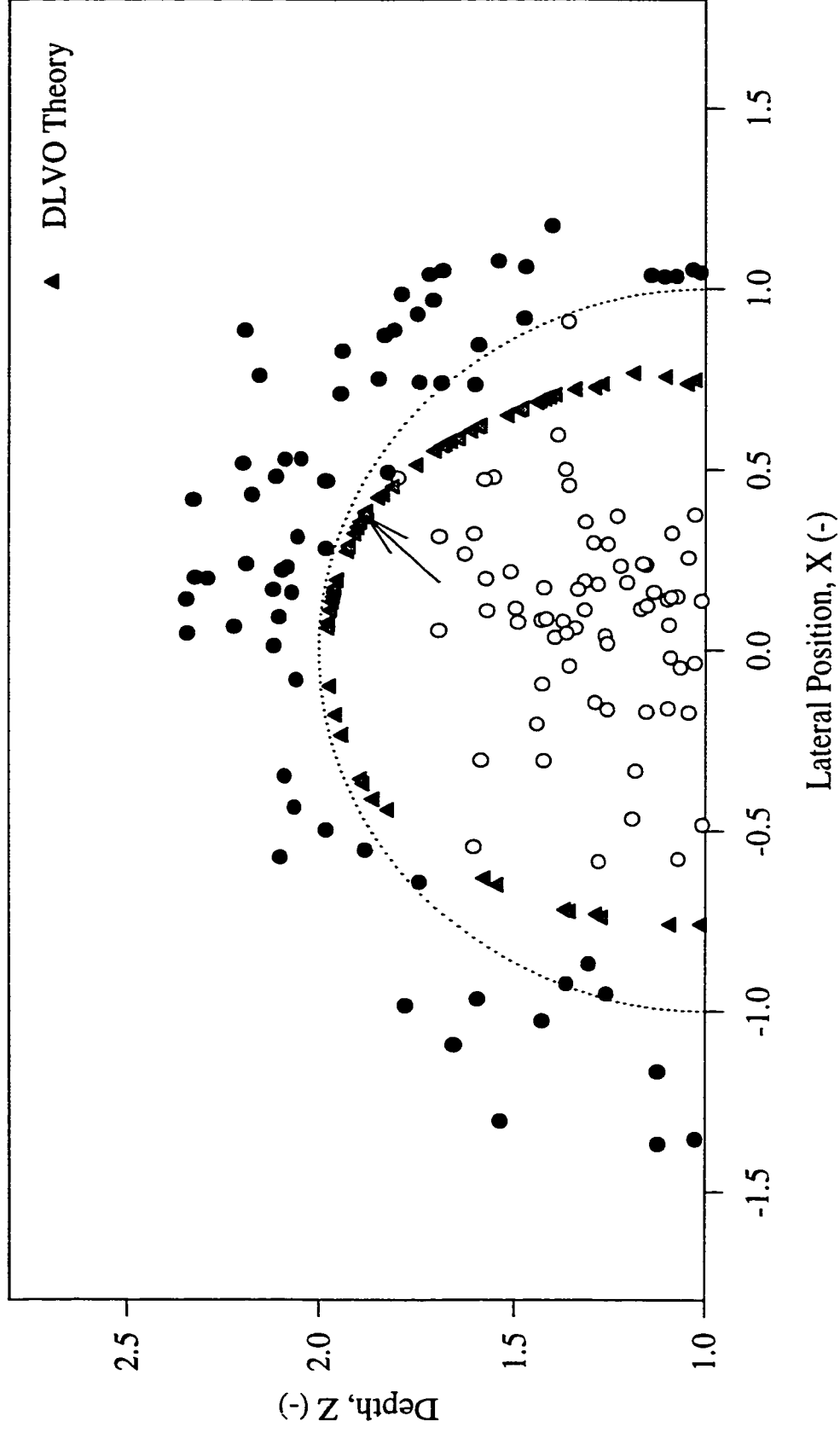
The results obtained with the shell and core model are provided in Figure 3.16. Calculations were made for a clay layer of 15 nm supplemented by a steric layer of 14 and 25 nm. Calculations of the theoretical final positions in the absence of a steric layer were also made but the model predicted aggregation at secondary minima for all points. The origin of this steric layer could be the asphaltene chains attached to the surface of the clay particles or the polymeric chains on the bitumen surface, which are not completely covered by clay particles. The scattering diagram in Figure 3.15 for bitumen droplet collisions in the absence of clays shows that the polymeric chains on the bitumen surface were mostly less than 22 nm in length. If they extend beyond the clay layer of 15 nm in thickness, the L_s value should be no more than 10 nm (7 nm to be precise). Since the majority of the collision data in Figure 3.16 indicate L_s values larger than 14 nm, the first hypothesis, i.e. asphaltene chains attached to the surface of clay, is probably correct.

The L_s values in Figure 3.16 also indicate that these asphaltene chains on the clay surface are generally longer than those observed on the untreated bitumen surface (cf.

Figure 3.14 or 3.15). As mentioned above, the polymeric chains on the untreated bitumen surface probably originate from asphaltenes as well. The difference in chain length implies different structures of precipitated asphaltenes used to coat clay particles and natural asphaltenes found on the bitumen surface.

One might argue that the above-mentioned conclusions are drawn on the basis of the simple shell-and-core model. In reality, clay particles may deposit on bitumen surface in the form of large aggregates instead of a uniform layer. This is quite possible. However, the collision trajectories are only affected by the *average* surface structures “scanned” by the moving droplet during a collision. Uneven surface structures do not usually alter the qualitative interpretation of the collision data.

Figure 3.1: Scattering Diagram for Deasphalted Bitumen in 0.04M KCl - DLVO Theory



The white and black circles are respectively the experimental initial and final positions of the mobile droplet. The gray triangles are the theoretical final positions calculated using the DLVO theory. Parameters used: $A = 2.7 \times 10^{-21} \text{ J}$; $\zeta = -80 \text{ mV}$; $\lambda = 100 \text{ nm}$ and $a = 4.46 \text{ }\mu\text{m}$. $ka = 2930$, $\text{pH} = 7$.

Figure 3.2: SEM Image of Deasphalted Bitumen

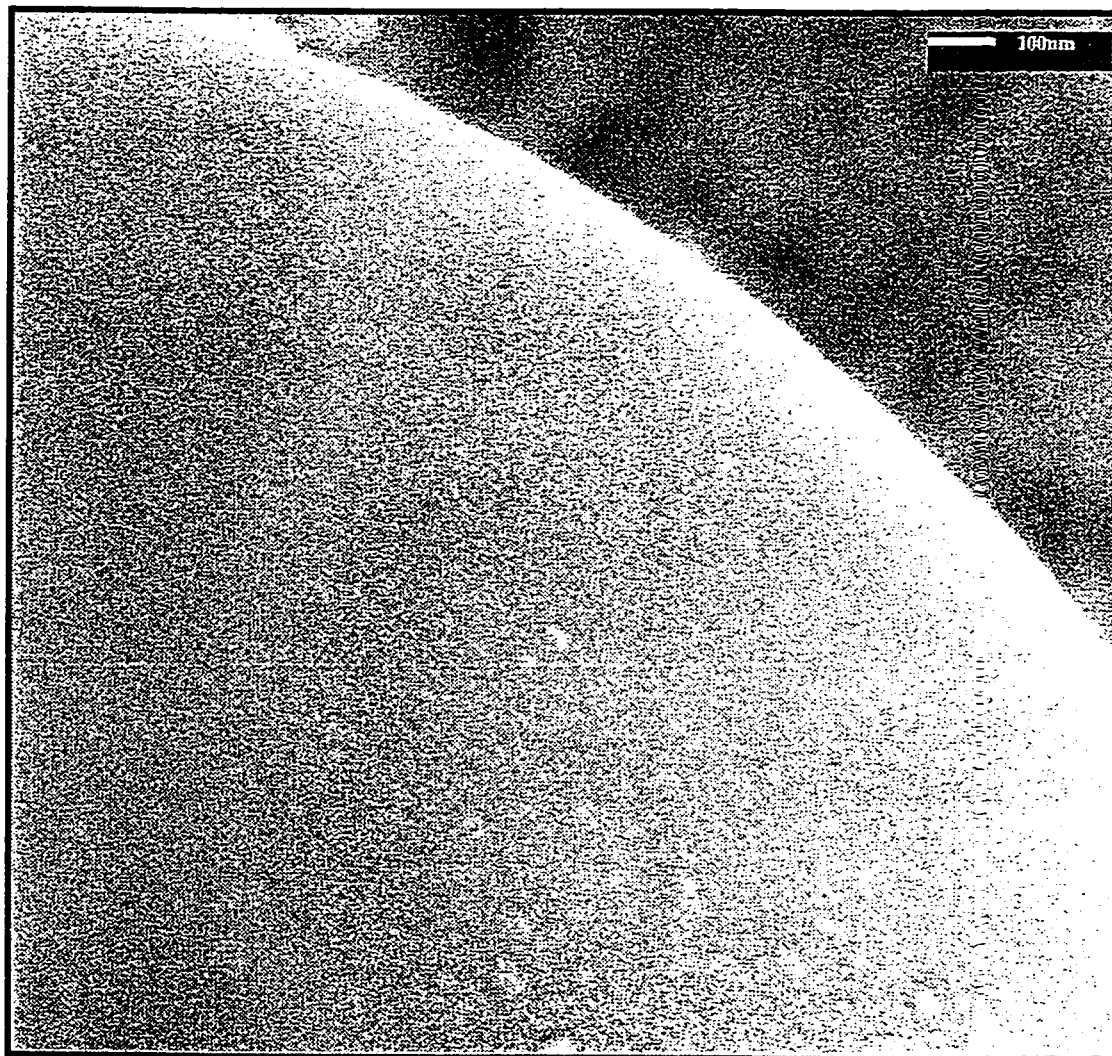


Figure 3.3: Single Disk Model

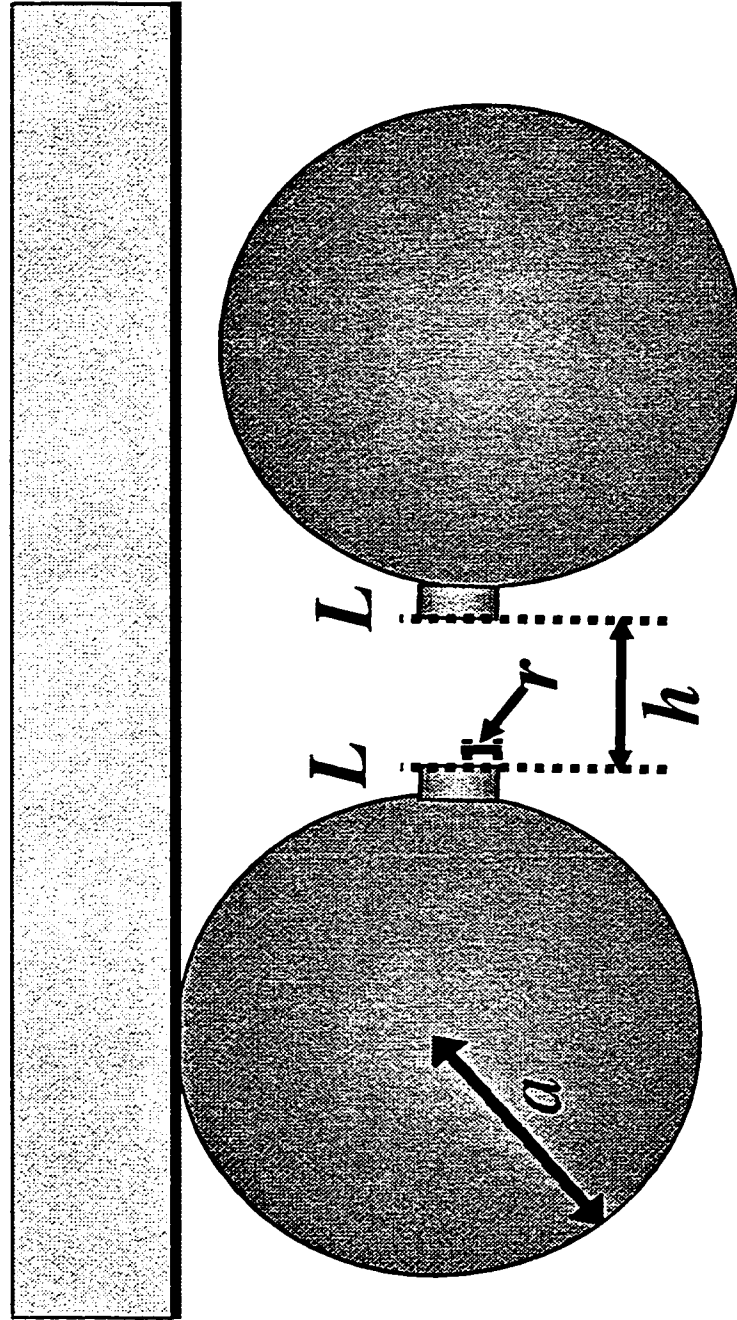
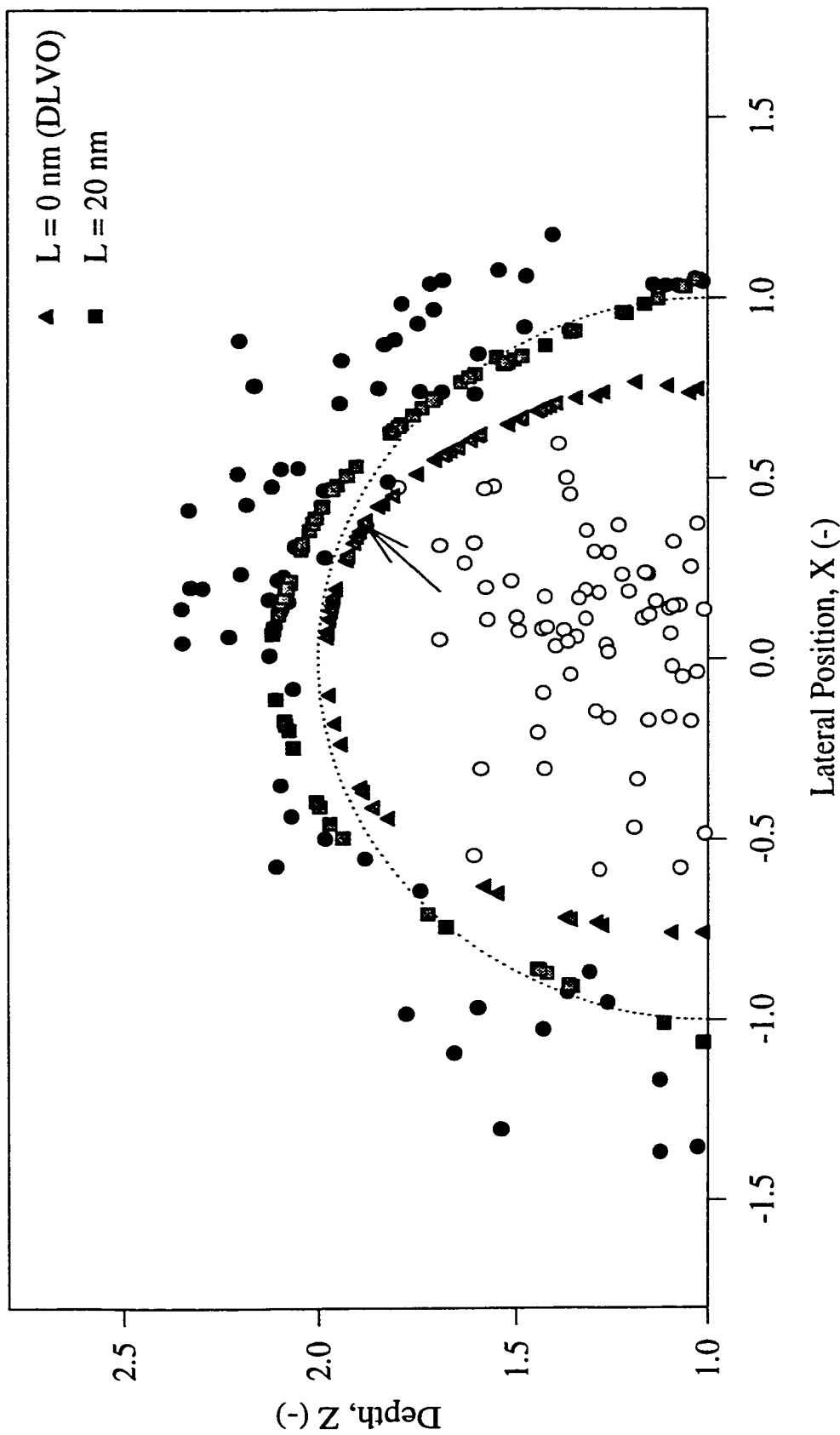


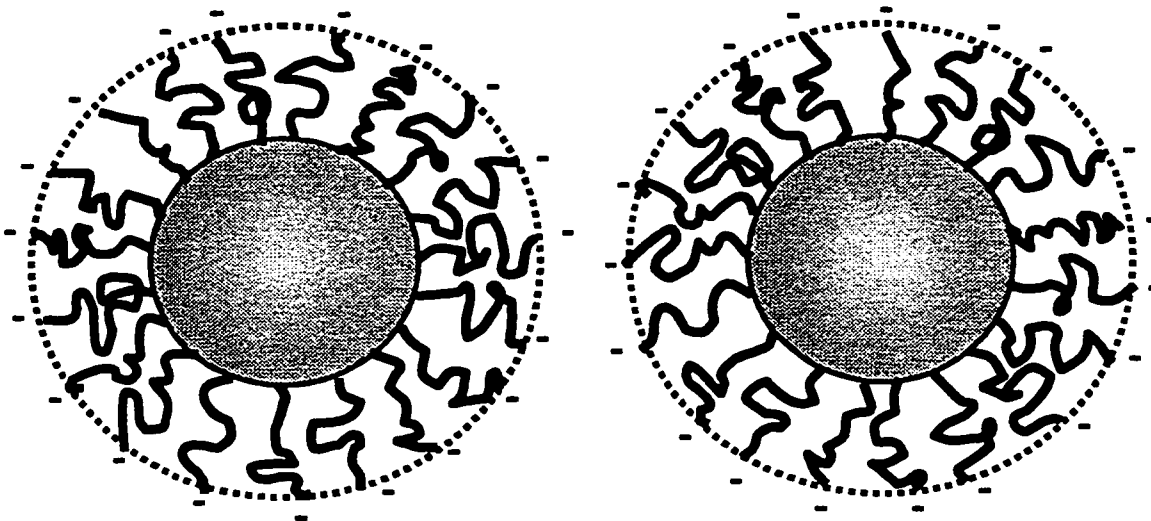
Figure 3.4: Scattering Diagram for Deasphalted Bitumen in 0.04M KCl - Single Disk Model



The white and black circles are respectively the experimental initial and final positions of the mobile droplet. The gray symbols are the theoretical final positions calculated using the DLVO theory (triangles) and the single disk model (squares). Parameters used: $A = 2.7 \times 10^{-21}$ J; $\zeta = -80$ mV; $\lambda = 100$ nm; $a = 4.46$ μ m; $r = 25$ nm and $L = 20$ nm. $k_a = 2930$. $pH = 7$. 100% water in protrusions.

Figure 3.5: Mechanisms for Repulsion due to Polymeric Chain Adsorption

Enhanced Electrostatic Repulsion



Steric Repulsion

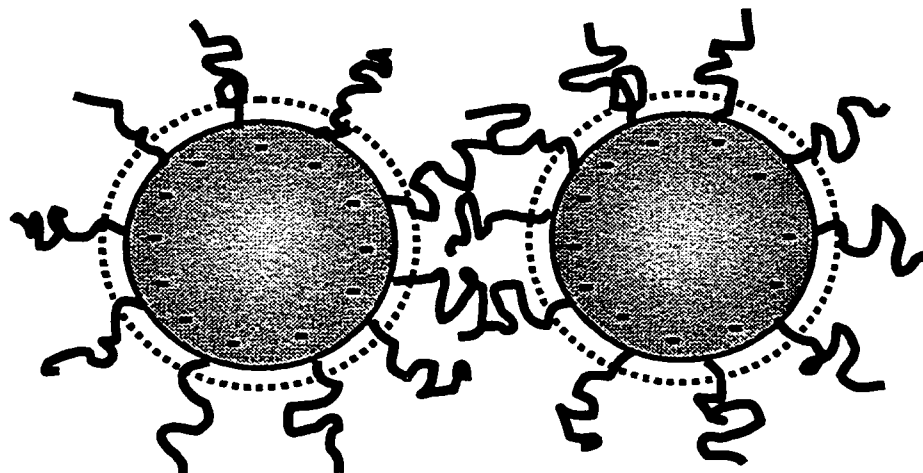
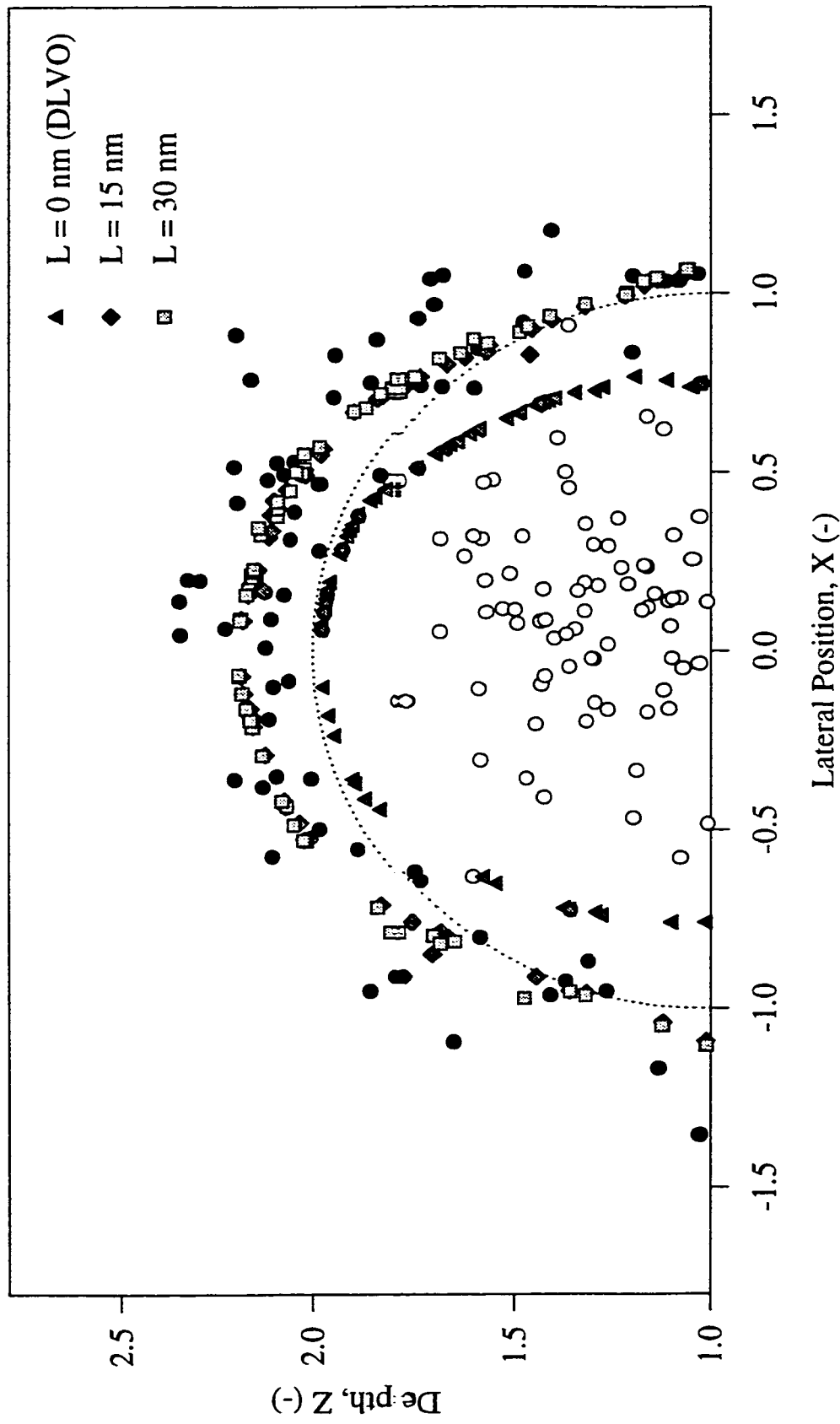
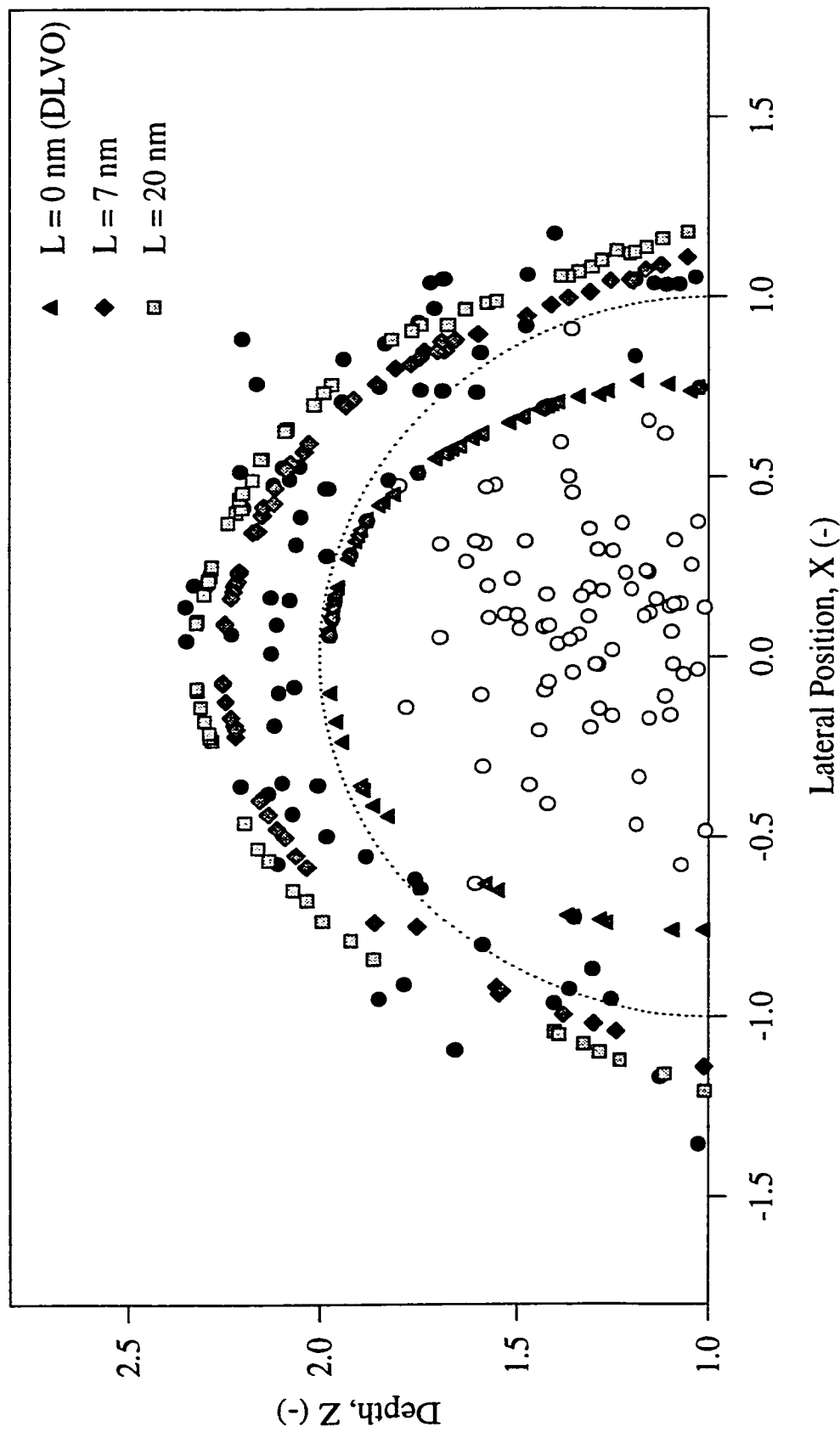


Figure 3.6: Scattering Diagram for Deasphalted Bitumen in 0.04M KCl - Enhanced Electrostatic Repulsion Model



The white and black circles are respectively the experimental initial and final positions of the mobile droplet. The gray symbols are the theoretical final positions calculated using the DLVO theory (diamonds and squares). Parameters used: $A = 2.7 \times 10^{-21} \text{ J}$; $\zeta = -80 \text{ mV}$; $\lambda = 100 \text{ nm}$; $a = 4.46 \text{ }\mu\text{m}$; $L = 15 \text{ nm}$ (diamonds) and $L = 30 \text{ nm}$ (squares). $\kappa a = 2930$, $\text{pH} = 7$.

Figure 3.7: Scattering Diagram for Deasphalted Bitumen in 0.04M KCl - Steric Repulsion Model



The white and black circles are respectively the experimental initial and final positions of the mobile droplet. The gray symbols are the theoretical final positions calculated using the DLVO theory (triangles) and the steric repulsion model (diamonds and squares). Parameters used: $A = 2.7 \times 10^{-21}$ J; $\zeta = -80$ mV; $\lambda = 100$ nm; $a = 4.46$ μ m; $L = 7$ nm (diamonds) and $L = 20$ nm (squares). $\kappa a = 2930$, $\text{pH} = 7$.

Figure 3.8: SEM Image of Untreated Bitumen

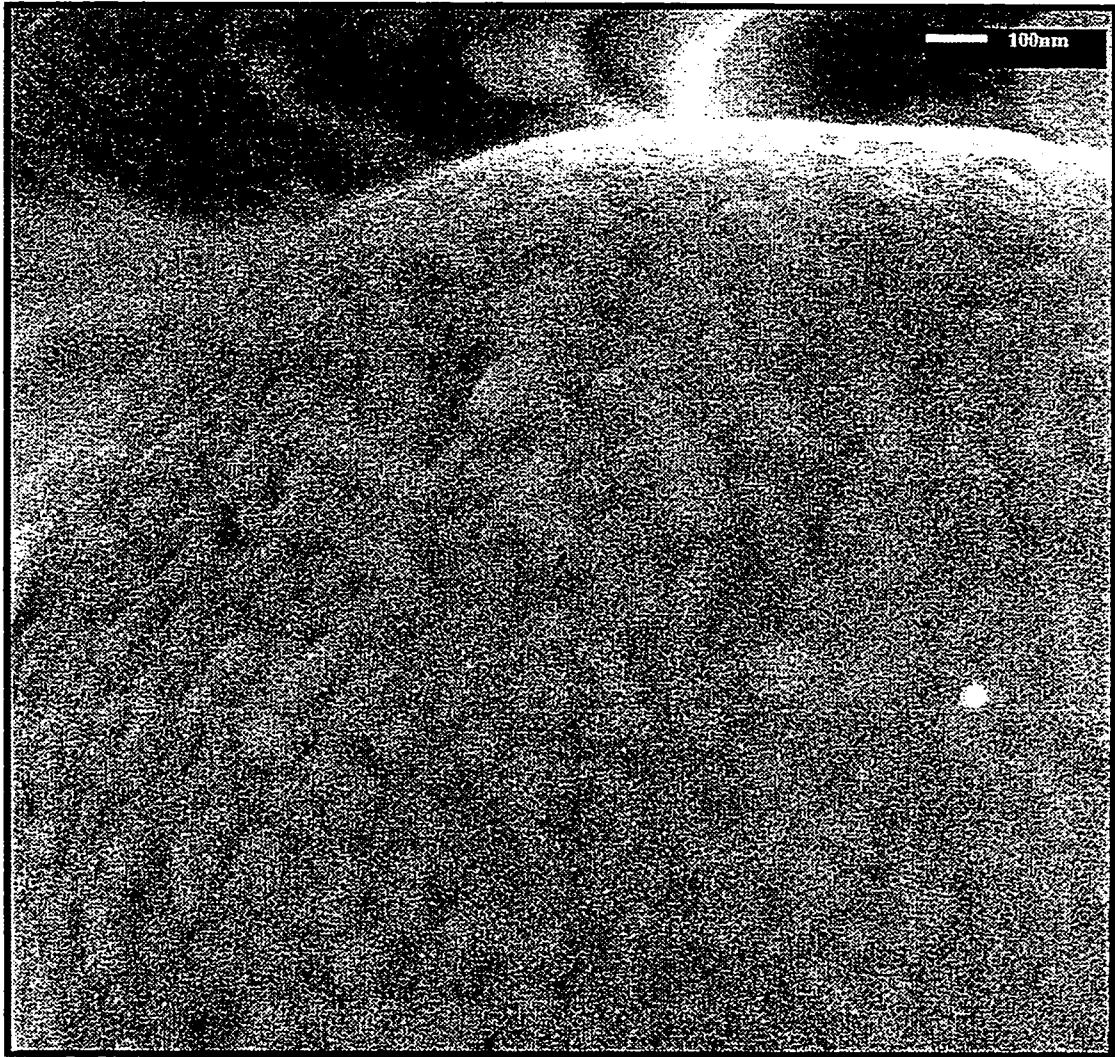
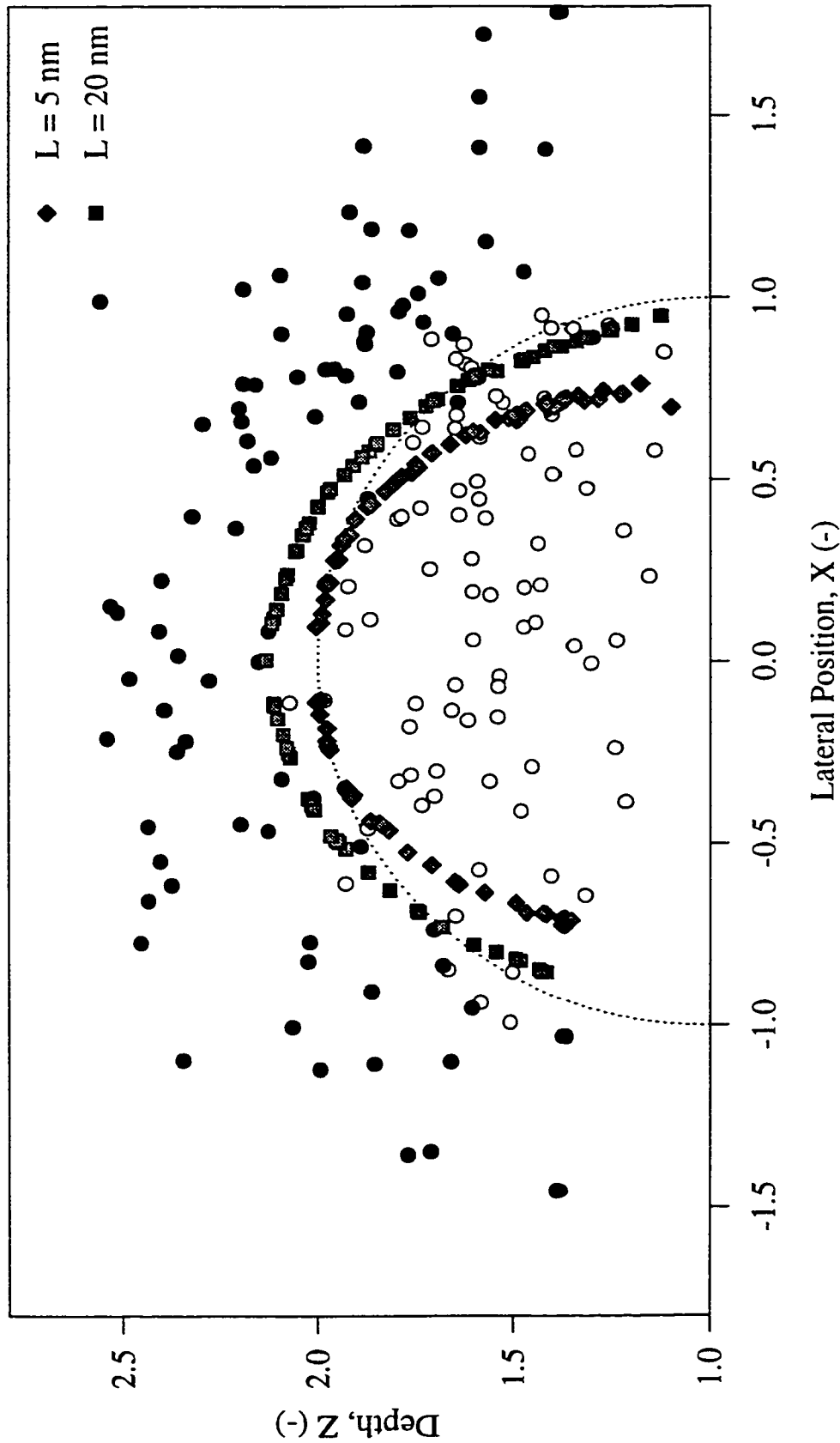
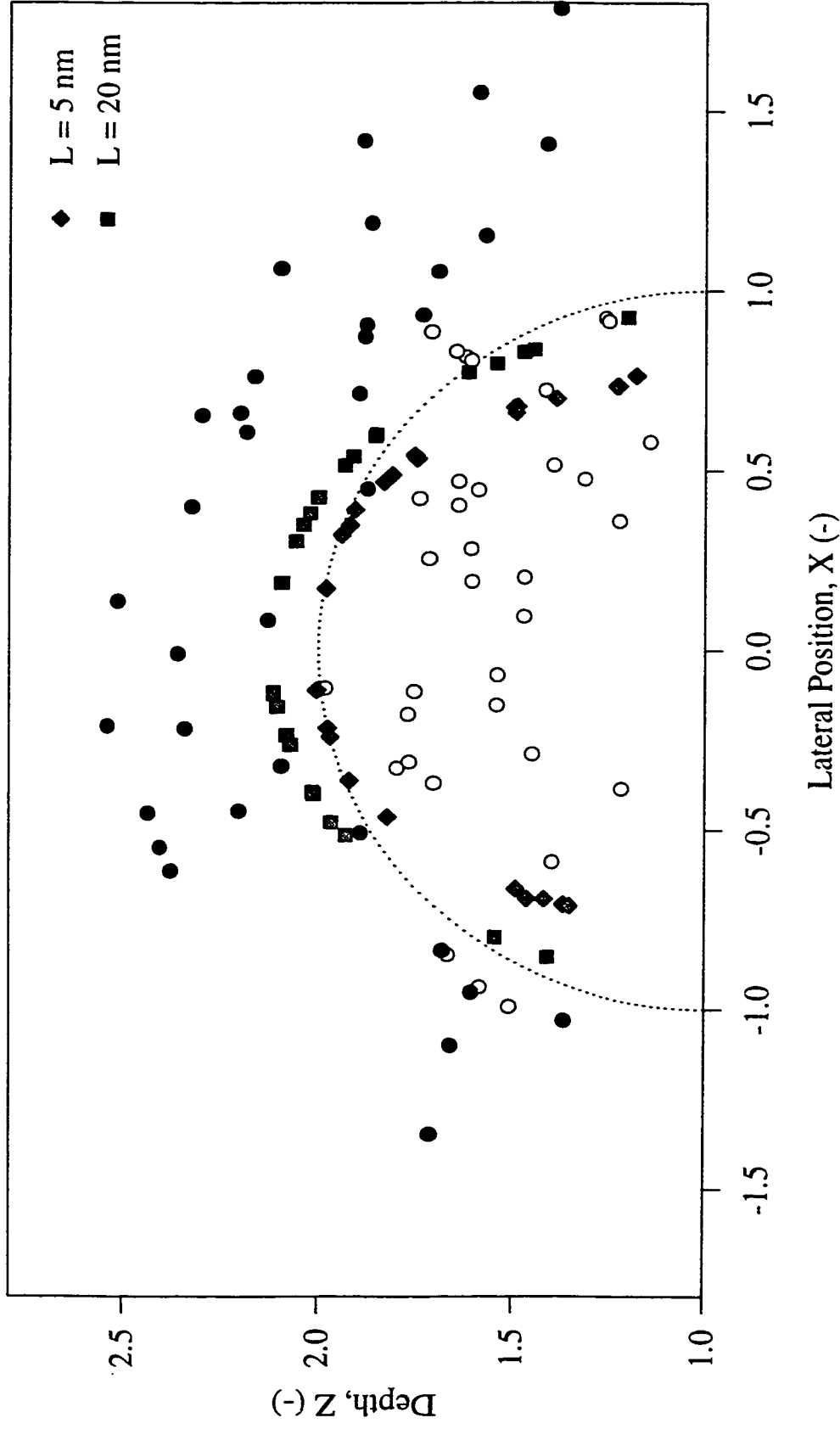


Figure 3.9a: Scattering Diagram for Bitumen in 0.04M KCl - Single Disk Model (after 1st screening)



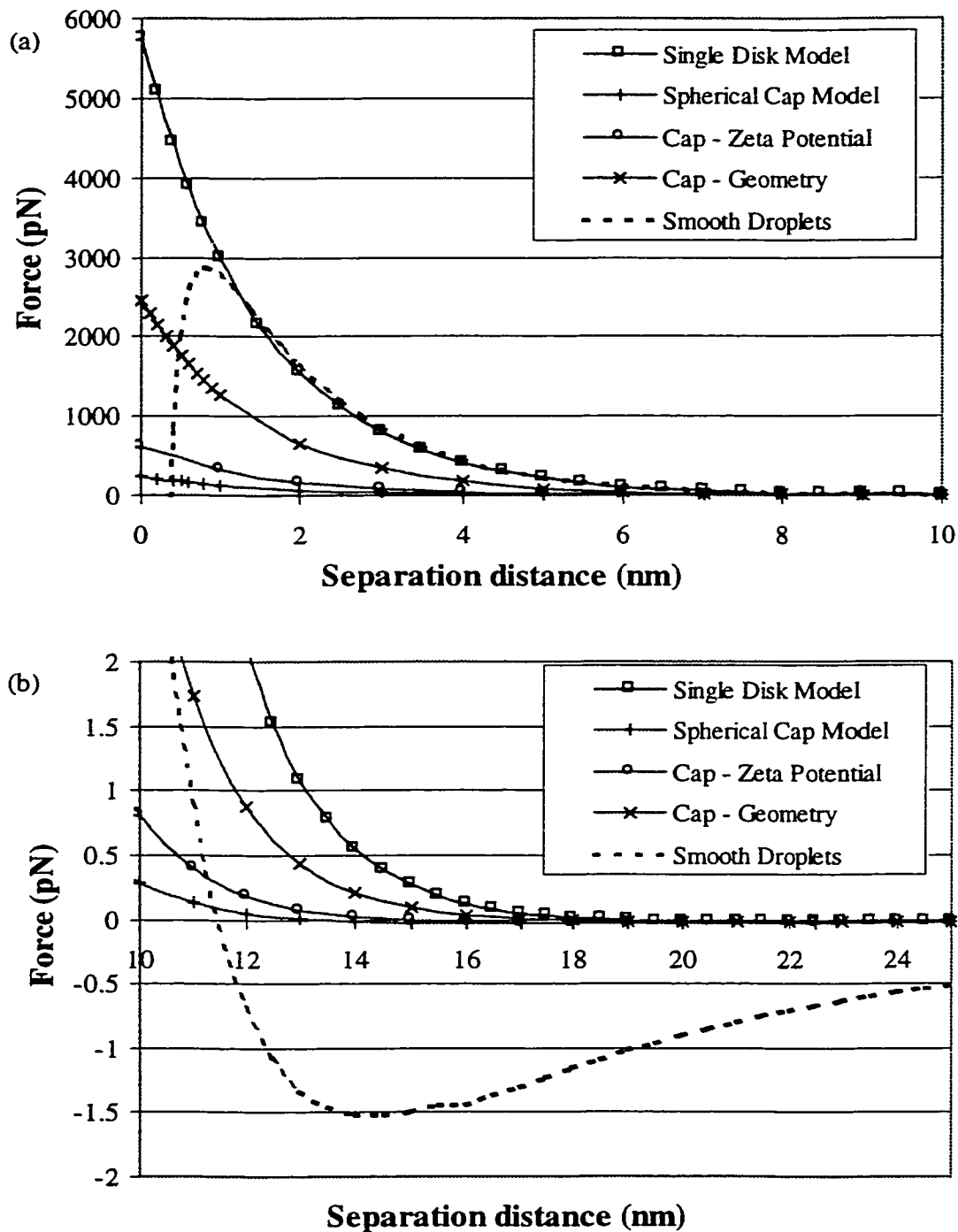
The white and black circles are respectively the experimental initial and final positions of the mobile droplet. The gray symbols are the theoretical final positions calculated using the single disk model (diamonds and squares). Parameters used: $A = 3.0 \times 10^{-21}$ J; $\zeta = -30$ mV; $\lambda = 100$ nm; $a = 2.72$ μ m; $r = 60$ nm; $L = 5$ nm (diamonds) and $L = 20$ nm (squares). $ka = 1787$, $\text{pH} = 7$, 100% water in protrusions.

Figure 3.9b: Scattering Diagram for Bitumen in 0.04M KCl - Single Disk Model (after 2nd screening)



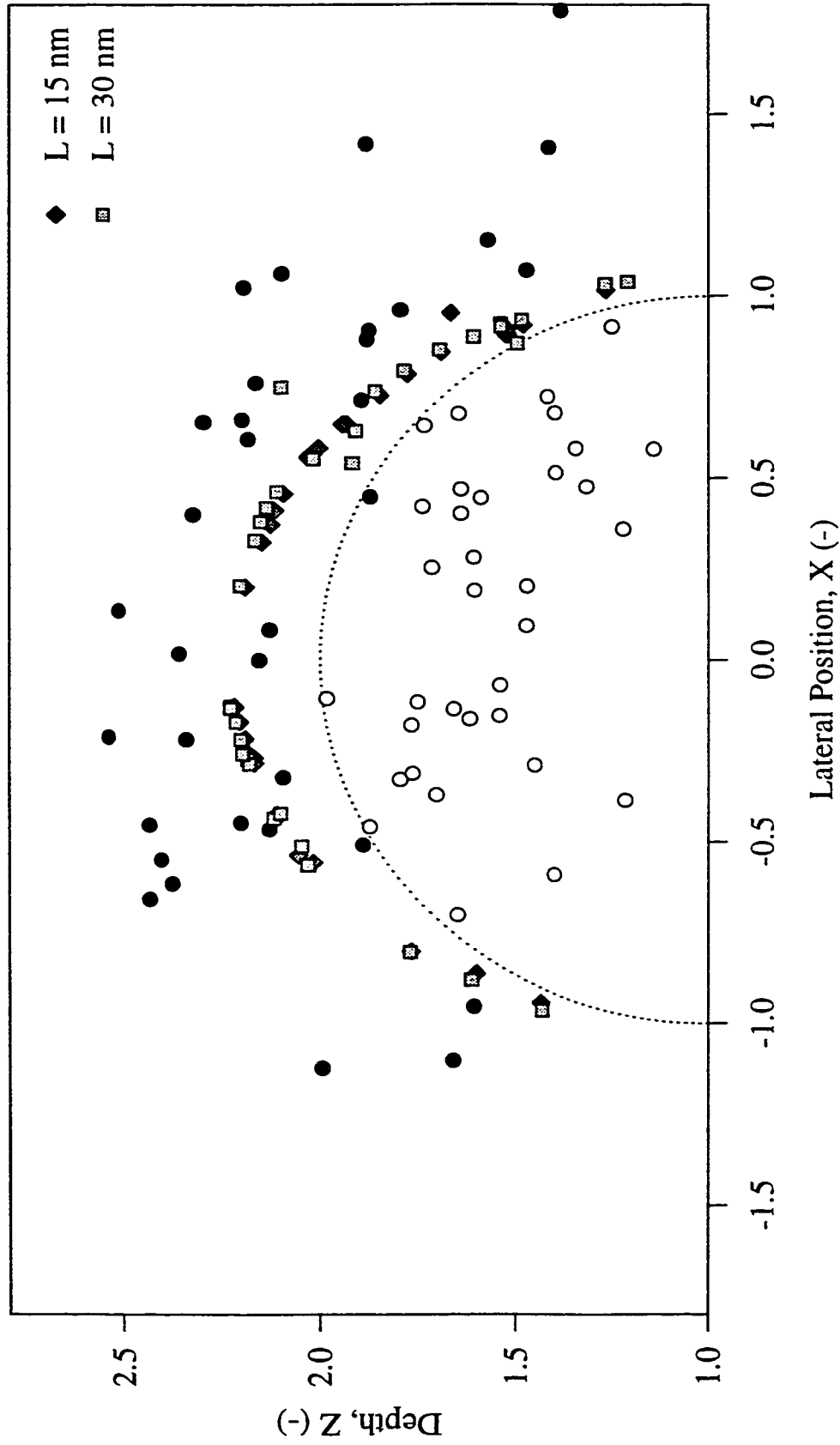
The white and black circles are respectively the experimental initial and final positions of the mobile droplet. The gray symbols are the theoretical final positions calculated using the single disk model (diamonds and squares). Parameters used: $A = 3.0 \times 10^{-21}$ J; $\zeta = -30$ mV; $\lambda = 100$ nm; $a = 2.72$ μ m; $r = 60$ nm; $L = 5$ nm (diamonds) and $L = 20$ nm (squares). $\kappa a = 1787$, $\text{pH} = 7$, 100% water in protrusions.

Figure 3.10: Force Profiles - Comparison of Roughness Models



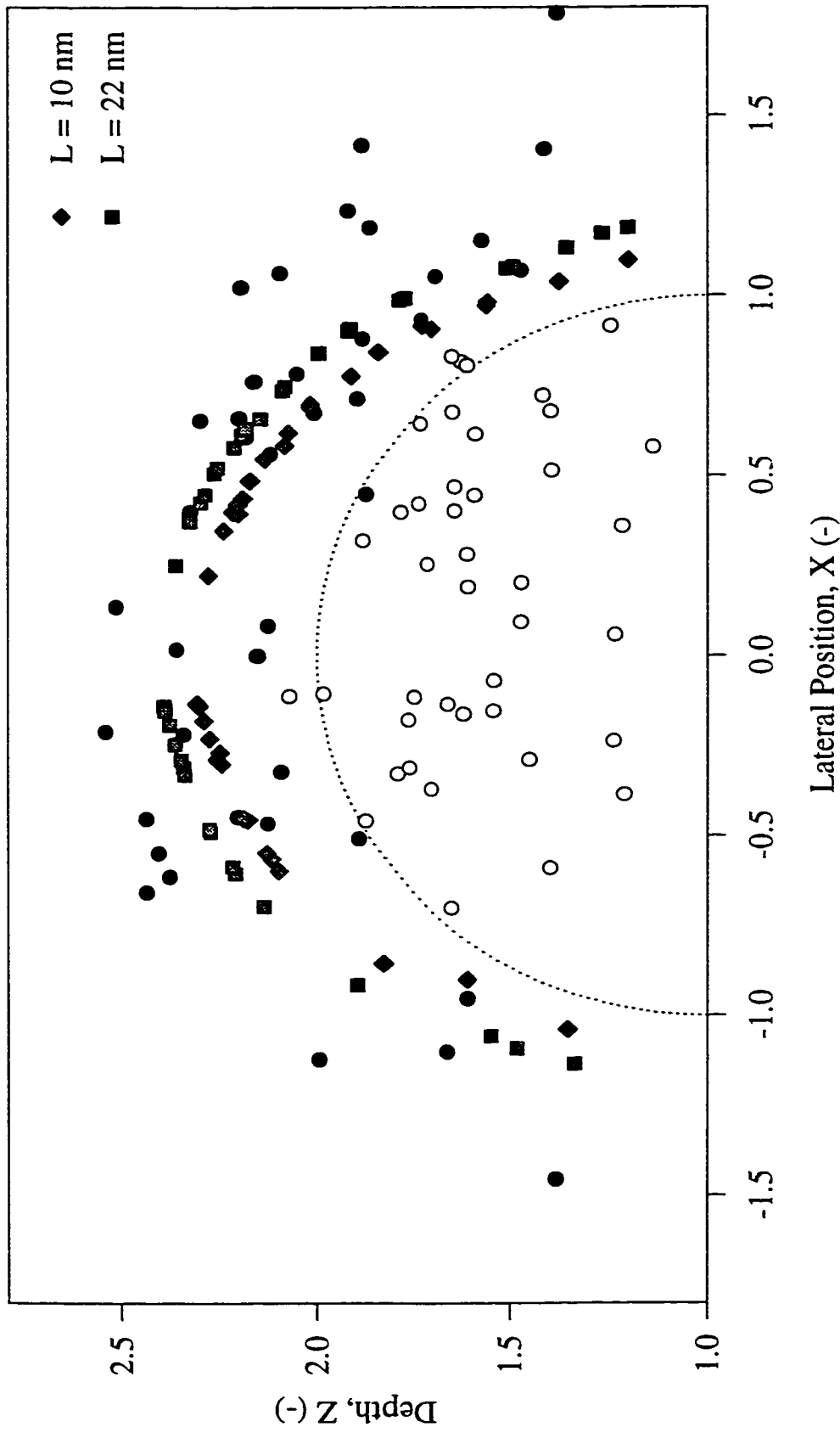
Parameters used: $a = 2.7 \mu\text{m}$, $A_{s-s} = 3.0 \times 10^{-21} \text{ J}$, $A_{d-d} = A_{d-s} = 0$ and $\lambda = 100 \text{ nm}$. Single disk model and spherical cap model: $\zeta = -30 \text{ mV}$, $r = 60 \text{ nm}$, $L = 25 \text{ nm}$. Cap - zeta potential: $\zeta = -50 \text{ mV}$, $r = 60 \text{ nm}$, $L = 25 \text{ nm}$. Cap - geometry: $\zeta = -30 \text{ mV}$, $r = 100 \text{ nm}$, $L = 5 \text{ nm}$. Smooth Droplets: $\zeta = -30 \text{ mV}$. Protrusions made of 100% water. 0.04M KCl solution (pH = 7).

Figure 3.11: Scattering Diagram for Bitumen in 0.04M KCl - Enhanced Electrostatic Repulsion Model



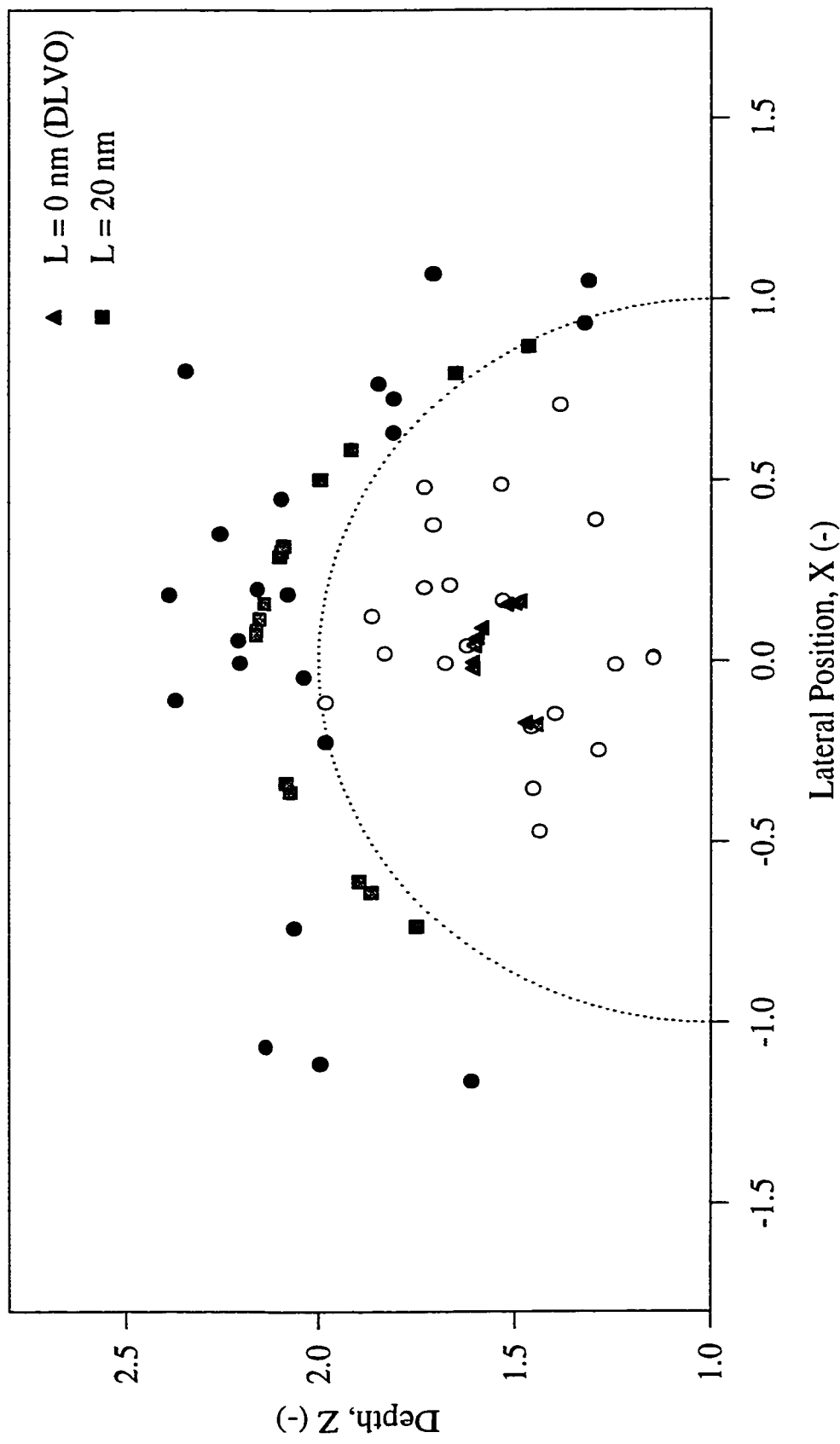
The white and black circles are respectively the experimental initial and final positions of the mobile droplet. The gray symbols are the theoretical final positions calculated using the enhanced electrostatic repulsion model (diamonds and squares). Parameters used: $A = 3.0 \times 10^{-21}$ J; $\zeta = -30$ mV; $\lambda = 100$ nm; $a = 2.72$ μm ; $L = 15$ nm (diamonds) and $L = 30$ nm (squares). $\kappa a = 1787$. $\text{pH} = 7$.

Figure 3.12: Scattering Diagram for Bitumen in 0.04M KCl - Steric Repulsion Model



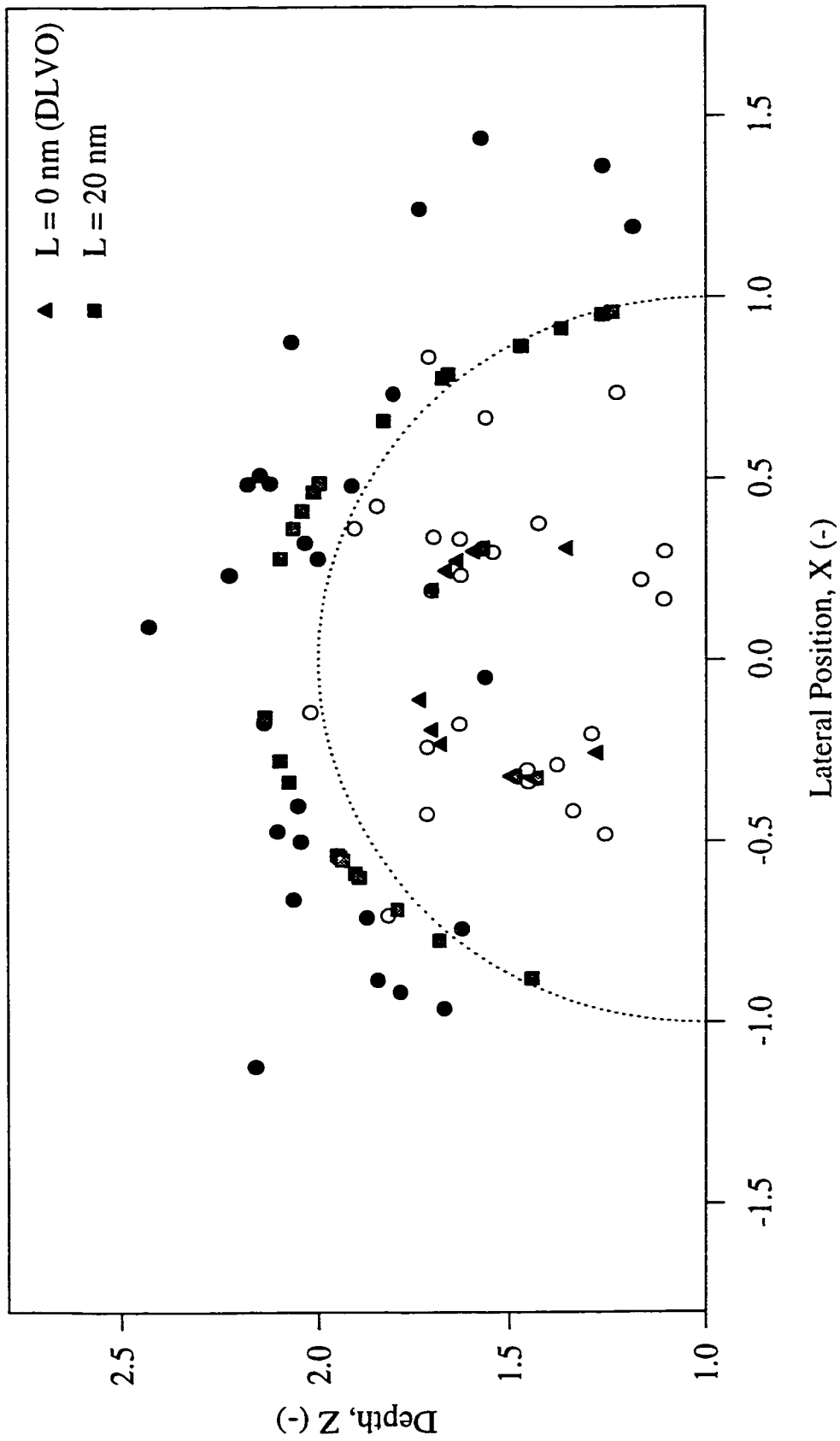
The white and black circles are respectively the experimental initial and final positions of the mobile droplet. The gray symbols are the theoretical final positions calculated using the steric repulsion model (diamonds and squares). Parameters used: $A = 3.0 \times 10^{-21} \text{ J}$; $\zeta = -30 \text{ mV}$; $\lambda = 100 \text{ nm}$; $a = 2.72 \text{ }\mu\text{m}$; $L = 10 \text{ nm}$ (diamonds) and $L = 22 \text{ nm}$ (squares). $\kappa a = 1787$, $\text{pH} = 7$.

Figure 3.13a: Scattering Diagram for Bitumen in 0.025M NaCl + 0.015M NaHCO₃ - DLVO and Single Disk Models



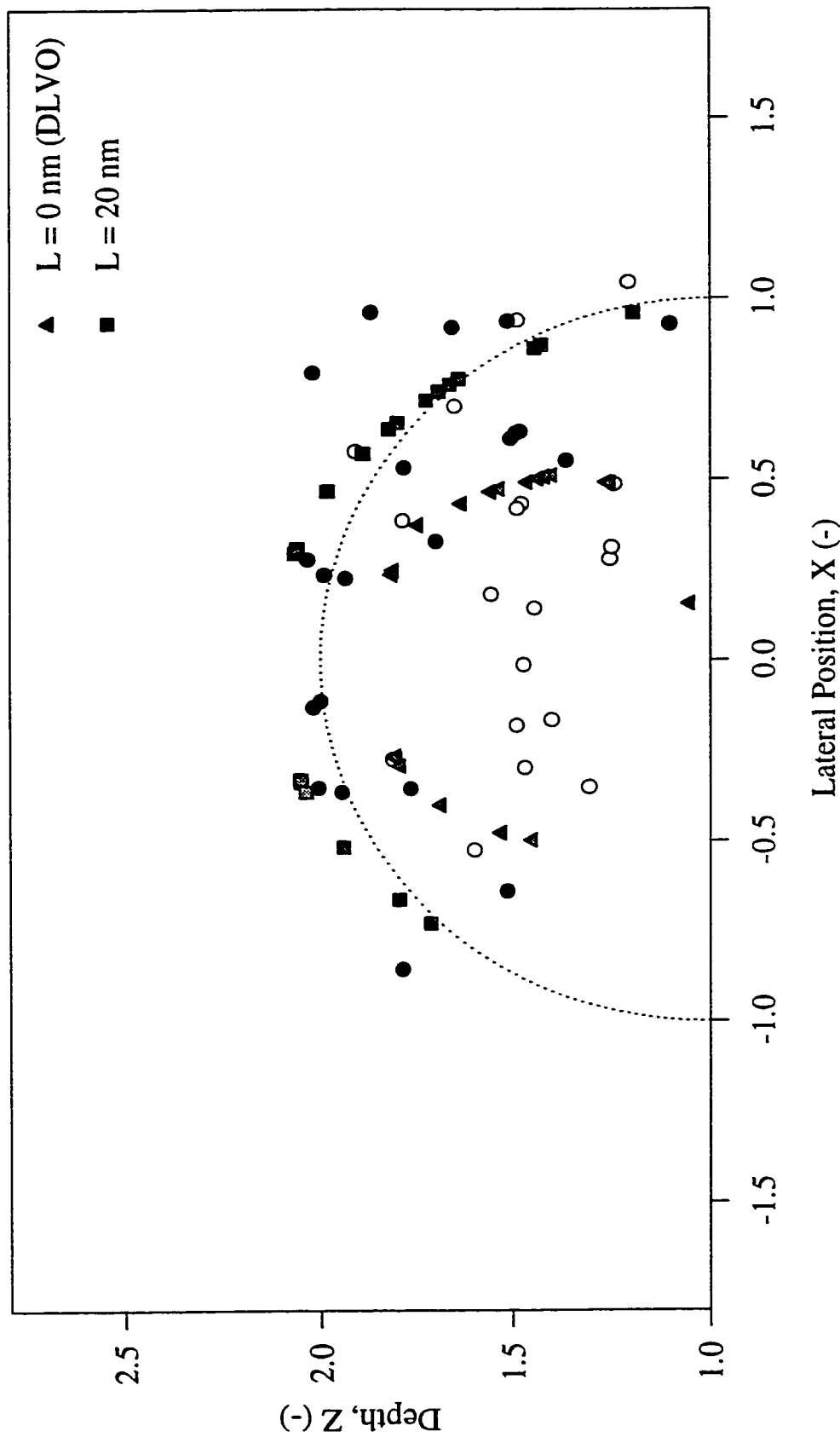
The white and black circles are respectively the experimental initial and final positions of the mobile droplet. The gray symbols are the theoretical final positions calculated using the DLVO theory (triangles) and the single disk model (squares). Parameters used: $A = 3.0 \times 10^{-21}$ J; $\zeta = -55$ mV; $\lambda = 100$ nm; $a = 2.52$ μ m; $r = 60$ nm; $L = 20$ nm (squares). $\kappa a = 1656$. pH = 8.5. 100% water in protrusions.

Figure 3.13b: Scattering Diagram for Bitumen in 0.025M NaCl + 0.015M NaHCO₃ - DLVO and Single Disk Models



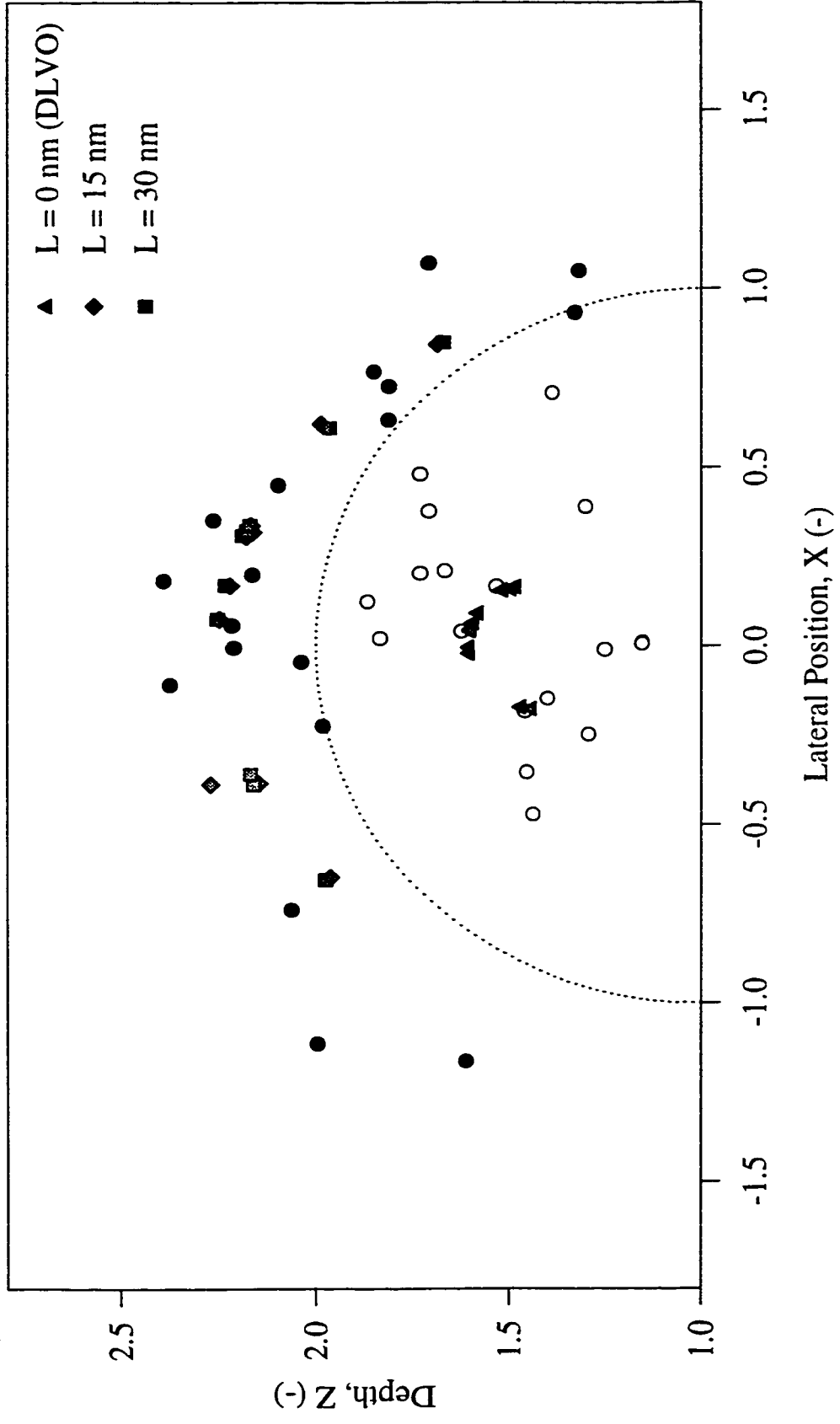
The white and black circles are respectively the experimental initial and final positions of the mobile droplet. The gray symbols are the theoretical final positions calculated using the DLVO theory (triangles) and the single disk model (squares). Parameters used: $A = 3.0 \times 10^{-21}$ J; $\zeta = -55$ mV; $\lambda = 100$ nm; $a = 2.81$ μ m; $r = 60$ nm; $L = 20$ nm (squares). $\kappa a = 1846$, pH = 8.5, 100% water in protrusions.

Figure 3.13c: Scattering Diagram for Bitumen in 0.025M NaCl + 0.015M NaHCO₃ - DLVO and Single Disk Models



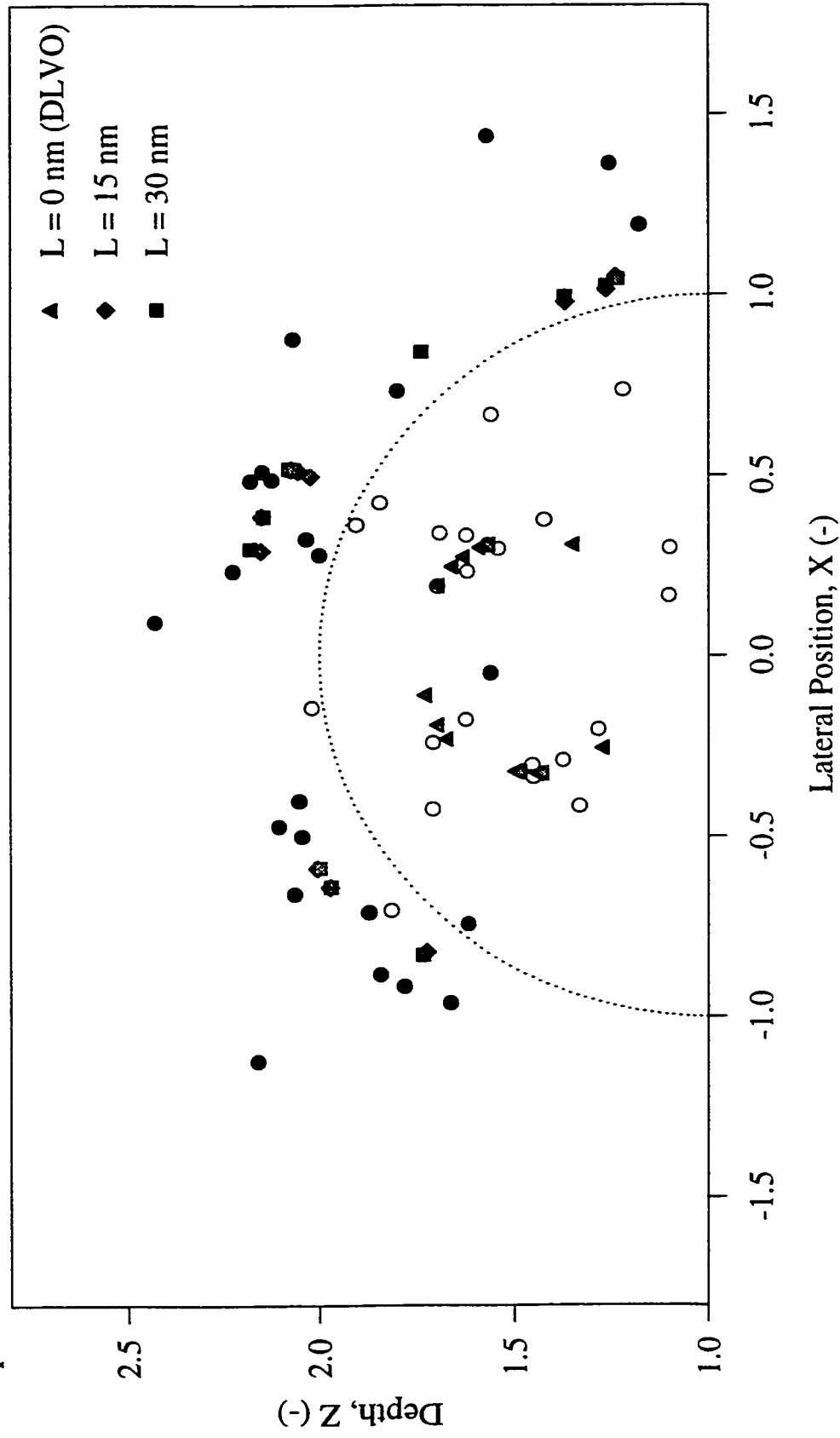
The white and black circles are respectively the experimental initial and final positions of the mobile droplet. The gray symbols are the theoretical final positions calculated using the DLVO theory (triangles) and the single disk model (squares). Parameters used: $A = 3.0 \times 10^{-21}$ J; $\zeta = -55$ mV; $\lambda = 100$ nm; $a = 3.55$ μ m; $r = 60$ nm; $L = 20$ nm (squares). $\kappa a = 2332$, pH = 8.5, 100% water in protrusions.

Figure 3.14a: Scattering Diagram for Bitumen in 0.025M NaCl + 0.015M NaHCO₃ - Enhanced Electrostatic Repulsion Model



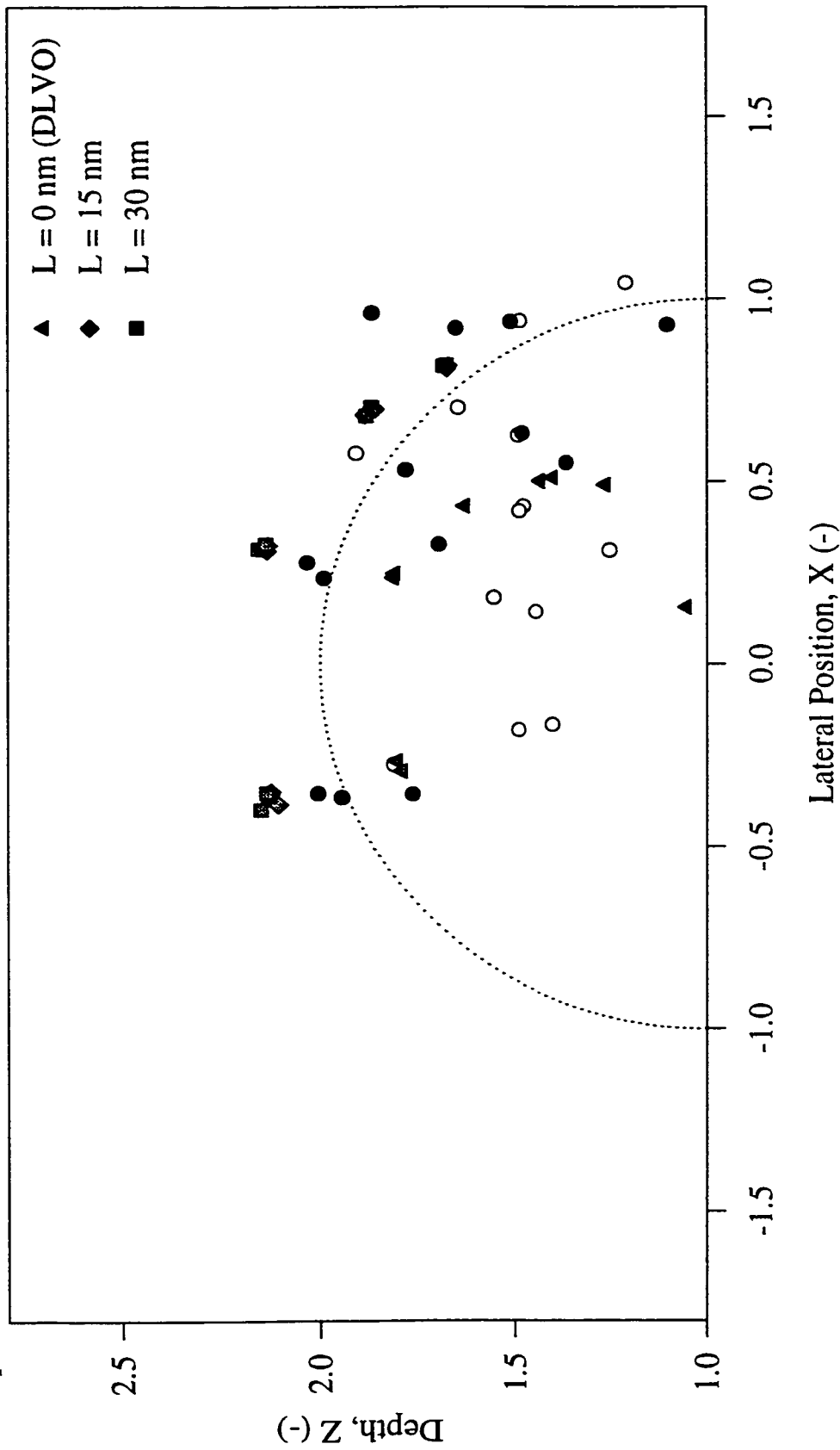
The white and black circles are respectively the experimental initial and final positions of the mobile droplet. The gray symbols are the theoretical final positions calculated using the DLVO theory (triangles) and the enhanced electrostatic repulsion model (diamonds and squares). Parameters used: $A = 3.0 \times 10^{-21}$ J; $\zeta = -55$ mV; $\lambda = 100$ nm; $a = 2.52$ μ m; $L = 15$ nm (diamonds) and $L = 30$ nm (squares). $\kappa a = 1656$, $\text{pH} = 8.5$.

Figure 3.14b: Scattering Diagram for Bitumen in 0.025M NaCl + 0.015M NaHCO₃ - Enhanced Electrostatic Repulsion Model



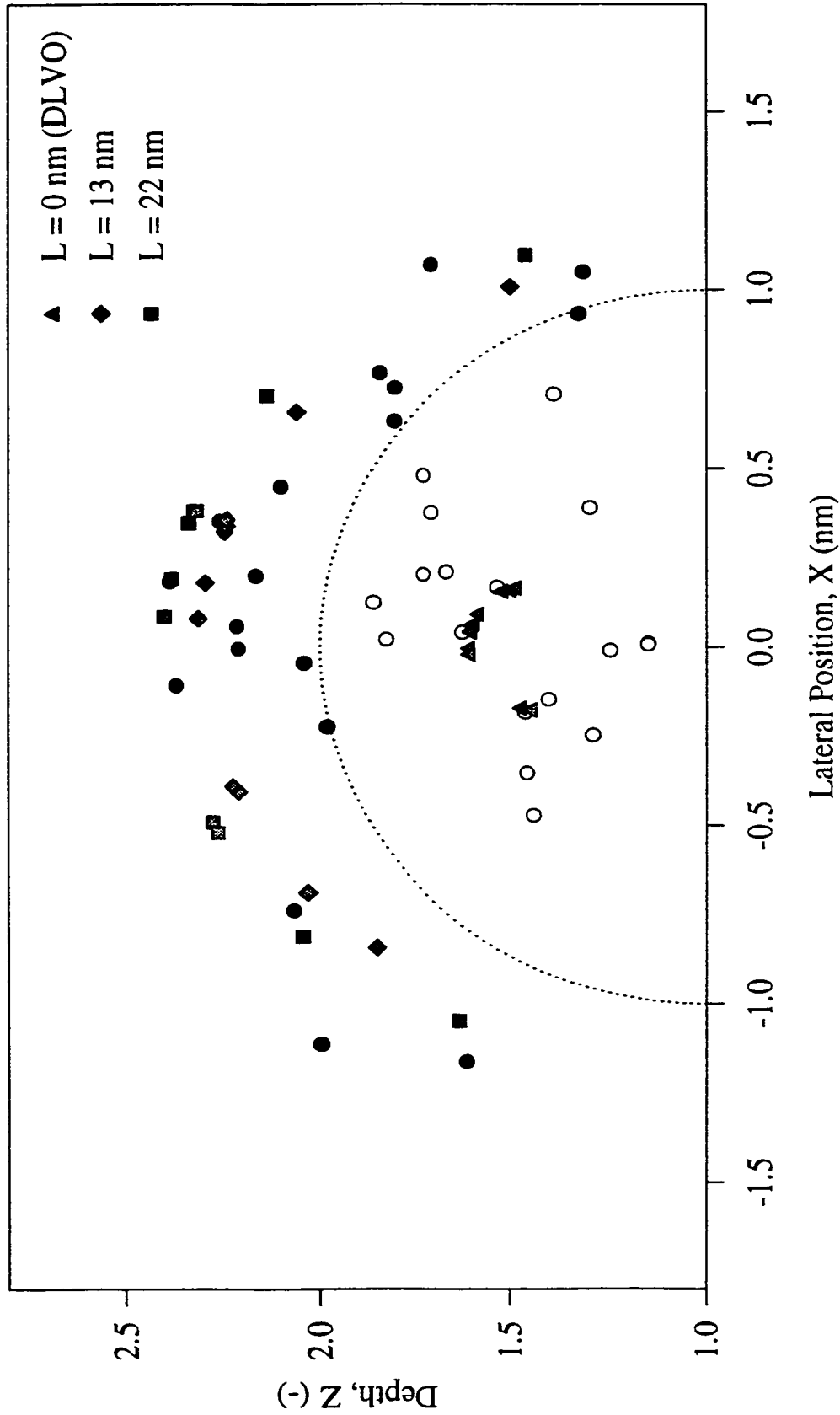
The white and black circles are respectively the experimental initial and final positions of the mobile droplet. The gray symbols are the theoretical final positions calculated using the DLVO theory (triangles) and the enhanced electrostatic repulsion model (diamonds and squares). Parameters used: $A = 3.0 \times 10^{-21}$ J; $\zeta = -55$ mV; $\lambda = 100$ nm; $a = 2.81$ μ m; $L = 15$ nm (diamonds) and $L = 30$ nm (squares). $\kappa a = 1846$, pH = 8.5.

Figure 3.14c: Scattering Diagram for Bitumen in 0.025M NaCl + 0.015M NaHCO₃ - Enhanced Electrostatic Repulsion Model



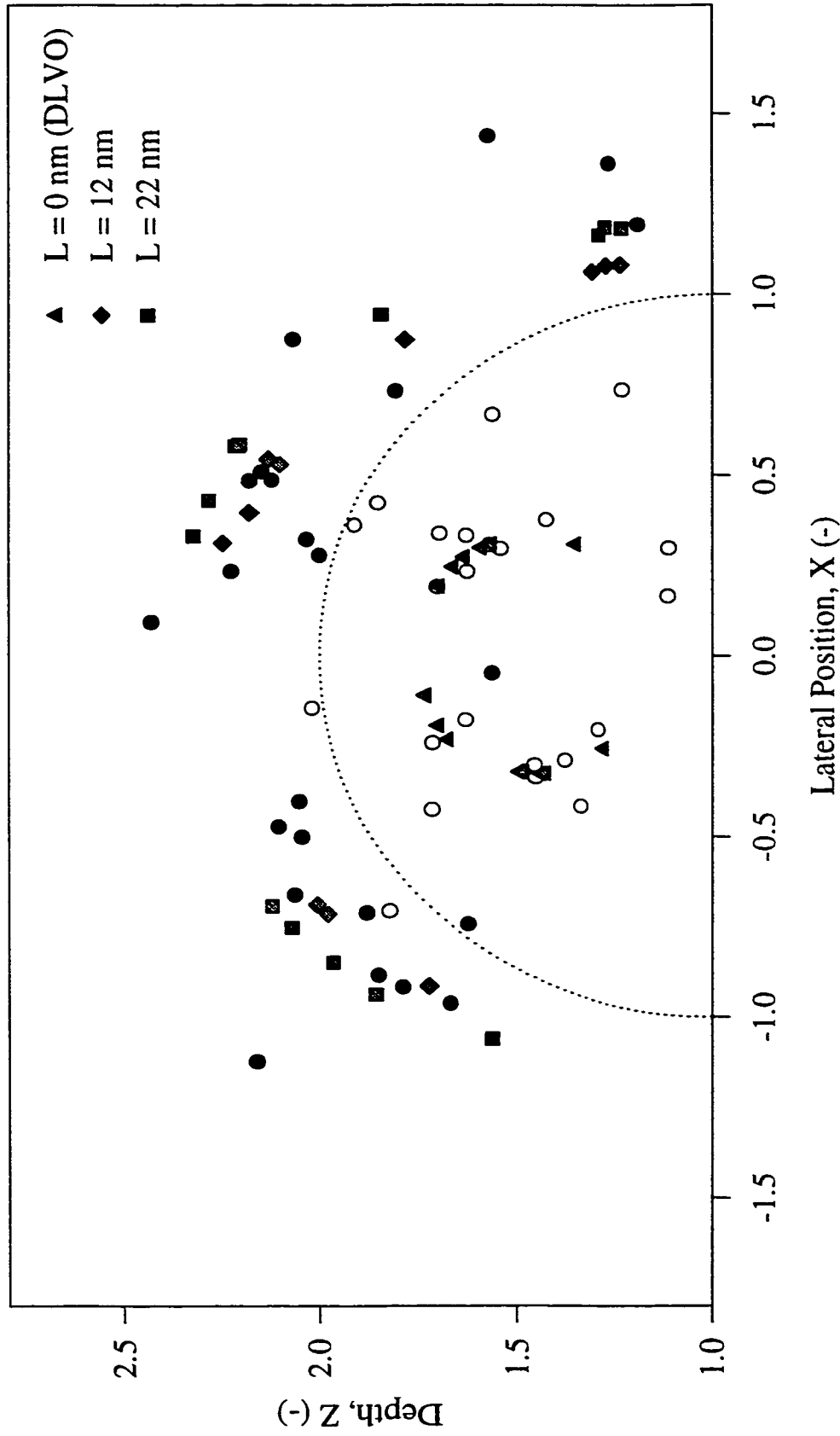
The white and black circles are respectively the experimental initial and final positions of the mobile droplet. The gray symbols are the theoretical final positions calculated using the DLVO theory (triangles) and the enhanced electrostatic repulsion model (diamonds and squares). Parameters used: $A = 3.0 \times 10^{-21}$ J; $\zeta = -55$ mV; $\lambda = 100$ nm; $\lambda = 3.55$ μ m; $L = 15$ nm (diamonds) and $L = 30$ nm (squares). $\kappa a = 2332$, $\text{pH} = 8.5$.

Figure 3.15a: Scattering Diagram for Bitumen in 0.025M NaCl + 0.015M NaHCO₃ - Steric Repulsion Model



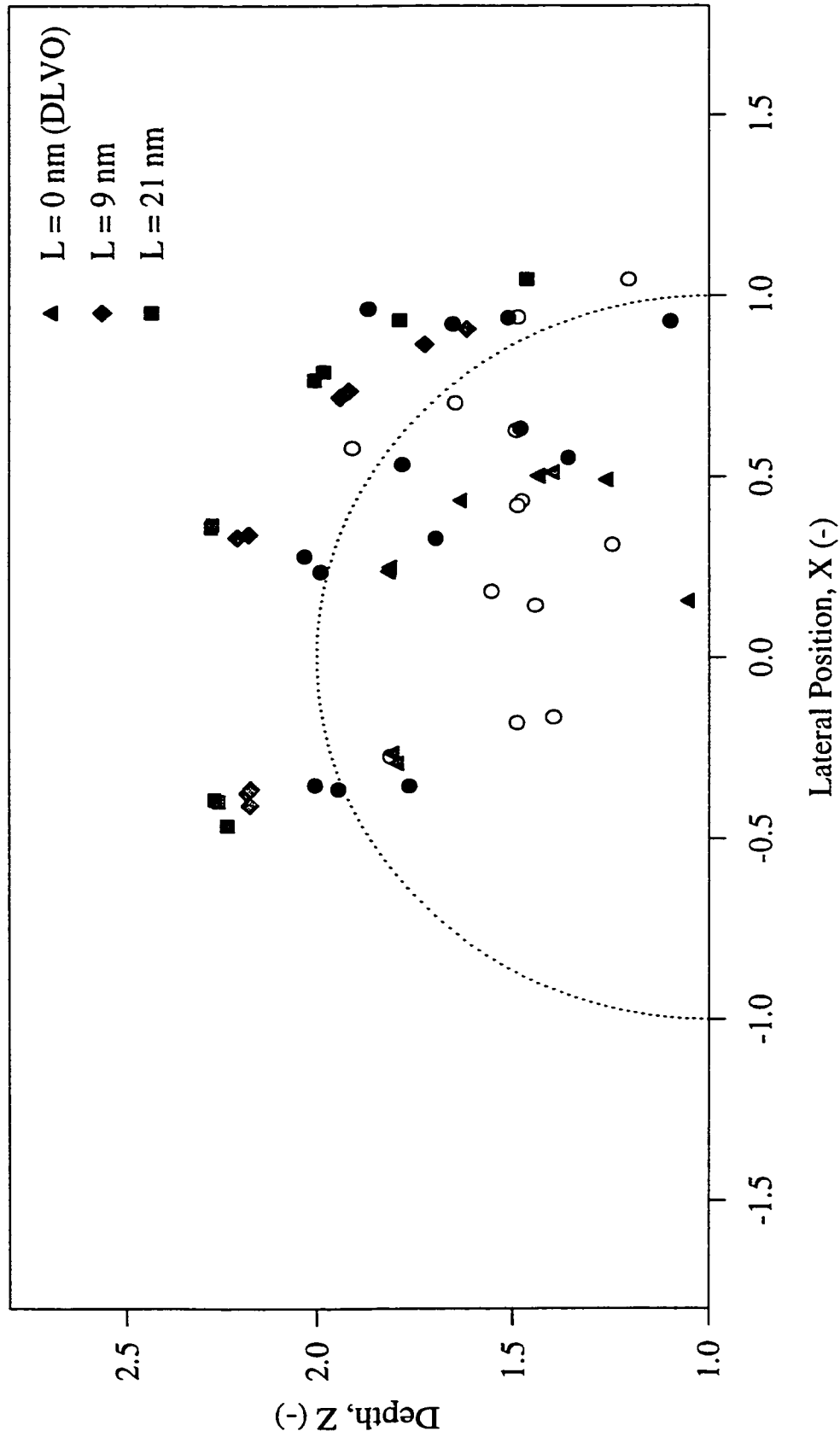
The white and black circles are respectively the experimental initial and final positions of the mobile droplet. The gray symbols are the theoretical final positions calculated using the DLVO theory (triangles) and the steric repulsion model (diamonds and squares). Parameters used: $A = 3.0 \times 10^{-21}$ J; $\zeta = -55$ mV; $\lambda = 100$ nm; $a = 2.52$ μ m; $L = 13$ nm (diamonds) and $L = 22$ nm (squares). $\kappa a = 1656$, pH = 8.5.

Figure 3.15b: Scattering Diagram for Bitumen in 0.025M NaCl + 0.015M NaHCO₃ - Steric Repulsion Model



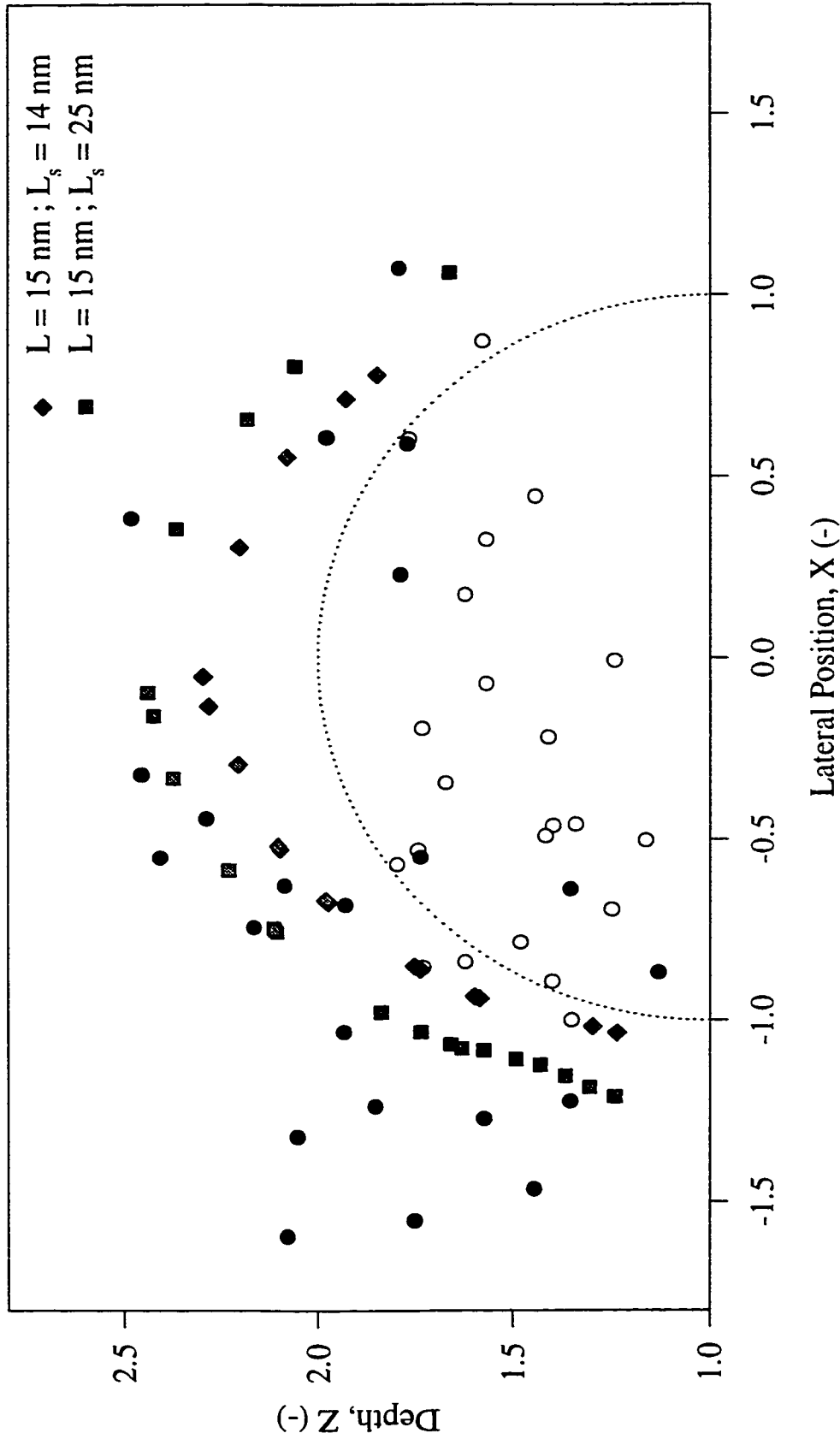
The white and black circles are respectively the experimental initial and final positions of the mobile droplet. The gray symbols are the theoretical final positions calculated using the DLVO theory (triangles) and the steric repulsion model (diamonds and squares). Parameters used: $A = 3.0 \times 10^{-21}$ J; $\zeta = -55$ mV; $\lambda = 100$ nm; $a = 2.81$ μ m; $L = 12$ nm (diamonds) and $L = 22$ nm (squares). $\kappa a = 1846$. $\text{pH} = 8.5$.

Figure 3.15c: Scattering Diagram for Bitumen in 0.025M NaCl + 0.015M NaHCO₃ - Steric Repulsion Model



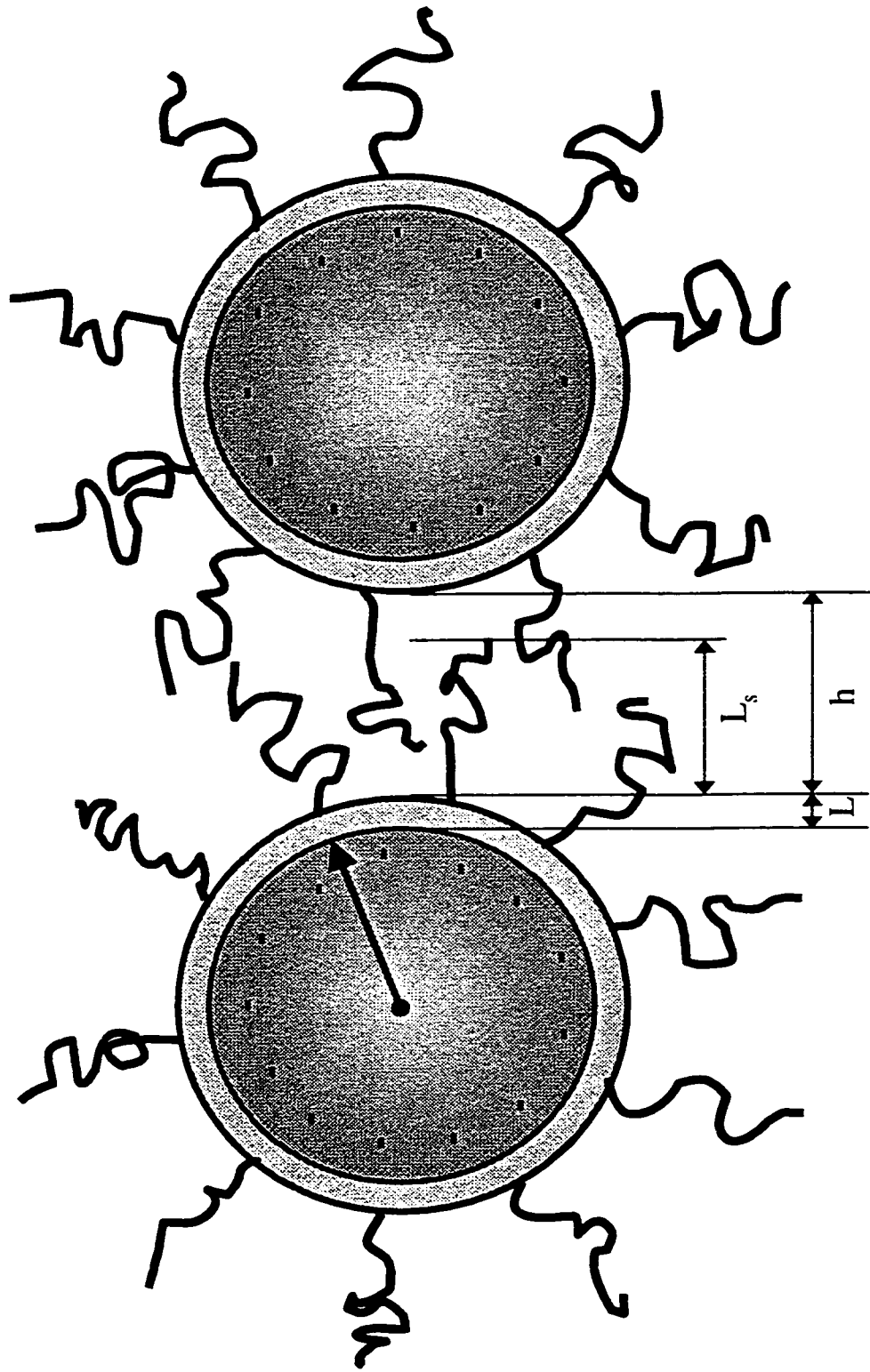
The white and black circles are respectively the experimental initial and final positions of the mobile droplet. The gray symbols are the theoretical final positions calculated using the DLVO theory and the steric repulsion model (diamonds and squares). Parameters used: $A = 3.0 \times 10^{-21}$ J; $\zeta = -55$ mV; $\lambda = 100$ nm; $a = 3.55$ μ m; $L = 9$ nm (diamonds) and $L = 21$ nm (squares). $\kappa a = 2332$, $\text{pH} = 8.5$

Figure 3.16: Scattering Diagram for Bitumen with Clay in 0.025M NaCl + 0.015M NaHCO₃ - Shell and Core Steric Model



The white and black circles are respectively the experimental initial and final positions of the mobile droplet. The gray symbols are the theoretical final positions calculated using the shell and core model (diamonds and squares). Parameters used: $A_{h,w,b} = 3.0 \times 10^{-21} \text{ J}$; $A_{e,w,c} = 3.8 \times 10^{-20} \text{ J}$; $\zeta = -47 \text{ mV}$; $\lambda = 100 \text{ nm}$; $a = 2.39 \mu\text{m}$; Clay layer = 15 nm; $L_s = 14 \text{ nm}$ (diamonds) and $L_s = 25 \text{ nm}$ (squares). $k_a = 1570$, $\text{pH} = 8.5$.

Figure 3.17: Shell and Core Model



CHAPTER 4

MEASUREMENT OF THE MAXIMUM ATTRACTIVE FORCE USING HYDRODYNAMIC FORCE BALANCE

Most of the samples studied in the previous chapter using colloidal particle scattering were also investigated using the hydrodynamic force balance (HFB) technique described in Chapter 2.

The hydrodynamic force balance technique is used to complement the colloidal particle scattering study by measuring the maximum attractive force. This maximum attractive force, located close to the secondary energy minimum, (cf. Figures 1.4 and 2.6) provides meaningful information for stability studies. An important advantage of the HFB technique is that the force measured depends only on the hydrodynamics and not on any colloidal force models.

A colloidal force model with adjustable parameters may nevertheless be applied to interpret the determined colloidal forces in an effort to gain useful information about one parameter of the assumed model, for example a parameter describing the bitumen surface structure.

In this study, the single disk model was applied to all samples for simplicity. The disk model has been found to be sufficient to qualitatively compare surface roughness of various samples. The surface characterisation using the hydrodynamic force balance should be treated as a preliminary study.

The colloidal force as described by the single disk model is function of the several parameters (cf. Equations 3.2 and 3.3):

$$F_{\text{colloidal}} = f(a, h, L, r, \kappa, e, \psi_0 k, T, \epsilon, \epsilon_0 z, A_{s-s}, A_{d-s}, A_{d-d}) \quad (4.1)$$

where the various parameters are defined in Chapter 3.

The procedure used to determine one of the parameters, e.g. L , of a force model consists of fixing all the parameters mentioned in Equation 4.1, with the exception of h and the parameter to determine. Since only one equation (the single disk model colloidal force equation) and one constraint (h must correspond to the secondary minimum separation distance) are available, the number of additional parameters that can be determined with the HFB technique is limited to one only. Once the independent parameters are fixed, an initial arbitrary value is chosen for the parameter to determine. The colloidal force is then calculated based on the colloidal force model for a small separation distance, h . The separation distance is then incremented and the new colloidal force corresponding to the new separation distance is calculated. The iterative procedure continues until the new force calculated becomes higher than the previously calculated force value. The previously calculated values for the colloidal force and the separation distance correspond, respectively, to the maximum attractive force and to the separation distance at the secondary force minimum. The parameter to determine is then modified and the calculations yielding the maximum attractive force are repeated for this new parameter value. The procedure is repeated until the maximum attractive force calculated from the colloidal force model corresponds to the experimentally determined hydrodynamic drag force. The computer programs used to perform the calculations were provided courtesy of Dr. Alex Wu from Syncrude Canada Ltd.

Among the bitumen samples mentioned in Chapter 3, the case of asphaltenes-treated clays was not studied. The reason is that the hydrodynamic force balance method requires attraction between the droplets. As it was noted from the respective scattering diagrams (cf. Figures 3.4, 3.9 and 3.13) all samples showed a pronounced repulsion at an electrolyte concentration of 0.04M. Thus, the electrolyte

concentration had to be increased to 0.1M for both bitumen and deasphalted bitumen in order to have sufficient attraction to perform the experiments. For clay-containing bitumen emulsions, a higher electrolyte concentration results in instant formation of large clay aggregates, which hinders any precise measurements of a hydrodynamic force balance.

4.1. Effect of Asphaltenes

It was found in the previous chapter that asphaltenes contributed to the stability of a bitumen emulsion by enhancing the repulsion between the droplets. This result was obtained with a hydrodynamic driving force of approximately 1 pN in collision experiments (CPS). To investigate if the enhanced repulsion due to asphaltenes can also be detected around the secondary minimum, the maximum attractive force was measured for both bitumen and deasphalted bitumen samples in the presence of 0.1M of potassium chloride.

The results obtained for deasphalted bitumen are given in Table 4.1. The first column provides the radius of the droplets used in each experimental run, directly measured from droplet images with a size calibration for diffraction. Occasionally, a pair of droplets could be reused for more than one doublet break-up. Thus, identical radii in column 1 of Table 4.1 usually indicate such a case. The second column of Table 4.1 gives the measured maximum attractive force, obtained from the experimental data and the hydrodynamic calculations following the procedure in Chapter 2. As it can be observed, the forces obtained vary considerably, ranging from 0.35 to 3.04 pN. This variability is an indication that the droplets do not always present the same surface region to each other. In fact, the free droplet rotates on both the approaching and the receding part of the doublet break-up experimental run. The free bitumen droplet also rises slowly to the surface due to the slight buoyancy force induced by the slightly higher density of the solution. Although the buoyancy effect is negligible during an

experimental run, it becomes important over a time period of minutes, contributing to the change in the relative position of the droplets.

All the doublets created in the HFB experiments were secondary doublets. This was clearly indicated by the low shear rate needed to separate the doublets and by the rotation of the free droplet under the shear and before the doublet separation.

As it can be seen from Equations 3.2 and 3.3, the colloidal force is proportional to the radius of the droplets. Therefore, it is best to compare the ratio of the force to the radius to avoid any misinterpretation due to the size effect. The F/a values vary from $0.11 \mu\text{N/m}$ to $1.04 \mu\text{N/m}$, with an average value of $0.37 \mu\text{N/m}$. Most values are again quite small, indicating shallow secondary force minima. However, in two instances the forces are quite high compared to the others. It is strongly believed that these two break-up situations correspond to smooth sphere-sphere interaction. The classical DLVO theory was applied to those results and the Hamaker constant was found using the procedure described in the introduction of the present chapter. A Hamaker constant value of $2.6 \times 10^{-21} \text{ J}$ was found. This Hamaker constant value is in very good agreement with the value obtained from colloidal particle scattering, which is $2.7 \times 10^{-21} \text{ J}$.

Once the Hamaker constant has been determined, it is possible to characterise the surface roughness, using a force model such as the single disk model. The radius of the disk was estimated from the SEM image shown in Figure 3.2. Its thickness was calculated from the single disk model by fitting the experimentally determined force. Lacking the detailed information about the protrusion composition, only two extreme cases of protrusions made of 100% water and protrusions made of 100% bitumen were considered. The thickness values calculated are listed in columns 4 and 5 of Table 4.1 respectively. Note that the thickness values correspond to the total thickness of both disks. It is impossible to determine the exact thickness of the individual disks with the single disk model. For example, the disks may have the

thickness of $\frac{1}{2} L$ each or one may have a thickness of $\frac{1}{4} L$ and the other a thickness of $\frac{3}{4} L$. It is also possible to have only one disk of thickness L .

From columns 4 and 5 of Table 4.1, it is clear that the total thickness values calculated for protrusions made of 100% water are thinner than those obtained for protrusions made of 100% bitumen. The average values of the thickness are 7.5 nm for water protrusions and 12.5 nm for bitumen protrusions.

The hydrodynamic force balance technique was also applied to an untreated bitumen sample, with the same electrolyte and the same electrolyte concentration. The results obtained are given in Table 4.2. As it can be seen from the table, the force measured varies substantially, even for a same pair of droplets. Again, the absolute force measured was divided by the radius to obtain a more reliable comparative value. These F/a values range from 0.1 $\mu\text{N/m}$ to 1.12 $\mu\text{N/m}$, a range similar to that of deasphalted bitumen. The averaged F/a values are also comparable to those obtained for deasphalted bitumen droplets although the value for untreated bitumen is slightly lower than that of deasphalted bitumen.

The surface of bitumen was also characterised by the disk model. In this case, however, it is not possible to determine the Hamaker constant from the interactions between the smooth parts of the droplets due to the absence of any smooth regions on bitumen surface (cf. SEM image in Figure 3.8). The Hamaker constant was assumed to be identical to the value determined by the colloidal particle scattering technique, 3.0×10^{-21} J. Calculations were made for both the 100% water and 100% bitumen cases. As it can be seen from Table 4.2, the thicknesses obtained are larger than those calculated for deasphalted bitumen. When the disk is assumed to be made of 100% water, the average value obtained for bitumen is 9.8 nm compared to 7.5 nm for deasphalted bitumen. When the disk protrusions are assumed to be made of 100% bitumen, the disk model can only fit 6 experimental force measurements. The failure of fitting may indicate that the disk model is not valid for the bitumen surface. An

additional repulsive force, such as a steric force, is present to make the attractive force around the secondary minimum smaller than any predictions from the disk model, no matter how the thickness parameter is adjusted. As a conclusion, the results from the HFB experiment strongly indicate two possible structures on the untreated bitumen surface: loose and “watery” protrusions composed of hairy chains (100% water in protrusions) or solid protrusions (100% bitumen in protrusions) also covered by hairy polymeric chains to provide additional repulsive force. Any intermediate structures or the combination of both might also be present. Essentially, the existence of loose hairy structures detected here is consistent with the finding using the colloidal particles scattering technique (see Chapter 2).

4.2. Effect of Electrolyte and pH

The hydrodynamic force balance technique was also used to study the effect of a different electrolyte along with a different pH. The electrolyte concentration was kept identical to that used for the bitumen and deasphalted bitumen emulsions presented in section 4.1, namely 0.1M. However, a solution containing a combination of NaCl and NaHCO₃ was used instead of the KCl solution. The 5:3 ratio of sodium chloride to sodium bicarbonate used in the colloidal particle scattering experiments (cf. section 3.2) was kept. The respective concentrations of NaCl and NaHCO₃ yielded a pH of about 8.5, which is similar to the pH used for colloidal particle scattering experiments. Results obtained for this bitumen in NaCl and NaHCO₃ are given in Table 4.3. As it can be noted from Table 4.3, more doublet break-ups were recorded with the same pair of bitumen droplets. The reason is that the electrostatic repulsion between the glass surface and the bitumen droplets was enhanced for the NaCl and NaHCO₃ solution at a pH of 8.5.

Once again, according to columns 2 and 3 of Table 4.3, the force values vary considerably. The actual force measured ranges from 0.23 pN to 2.91 pN, with an

average value of 1.09 pN. This average value is higher than the average force measured for bitumen in 0.1M KCl, which was 0.81 pN. When comparing the F/a values, the difference is not as significant although bitumen in NaCl and NaHCO₃ again shows a more attractive force than bitumen in KCl, with respective average values of 0.40 $\mu\text{N}/\text{m}$ and 0.35 $\mu\text{N}/\text{m}$. These hydrodynamic force balance results agree with the results obtained from the colloidal particle scattering technique. This finding seems to contradict the common belief that at higher pH, the higher surface potential enhance the repulsive force between bitumen droplets and thus make them more stable in water. The higher surface potential in a NaCl/NaHCO₃ solution was observed through zeta potential measurement. The zeta potential of bitumen drops in a 0.04M NaCl/NaHCO₃ solution (pH = 8.5) is -55 mV as compared to -30 mV for the bitumen drops in a 0.04M KCl solution (pH = 7). Note that the zeta potentials used to obtain the disk thicknesses were measured at an electrolyte concentration of 0.04M instead of the 0.1M concentration used to perform the experiments. At the high concentration of 0.1M, the micro-electrophoresis apparatus used to measure the zeta potentials was unable to provide reliable measurements. Since the zeta potentials were only needed to obtain the protrusion thickness of the somewhat disputable single disk model, the values determined at an electrolyte concentration of 0.04M were used.

As mentioned above, the presence of a layer of polymeric chains on the bitumen surface is quite likely. If these chains are negatively charged, the higher surface potential at a high pH will force them to extend more into the water phase, therefore further enhance the repulsive force. The opposite trend observed in the experiment can be explained by the fact that some natural surfactants on the oil-water interface disperse into the water phase after ionisation at a higher pH [7], leaving behind a relatively smooth bitumen surface. As shown above, the interaction force between smooth surfaces is less repulsive, around the secondary minimum. The existence of liberated natural surfactants is supported by some literature findings [8] as well as the SEM analysis in the present study. The SEM image (cf. Figure 3.8) shows that some protrusions seem to deposit on the bitumen surface in the sample preparation for SEM

scanning rather than being an inherent part of it. It has also been observed that there is a transition from rough solid film to smooth liquid film on the crude oil-water interface when the pH rises above a certain value between 6-10, depending on oil compositions and salt concentrations [63]. It is quite likely that the film property changes at the pH that enables sufficient ionisation and dispersion of natural surfactants.

Bitumen surface characterisation was attempted in the NaCl/NaHCO₃ system using the single disk model. As was the case for the bitumen droplets in presence of KCl, a Hamaker constant of 3.0×10^{-21} J was assumed. Thickness values ranging from 1.1 to 18 nm were found when the disks were assumed to be made of 100% water. This range of thickness agrees well with the one calculated for bitumen in a KCl solution. The average thickness for bitumen in a NaCl/NaHCO₃ solution is smaller than that in a KCl solution. As mentioned above, it could be the result of surfactant migration from the bitumen surface. Calculations were also performed for the case where the disks are assumed to be made of 100% bitumen. However, as was the case for bitumen in presence of KCl, the model cannot fit all the force measurements. In fact, the model barely fits more than half of the results. Following the same argumentation as in section 4.1, the incapability of fitting the experimental data indicates the existence of hairy structures on bitumen surface.

4.3. Discussion and Conclusions

Table 4.4 summarises the ranges and the average values (in brackets) of the determined forces and the proposed protrusion thickness in various bitumen systems. It can be observed that the average secondary force minimum for deasphalted bitumen is comparable to the secondary force minimum for bitumen. The slightly higher value for deasphalted bitumen is in accordance with the colloidal particle scattering results. Comparing the force values for bitumen in presence of KCl and bitumen in presence

of NaCl/NaHCO₃ show that the latter has a slightly greater maximum attractive force. In other words, the NaCl/NaHCO₃ solution at a pH of 8.5 lowers the repulsion between the bitumen droplets. The difference is tentatively attributed to the effect of pH on the solubility of the naturally surfactants in water, causing the dissociation of the surfactants from the bitumen-water interface and a structural change of the interfacial film. Such a phenomenon was previously observed in crude oil-water emulsions [7, 63].

As it was the case with colloidal particle scattering, a colloidal force model was applied to the results in an attempt to characterise the surface of the bitumen droplets. For simplicity considerations, the single disk model was used. The total disk thickness is given in Table 4.4 for protrusions made of 100% water. The thickness results of Table 4.4 seem to indicate that deasphalted bitumen is smoother than bitumen, which agrees with the result obtained from colloidal particle scattering as well as from the SEM images. When the single disk model was applied to the two bitumen samples, it yielded a higher disk thickness for bitumen in presence of KCl than for bitumen in presence of a NaCl/NaHCO₃. This difference in thickness seems to support the hypothesis that pH affects the migration of the natural surfactants on the oil-water interface.

As already discussed, the thickness values calculated from the single disk model should be regarded as being qualitative only due to the uncertainty in the correct representation of the bitumen surface by the disk model used. In fact, for protrusions made of pure bitumen, the single disk model cannot predict a force as repulsive as measured in many cases. The failure of the data fitting proves that either the single disk model is inadequate for a good representation of bitumen surface roughness and that there might be an additional hairy layer to provide more repulsion, or that the protrusions are made of more loose structures containing more water. In either case, the data strongly indicate the existence of hairy structures on the bitumen surface.

The single disk model may not be an ideal model for bitumen surfaces. More sophisticated models, such as the spherical cap model, predict a higher attractive force at the secondary minimum. This requires more “watery” protrusions or more hairy structures to explain the experimental data, which does not contradict the above-mentioned conclusions.

To summarise, the experimental results do not allow any definite conclusion on the effect of asphaltenes on the depth of the secondary minimum. Experimental results show that using a solution of NaCl and NaHCO₃ (pH = 8.5) instead of a solution of KCl (pH = 7) results in a lower repulsion around the secondary minimum, which agrees with the previous findings from colloidal particle scattering.

Table 4.1: Maximum Attractive Force for Deasphalted Bitumen in a 0.1M KCl Solution

Radius, a (μm)	$F_{\text{colloidal}}$ (pN)	$F_{\text{colloidal}}/a$ ($\mu\text{N}/\text{m}$)	Disk Thickness, L (nm)	
			100% water	100% bitumen
2.92	3.04	1.04	0	0
2.28	2.35	1.03	0	0
2.88	2.23	0.78	1.6	2.0
2.23	1.68	0.75	1.5	1.9
3.48	2.51	0.72	2.1	2.5
2.84	1.85	0.65	2.4	3.0
2.84	1.84	0.65	2.4	3.0
2.28	1.39	0.61	2.5	3.3
2.66	1.00	0.38	5.4	7.1
2.62	0.98	0.38	5.4	7.2
3.14	1.11	0.35	6.0	7.6
2.43	0.80	0.33	6.2	8.5
2.09	0.59	0.28	7.0	10.3
2.28	0.60	0.26	7.5	11.0
2.90	0.73	0.25	8.1	11.0
2.90	0.71	0.24	8.2	11.3
2.66	0.65	0.24	8.1	11.4
2.56	0.61	0.24	8.3	11.9
2.23	0.53	0.24	8.2	12.3
2.09	0.38	0.18	10.1	17.5
2.66	0.45	0.17	10.8	16.7
2.35	0.39	0.17	10.8	17.8
2.07	0.35	0.17	10.7	19.2
2.84	0.46	0.16	11.2	17.1
2.09	0.31	0.15	11.5	21.9
2.09	0.28	0.13	12.5	25.7
2.09	0.27	0.13	12.8	27.2
1.89	0.22	0.12	13.5	37.4
3.04	0.34	0.11	14.5	24.6
3.14	0.35	0.11	14.5	25.3
Average	0.97	0.37	7.5	12.5
			$A_{s-s}=2.6 \times 10^{-21} \text{ J}$	$A_{s-s}=2.6 \times 10^{-21} \text{ J}$
			$A_{d-d}=0$	$A_{d-d}=2.6 \times 10^{-21} \text{ J}$
			$A_{d-s}=0$	$A_{d-s}=2.6 \times 10^{-21} \text{ J}$
			$\zeta=-80 \text{ mV}$	$\zeta=-80 \text{ mV}$

Table 4.2: Maximum Attractive Force for Untreated Bitumen in a 0.1M KCl Solution

Radius, a (μm)	$F_{\text{colloidal}}$ (pN)	$F_{\text{colloidal}}/a$ ($\mu\text{N}/\text{m}$)	Disk Thickness, L (nm)	
			100% water	100% bitumen*
2.23	2.49	1.12	1.6	3.7
2.44	2.31	0.95	2.5	5.4
2.45	2.13	0.87	2.6	6.7
2.12	1.36	0.64	3.8	16.0
2.35	1.44	0.61	4.1	14.8
2.66	1.47	0.55	4.8	15.5
2.14	1.02	0.48	5.5	--
2.14	1.02	0.48	5.5	--
2.30	1.03	0.45	6.0	--
2.44	1.00	0.41	6.5	--
2.30	0.92	0.40	6.6	--
1.99	0.75	0.38	6.8	--
2.14	0.72	0.34	7.6	--
2.14	0.52	0.24	9.8	--
2.23	0.53	0.24	10.0	--
2.66	0.63	0.24	10.2	--
2.14	0.44	0.21	11.0	--
3.27	0.56	0.17	12.9	--
2.14	0.36	0.17	12.7	--
1.99	0.33	0.16	12.8	--
2.14	0.34	0.16	13.2	--
2.27	0.34	0.15	13.7	--
2.06	0.31	0.15	13.6	--
2.14	0.30	0.14	14.4	--
3.27	0.36	0.11	17.0	--
2.25	0.25	0.11	16.6	--
2.14	0.23	0.11	16.9	--
2.06	0.21	0.10	17.2	--
2.14	0.21	0.10	17.7	--
Average	0.81	0.35	9.8	--

$A_{s-s}=3.0 \times 10^{-21} \text{ J}$ $A_{s-s}=3.0 \times 10^{-21} \text{ J}$
 $A_{d-d}=0$ $A_{d-d}=3.0 \times 10^{-21} \text{ J}$
 $A_{d-s}=0$ $A_{d-s}=3.0 \times 10^{-21} \text{ J}$
 $\zeta=-30 \text{ mV}$ $\zeta=-30 \text{ mV}$

* "--" indicates that the observed force cannot be fitted with this set of parameters.

Table 4.3: Maximum Attractive Force for Untreated Bitumen in a 0.1M (NaCl + NaHCO₃) Solution

Radius, a (μm)	$F_{\text{colloidal}}$ (pN)	$F_{\text{colloidal}}/a$ ($\mu\text{N}/\text{m}$)	Disk Thickness, L (nm)	
			100% water	100% bitumen*
2.71	2.72	1.01	1.1	1.9
2.71	2.70	1.00	1.1	1.9
2.98	2.91	0.98	1.3	2.1
2.98	2.49	0.84	1.9	3.2
2.98	2.42	0.81	2.0	3.5
2.99	2.41	0.81	2.0	3.5
2.99	2.37	0.79	2.1	3.7
2.98	2.22	0.75	2.4	4.2
2.98	2.21	0.74	2.4	4.2
2.98	2.19	0.74	2.4	4.3
2.99	2.15	0.72	2.5	4.7
2.98	2.14	0.72	2.5	4.7
2.99	2.12	0.71	2.6	4.9
2.98	1.93	0.65	3.0	5.9
2.99	1.91	0.64	3.1	6.0
2.98	1.80	0.60	3.4	6.6
2.71	1.63	0.60	3.3	7.0
2.98	1.78	0.60	3.4	6.8
2.98	1.77	0.59	3.4	6.9
2.98	1.57	0.53	4.3	8.4
2.99	1.54	0.52	4.4	8.6
2.99	1.50	0.50	4.6	9.1
2.28	1.14	0.50	4.3	11.2
2.99	1.46	0.49	4.7	9.5
2.09	1.01	0.48	4.4	13.3
2.28	1.08	0.48	4.6	12.4
2.99	1.40	0.47	4.9	10.1
2.28	1.05	0.46	4.8	13.3
2.28	1.04	0.46	4.8	13.5
2.09	0.93	0.45	4.8	16.2
2.99	1.31	0.44	5.3	11.3
2.40	1.03	0.43	5.2	14.6
2.09	0.88	0.42	5.2	18.7
2.28	0.96	0.42	5.3	16.3
2.98	1.23	0.41	5.6	12.5
2.32	0.90	0.39	5.8	19.4

Radius, a (μm)	$F_{\text{colloidal}}$ (pN)	$F_{\text{colloidal}}/a$ ($\mu\text{N}/\text{m}$)	Disk Thickness, L (nm)	
			100% water	100% bitumen*
2.98	0.85	0.29	7.9	26.0
2.99	0.73	0.24	9.0	--
2.99	0.71	0.24	9.2	--
2.99	0.68	0.23	9.5	--
2.99	0.68	0.23	9.6	--
2.98	0.67	0.23	9.6	--
2.98	0.61	0.20	10.4	--
2.41	0.48	0.20	10.4	--
2.99	0.54	0.18	11.3	--
2.40	0.41	0.17	11.5	--
2.98	0.51	0.17	11.7	--
2.98	0.51	0.17	11.8	--
2.09	0.35	0.17	11.7	--
2.09	0.35	0.17	11.7	--
2.98	0.49	0.17	12.1	--
2.10	0.34	0.16	11.8	--
2.98	0.48	0.16	12.3	--
2.71	0.41	0.15	12.8	--
2.99	0.44	0.15	13.0	--
2.09	0.31	0.15	12.7	--
2.10	0.31	0.15	12.8	--
2.40	0.34	0.14	13.1	--
2.98	0.41	0.14	13.6	--
2.09	0.27	0.13	13.7	--
2.10	0.27	0.13	13.9	--
2.41	0.31	0.13	14.1	--
2.40	0.30	0.13	14.3	--
2.09	0.26	0.12	14.4	--
2.22	0.26	0.12	14.8	--
2.25	0.26	0.12	15.1	--
2.98	0.32	0.11	16.0	--
2.25	0.24	0.11	15.8	--
2.25	0.23	0.10	16.4	--
2.99	0.26	0.09	18.0	--
Average	1.09	0.40	7.9	--

$A_{s-s}=3.0 \times 10^{-21} \text{ J}$ $A_{s-s}=3.0 \times 10^{-21} \text{ J}$
 $A_{d-d}=0$ $A_{d-d}=3.0 \times 10^{-21} \text{ J}$
 $A_{d-s}=0$ $A_{d-s}=3.0 \times 10^{-21} \text{ J}$
 $\zeta=-55 \text{ mV}$ $\zeta=-55 \text{ mV}$

* "--" indicates that the observed force cannot be fitted with this set of parameters.

Table 4.4: Summary of Maximum Attractive Force Measurements

	$F_{\text{colloidal}}$ (pN)	$F_{\text{colloidal}}/\text{Radius}$ ($\mu\text{N/m}$)	Zeta Potential ¹ (mV)	Disk Thickness ² (nm)
Bitumen in 0.1M KCl	0.21 to 2.49 (0.81) ³	0.10 to 1.12 (0.35)	-30	1.6 to 17.7 (9.8)
Bitumen in 0.1M (NaCl + NaHCO₃)	0.26 to 2.72 (1.09)	0.09 to 1.01 (0.40)	-55	1.1 to 18.0 (7.9)
Deasphalted Bitumen in 0.1M KCl	0.35 to 3.04 (0.97)	0.11 to 1.04 (0.37)	-80	0 to 14.5 (7.5)

¹ The micro-electrophoresis apparatus did not provide reliable measurements of the zeta potentials at such a high electrolyte concentration (0.1M). Since the zeta potentials were only needed for the calculation of the disk thickness (single disk model), the values measured at 0.04M KCl were used for the approximate determination of the magnitude of surface roughness performed here.

² Disk thicknesses reported for disks assumed to be made of 100% water.

³ Values in brackets are the average values.

CHAPTER 5

CONCLUSIONS

5.1. Review of Problem and Objectives

The modern economy strongly depends on energy sources. Among these sources, petroleum plays a prominent role. However, as the conventional crude oil resources are depleting, other sources of energy will need to be used. Oil sands are one of these sources. Alberta possesses the world's largest oil sands deposit, the Athabasca deposit, which can provide enough energy to every Canadian for at least a century.

An important problem of bitumen extraction from oil sands is the formation of a very stable bitumen-in-water emulsion during the digestion of the oil sands lumps, resulting in a loss of bitumen in the tailing stream. The amount of bitumen lost depends on the quality of the oil sands ore and especially on the amount of fines contained in the ore. The poorer the quality of the ore is, the smaller and the more stable the bitumen droplets will be and as a consequence, the greater the bitumen losses will be.

The bitumen droplets in the stable emulsion are of colloidal size and thus, the surface characteristics of these droplets play a very important role in the way they interact with each other. Many factors can affect or modify the surface characteristics of bitumen droplets. Three of these factors were considered in the present study. First, the effect of asphaltenes was investigated. Asphaltenes, one of the main components of bitumen, form stable nano-size aggregates at the bitumen and water interface. Once these asphaltenes aggregates migrate to the bitumen-water interface, they are likely to influence the bitumen droplet-droplet interactions. The effect of asphaltenes

was determined by comparing the interaction force between emulsified droplets made of deasphalted bitumen and droplets made of untreated bitumen.

The operating conditions used in the extraction process are another factor that can influence the size of the bitumen droplets and their interactions. Two bitumen emulsions were prepared and studied using different electrolytes and pH of solution. Finally, since fines contribute to the stabilisation of bitumen emulsions, the effect of adding clay to the emulsion was also investigated. As kaolinite clay forms the major part of the fines found in oil sands, this type of clay was used in the experiment.

5.2. Summary of Experimental Results

The stability of bitumen droplets in water was investigated by measuring the interaction force between individual droplets using the colloidal particle scattering (CPS) and the hydrodynamic force balance (HFB) techniques, which were described in Chapter 2. The colloidal particle scattering technique is capable of determining the complete force profile by fitting the experimental results with a colloidal force model containing adjustable parameters. The hydrodynamic force balance technique enables one to measure the maximum attractive force, around the secondary minimum, through hydrodynamic calculations. Both the HFB and the CPS methods are more sensitive than most commonly used colloidal force measurement techniques and are able to measure forces as small as those encountered at the secondary minimum, typically 0.1 pN to 10 pN.

Although CPS and HFB were used to measure the force at different regimes of the force profile, both yielded the same conclusions. One of these conclusions is that

asphaltenes greatly contribute to the stability⁷ of bitumen-in-water emulsions. This increased stability was confirmed by the scattering diagrams showing a much lower repulsion for deasphalted bitumen droplets than for untreated bitumen droplets.

The effect of electrolyte and pH was also investigated. The experimental results obtained from the colloidal particle scattering technique indicate that bitumen droplets in a KCl solution at a pH of 7 repel each other more strongly than bitumen droplets in a NaCl/NaHCO₃ solution at a pH of 8.5. The same tendency is found in the results of the hydrodynamic force balance experiment. As shown in Table 4.4, the magnitude of the maximum attractive force is slightly higher (0.40 μN/m vs. 0.35 μN/m) for the bitumen emulsion at a pH of 8.5. The increase in attraction (HFB) or decrease in repulsion (CPS) observed for bitumen droplets in the NaCl/NaHCO₃ solution at a pH of 8.5 is tentatively attributed to the migration of natural surfactants from the interface to the water phase.

5.3. Force Modelling

The above mentioned summary was arrived at directly from the experimental results, without applying any colloidal force model. It is possible to gain further knowledge, especially quantitative data, through the use of an appropriate colloidal force model. As discussed in Chapters 3 and 4, the experimental results can be used to determine one or several adjustable parameters for a given force model. For example, using the DLVO theory as the colloidal force model, the Hamaker constant of deasphalted bitumen was determined to be in the range of around 2.6×10^{-21} J to 2.7×10^{-21} J.

⁷ Stability here refers to the non-aggregation/non-coalescence of the bitumen droplets. Greater stability means less opportunity for aggregation or coalescence due to either a higher repulsive force (CPS) or a lower maximum attractive force (HFB).

Once all the parameters of the force model are determined, the complete force profile can be plotted. In the case of an HFB experiment, only one point in the force profile is obtained and is located at the secondary force minimum.

Calculations based on the DLVO theory for the colloidal particle scattering data clearly indicate that the DLVO theory cannot represent the true interaction forces for all bitumen samples. Furthermore, the DLVO theory is erroneous in its qualitative predictions as well. For example, the DLVO theory predicts aggregation at the secondary minimum for the bitumen sample in a 0.04M KCl solution and for the clay-containing emulsion, in contradiction with the experimental results. Since surface roughness is known to enhance the repulsion between colloidal particles and droplets, calculations were made using force models that considered roughness. First, a simple roughness model, called the single disk model, was applied to all results in an attempt to semi-quantitatively characterise the degree of surface roughness. The theoretical final positions obtained with this disk model are more representatives of the experimental final positions, especially for deasphalted bitumen and for bitumen in a NaCl/NaHCO₃ solution at pH 8.5. However, the final positions predicted by the single disk model are still not indicative of the magnitude of the repulsion observed. The difference in the repulsion predicted by the disk model and the repulsion actually observed is particularly significant for the bitumen in the 0.04M KCl solution.

The disk model was also applied to the results obtained with the hydrodynamic force balance technique. Two cases were studied: protrusions made of 100% water and protrusions made of 100% bitumen. Calculations made for the first case indicated that deasphalted bitumen is smoother than bitumen. They also indicated a smaller disk thickness for the bitumen in the solution at a pH of 8.5. When the disks were assumed to be made of pure bitumen, the disk model was not able to fit all the experimental data. Therefore, the pure bitumen disks model provided a less quantitative representation of either the composition or the geometry of the protrusions.

The surface of the bitumen droplets was scanned under a scanning electron microscope for both untreated bitumen and deasphalted bitumen. The images show that deasphalted bitumen is much smoother than bitumen. In addition, the SEM images indicate that the geometry of the protrusions resembles spherical caps. A new model, the multiple spherical cap model, was developed to represent the observed geometry. The force profiles shown in Figure 3.10 for this new model indicate that spherical cap protrusions produce a much weaker repulsion than the disk-shaped protrusions for protrusions assumed to be made of 100% water. Although not shown in Figure 3.10, the same conclusion is reached when the protrusions are assumed to be made of 100% bitumen. Since the more realistic spherical cap model is incapable of predicting the strong repulsion observed, it is strongly believed that an additional repulsive force in the form of steric repulsion plays an important role in the interaction between the bitumen droplets.

The additional repulsive force could be caused by the polymeric chains on the surface of the bitumen droplets, which could trigger two possible mechanisms of repulsion: steric repulsion and enhanced electrostatic repulsion. The main differences between the two mechanisms are that for a steric interaction the repulsion is due to the interpenetrating and compression of the chains whereas for an enhanced electrostatic interaction the repulsion is caused by the shift in the charge plane. Both types of interaction provided a better fit than either the single disk or the DLVO force models. Based on the large tangential deviation observed in the experiment, a steric repulsion seems more likely for untreated bitumen. However, the experimental positions of the deasphalted bitumen droplets show very little tangential deviation, which indicates the absence of steric interaction.

As it can be seen, several colloidal force models were presented in an attempt to gain a better understanding of the interaction between bitumen droplets. Although these

models were not able to provide unambiguous conclusions, they helped in understanding how bitumen droplets interact in an emulsion.

Finally, the effect of adding asphaltene-treated clay was investigated using the CPS method. Clay flocculation problems prohibited the use of the HFB technique. Based on the core and shell model, it has been found that an additional steric layer (hairy structure) outside the clay shell is required to explain the large repulsive forces observed in the experiments. This has the implication that what makes the clay-coated bitumen droplets stable is not the clay particles themselves but the hairy materials adsorbed on the clay.

5.4. Achievements

This study provided valuable information on some of the factors that affect the stability of the bitumen-in-water emulsion. It was found that:

- Asphaltenes greatly contribute to the stability of the emulsion.
- Deasphalted bitumen has a Hamaker constant in the range of 2.6×10^{-21} to 2.7×10^{-21} J.
- Deasphalted bitumen surface is smoother than untreated bitumen.
- Using a solution of NaCl/NaHCO₃ (pH of 8.5) instead of a solution of KCl (pH of 7) substantially reduces the interaction force between the bitumen droplets.
- Polymeric chains are likely adsorbed on the bitumen surface as well as on adsorbed clays.

5.5. Recommendations for Future Work

This study provided several answers on the conditions affecting the stability of bitumen droplets in water. However, many questions were also raised:

- Are chains only adsorbed on the bitumen droplets or are they also present in deasphalted bitumen?
- What is the mechanism of repulsion for the adsorbed polymeric chains?
- Is the repulsion mainly due to chains, to surface roughness or to a combination of both?
- What is the composition of the protrusions observed in the SEM images?
- How are asphaltenes distributed at the surface of the droplets?
- Is clay adsorbed on the bitumen droplets as a layer or in lumps?
- Would the bitumen emulsions become unstable at very high pH?

It is clear that substantial work is needed to understand the interaction between bitumen droplets in water. First, it is of primary importance to gain a better idea of the surface structure of the bitumen droplets and to develop a model that will represent the surface structure correctly. Since surface chemistry plays a major role in colloidal systems, it is also very important to determine the composition of the protrusions and to know how this composition will vary under different conditions.

The results of this study indicated that the existence of polymeric chains on the bitumen surface is likely. The repulsion mechanism of the chains was not clear and should be determined before a more advanced interaction model is developed. Finally, although clay is known to greatly affect the stability of bitumen emulsions, the repulsive force is somewhat masked by the original repulsion between untreated bitumen droplets. Experiments under different experimental conditions should be performed to further investigate the effect of clay. In addition, before attempting to model the interaction in bitumen, water and clay systems, a SEM image of the surface of the bitumen droplets should be taken to determine the distribution of clay on the surface.

In today's world where optimisation of resources is highly valued, it is desirable to reduce the losses of bitumen encountered in oil sands processing. A substantial

reduction of the bitumen losses can only be realised if the mechanisms of bitumen-bitumen droplet stability are understood. This study was carried out with that objective in mind and brought us closer to reaching an understanding of the stability of bitumen droplets in water.

BIBLIOGRAPHY

1. Energy Statistics Handbook, Statistics Canada, Natural Resources Canada, 1999.
2. Alberta's Reserves 1997, Alberta Energy and Utilities Board, Statistical Series, 98-18, 1997.
3. Outtrim, C.P., Evans, R.G., Alberta's Oil Sands Reserves and Their Evaluation in The Oil Sands of Canada-Venezuela, CIM Special Issue, 1977, 17, D.A. Redford and A.G. Winestock, Eds.
4. Gray, M.R., Masliyah, J.H., Extraction and Upgrading of Oilsands Bitumen, Documentation from an Intensive Short Course given by the authors. 1998.
5. Schramm, L.L. (ed.), Suspensions: Fundamentals and Applications in the Petroleum Industry, Advances in Chemistry Series 251, 1996, 800p.
6. Wu, X., Hamza, N., Czarnecki, J., Masliyah, J., Interaction Forces between Bitumen Droplets in Water, Langmuir, 1999, 15, 5244.
7. McLean, J.D., Kilpatrick, P.K., Effects of Asphaltene Solvency on Stability of Water-in-Crude-Oil Emulsions, J. Colloid Interface Sci, 1997, 189, 242.
8. Schramm, L.L., Smith, R.G., The Influence of Natural Surfactants on Interfacial Charges in the Hot-Water Process for Recovering Bitumen from the Athabasca Oil Sands, Colloids Surf., 1985, 14, 67.

9. Wu, X., Dabros, T., Czarnecki, J., *Determining the Colloidal Forces Between Bitumen Droplets in Water Using Hydrodynamic Force Balance Technique*, *Langmuir*, **1999**, 15, 8706.
10. Wu, X., Laroche, I., Masliyah, J., Czarnecki, J., Dabros, T., *Applications of Colloidal Force Measurements Using a Microcollider Apparatus to Oil Sand Studies*, *Colloids Surf. A.*, in press.
11. Everett, D.H. *Basic Principles of Colloid Science*, Royal Society of Chemistry, London, **1988** 243 pp.
12. Gouy, G., *J. Phys.*, **1910**, 4,9, 457.
13. Chapman, D.L., *Phil. Mag.*, **1913**, 6,25, 475.
14. Masliyah, J.H., *Electrokinetic Transport Phenomena*, AOSTRA Technical Publication Series, **1994**, 363 p.
15. van de Ven, T.G.M, *Colloidal Hydrodynamics*, Academic Press, London, **1989**.
16. Langmuir, I., *J. Chem. Phys.*, **1938**, 6, 893.
17. Derjaguin, B., *Trans. Faraday Soc.*, **1940**, 36, 203.
18. Verwey, E.J.W., Overbeek, J.TH.G., *Theory of the stability of lyophobic colloids*, Amsterdam, **1948**.
19. Derjaguin, B., *Acta Physicochim U.R.S.S.*, **1939**, 10, 333.
20. Stern, O., *Z.Elektrochem.*, **1924**, 30, 508.

21. Napper, D.H., *Steric Stabilization*, *J. Colloid Interface Sci.*, 58, 2, 390.
22. Hamaker, H.C., *Physica*, 1937, 4, 1058.
23. Lifshitz, E.M., *The Theory of Molecular Attractive Forces Between Solids*, *Soviet Physics JETP*, 1956, 2, 73.
24. Schenkel, J.H., Kitchener, J.A. *A Text of the Derjaguin-Verwey-Overbeek Theory With a Colloidal Suspension*, *Trans. Faraday Soc.*, 1960, 56, 161.
25. van Silfhout, A., *Dispersion Forces between Macroscopic Objects I.*, *Proc. Konigs. Akad. Wetensh. B.*, 1966, 69, 501.
26. Ninham, B.W., Parsegian, V.A., *Biophys. J.*, 1970, 10, 646.
27. Derjaguin, B., Landau, L.D., *Acta Physicochim. U.R.S.S.*, 1941, 14, 633.
28. Walz, J.Y., *The effect of surface heterogeneities on colloidal forces*, *Adv. Colloid Interface Sci.*, 1998, 74, 119.
29. Czarniecki, J., Dabros, T., *Attenuation of the van der Waals ATtraction Energy in the Particle/Semi-Infinite Medium System Due to the Roughness of the Particle Surface*, *J. Colloid Interface Sci.*, 1980, 78, 25.
30. Suresh, L., Walz, J.Y., *Effect of Surface Roughness on the Interaction Energy between a Colloidal Sphere and a Flat Plate*, *J. Colloid Interface Sci.*, 1996, 183, 199.

31. Bhattacharjee, S., Ko, C., Elimelech, M., DLVO Interaction between Rough Surfaces, *Langmuir*, **1998**, 14, 3365.
32. Herman, M.C., Papadopoulos, K.D., Effects of Asperities on the van der Waals and Electric Double-Layer Interactions of Two Parallel Flat Plates, *J. Colloid Interface Sci.*, **1989**, 136, 385.
33. Richmond, P., Electrical Forces between Particles with Discrete Periodic Surface Charge Distributions in Ionic Solution, *J. Chem. Soc. Faraday Trans. II*, **1975**, 71, 1154.
34. Kuin, A.J., Interaction Potential of a Dispersion of Colloidal Particles with a Non-homogeneous Surface Potential, *Faraday Discuss. Chem. Soc.*, **1990**, 90, 235.
35. Vreeker, R., Kuin, A.J., Den Boer, D.C., Hoekstra, L.L., Agterof, W.G.M., Stability of Colloidal Particles with a Nonhomogeneous Surface Potential: Application to Colloidal Nickel Hydroxy Carbonate, *J. Colloid Interface Sci.*, **1992**, 154, 138.
36. Miklavic, S.J., Chan, D.Y.C., White, L.R., Healy, T.W., Double Layer Forces between Heterogeneous Charged Surfaces, *J. Phys. Chem.*, **1994**, 98, 9022.
37. Czarnecki, J., Warszynski, P., The Evaluation of Tangential Forces Due to Surface Inhomogeneities in the Particle Deposition Process, *Colloids Surf.*, **1987**, 22, 207.
38. Israelachvili, J.N., Kott, S.J., Measurements of Dynamic Interactions in Thin Films of Polymer Melts: The Transition from Simple to Complex Behavior, *J. Polym. Sci.: Pt B Polym. Phys.*, **1989**, 27, 489.

39. Israelachvili, J.N., Tandon, R.K., White, L.R., Measurement of Forces between Two Mica Surfaces in Aqueous Polyethylene Oxide Solution, *J. Colloid Interface Sci.*, **1980**, 78, 430.
40. Stewart, A.M., Parker, J.L., Force feedback surface force apparatus: Principles of operation, *Rev. Sci. Instrum.*, **1992**, 63, 5626
41. Binnig, G. Quate, C.F., Gerber, Ch., Atomic Force Microscope, *Phys. Rev. Lett.*, **1986**, 56, 930.
42. Li, Y.Q., Tao, N.J., Garcia, A.A., Lindsay, S.M., Direct Measurement of Interaction Forces between Colloidal Particles Using the Scanning Force Microscope, *Langmuir*, **1993**, 9, 637.
43. Prieve, D.C., Frej, N.A., Total Internal Reflection Microscopy: A Quantitative Tool for the Measurement of Colloidal Forces, *Langmuir*, **1990**, 6, 396.
44. Schumacher, G.A., Van de Ven, T.G.M., Evanescence Wave Scattering Studies on Latex-Glass Interactions, *Langmuir*, **1991**, 7, 2028.
45. Rädler, J., Sackmann, E., On the Measurement of Weak Repulsive and Frictional Colloidal Forces by Reflection Interference Contrast Microscopy, *Langmuir*, **1992**, 8, 848.
46. Rohrsetzer, S., Kovacs, P., Nagy, M., A new experimental method for determination of the repulsive force-distance relationship between disperse particles, *Colloid Polym. Sci.*, **1986**, 264, 812.

47. Xu, W., Nikolov, A., Wasan, D.T., Gonsalves, A., Borwankar, R.P., Particle Structure and Stability of Colloidal Dispersions as Probed by the Kossel Diffraction Technique, *J. Colloid Interface Sci.*, **1997**, 191, 471.
48. Nikolov, A.D., Wasan, D.T., Particle-particle interactions in concentrated dispersions as probed by the capillary force balance with application to batch sedimentation, *Powder Technology*, **1996**, 88, 299.
49. Grier, D.G., Optical tweezers in colloid and interface science, *Curr. Opin. Colloid Interface Sci.*, **1997**, 2, 264.
50. Velegol, D., Anderson, J.L., Determining the Forces between Polystyrene Latex Spheres using Differential Electrophoresis, *Langmuir*, **1996**, 12, 4103.
51. Vadas, E.B., Goldsmith, H.L., Mason, S.G., The Microrheology of Colloidal Dispersions I. The Microtube Technique, *J. Colloid Interface Sci.*, **1972**, 43, 630.
52. Takamura, K., Goldsmith, H.L., Mason, S.G., The Microrheology of Colloidal Dispersions: XII Trajectories of Orthokinetic Pair-Collisions of Latex Spheres in a Simple Electrolyte, *J. Colloid Interface Sci.*, **1981**, 82, 175.
53. Tha, S.P., Shuster, J., Goldsmith, H.L., Interaction Forces between Red Cells Agglutinated by Antibody II. Measurement of Hydrodynamic Force of Breakup, *Biophys. J.*, **1986**, 50, 1117.
54. Van de Ven, T.G.M., Warszynski, P., Wu, S., Dabros, T., Colloidal Particle Scattering: A New Method To Measure Surface Forces, *Langmuir*, **1994**, 10, 3046.

55. Salou, M, Siffert, B., Jada, A., Study of the stability of bitumen emulsions by application of DLVO theory, *Colloids Surf. A: Physicochem. Eng. Aspects*, **1998**, 142, 9.
56. Yan, Z., Elliott, J.A.W., Masliyah, J.H., Roles of Various Bitumen Components in the Stability of Water-in-Diluted-Bitumen Emulsions, *J. Colloid Interface Sci.*, **1999**, 220, 329.
57. Yan, Y., Masliyah, J.H., Solids-stabilized oil-in-water emulsions: scavenging of emulsion droplets by fresh oil addition, *Colloids Surf. A: Physicochem. Eng. Aspects*, **1993**, 75, 123.
58. Speight, J.G., Moschopedis, S.E., On the Molecular Nature of Petroleum Asphaltenes in Chemistry of Asphaltenes, *Adv. in Chem. Series*, Washington, **1981**, p2.
59. Am Soc. Test. Mater., Book ASTM Standards, **1996**.
60. Dabros, T., van de Ven, T.G.M., Surface Collisions in a Viscous Fluid, *J. Colloid Interface Sci.*, **1992**, 149, 493.
61. Goren, S.L., O'Neill, M.E., On the hydrodynamic resistance to a particle of a dilute suspension when in the neighbourhood of a large obstacle, *Chem. Eng. Sci.*, **1971**, 26, 325.
62. Wu, X., van de Ven, T.G.M., Characterization of Hairy Latex Particles with Colloidal Particle Scattering, *Langmuir*, **1996**, 12, 3859.
63. Strassner, J.E., Effect of pH on Interfacial Films and Stability of Crude Oil-Water Emulsions, *J. Petrol. Technol.*, **1968**, 20, 303.

64. Grim, R.E., Clay Mineralogy, 2nd ed., McGraw-Hill, New York, 1968, 596p.

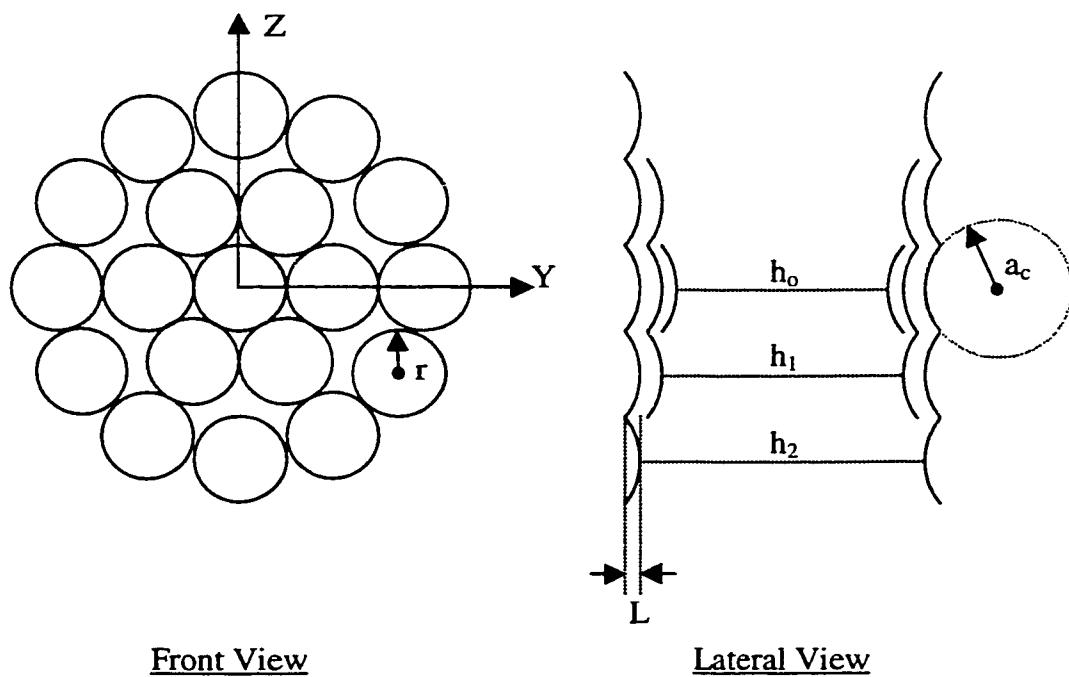
APPENDIX A

MULTIPLE SPHERICAL CAP MODEL

A.1. Geometric Considerations

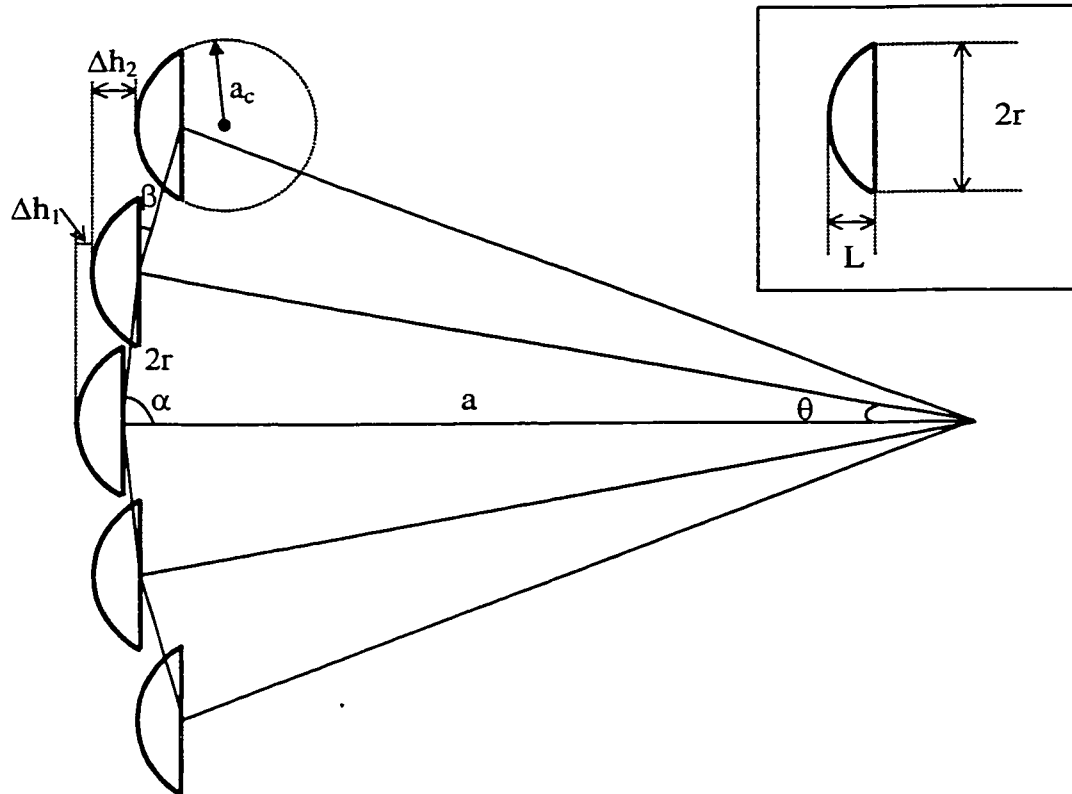
The multiple spherical cap model assumes that the protrusions at the surface of bitumen droplets can be modelled as truncated spheres. Figure A.1 gives a schematic representation of the spherical cap model. Three different levels of roughness were accounted for, corresponding to separation distances of h_0 , h_1 and h_2 . Since the interaction force decays rapidly with distance, contributions coming from higher levels were regarded as negligible.

Figure A.1: Representation of the Multiple Spherical Cap Model



To simplify the model, the spherical caps were vertically oriented and all of them had the same dimensions. In addition, the caps are assumed to directly face each other. The geometric parameters of the spherical cap model are presented in Figure A.2.

Figure A.2: Geometric Parameters of Multiple Spherical Caps Model



The geometry of the system gives:

$$\cos \alpha = \frac{r}{a} \quad (\text{A.1})$$

and

$$\frac{\Delta h_1}{2r} = \sin \left(\frac{\pi}{2} - \alpha \right) \quad (\text{A.2})$$

Combining both equations yields:

$$\Delta h_1 = \frac{2r^2}{a} \quad (\text{A.3})$$

Similarly,

$$\cos \theta = \left(1 - \frac{2r^2}{a^2}\right) \quad (\text{A.4})$$

and

$$\frac{\Delta h_2}{2r} = \sin \beta \quad (\text{A.5})$$

where the angle β is given by:

$$\beta = 90^\circ - (\alpha - \theta) = 90^\circ - \cos^{-1}\left(\frac{r}{a}\right) + \cos^{-1}\left(1 - \frac{2r^2}{a^2}\right) \quad (\text{A.6})$$

Rearranging the terms gives Δh_2 ,

$$\Delta h_2 = 2r \left[\frac{r}{a} \left(1 - \frac{2r^2}{a^2}\right) + \sin\left(\cos^{-1}\left(\frac{r}{a}\right)\right) \sin\left(\cos^{-1}\left(1 - \frac{2r^2}{a^2}\right)\right) \right] \quad (\text{A.7})$$

Therefore,

$$h_1 = h_0 + 2\Delta h_1 = h + \frac{4r^2}{a} \quad (\text{A.8})$$

$$\begin{aligned} h_2 &= h_1 + 2\Delta h_2 \\ &= h_1 + 4r \left[\left(\frac{r}{a} - \frac{2r^3}{a^3}\right) + \sin\left(\cos^{-1}\left(\frac{r}{a}\right)\right) \sin\left(\cos^{-1}\left(1 - \frac{2r^2}{a^2}\right)\right) \right] \end{aligned} \quad (\text{A.9})$$

As mentioned, the model assumes that the spherical caps are in a vertical position. This assumption is justified by the fact that the interior angle 4θ is less than 10 to 15° for the typical experimental values used. By taking the smallest droplets size possible, i.e. $a = 2 \mu\text{m}$, and $r = 60 \text{ nm}$ (value approximated from figure 3.8) one would obtain the highest possible deviation from the vertical. These parameters yield a deviation of less than 3.5° for the second level and of less than 7° for the third level. Moreover, the 7° deviation is located on a level that contributes very little to the interaction, as will be shown later.

To calculate the colloidal force, it is necessary to know the radius of the “virtual” sphere, a_c , from which the spherical cap is derived. This radius is given by:

$$(a_c - L)^2 + r^2 = a_c^2 \quad \text{or} \quad a_c = \frac{L^2 + r^2}{2L} \quad (\text{A.10})$$

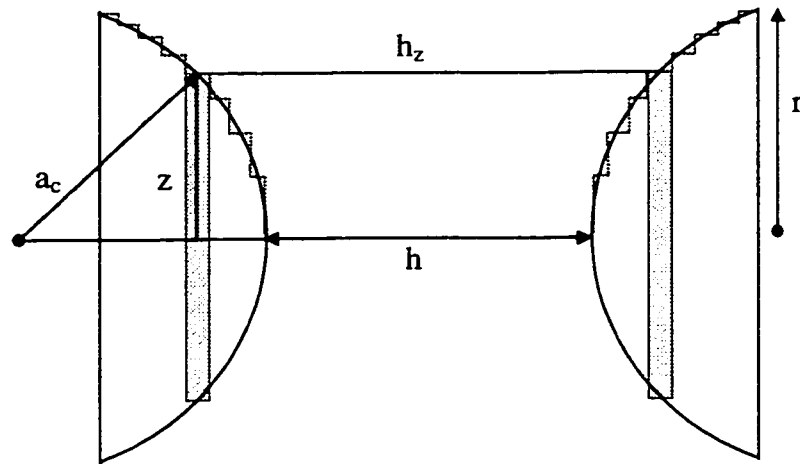
A.2. Electrostatic Force

The electrostatic force calculations are made by calculating the interaction from two spherical caps facing each other and summing over all the pairs of spherical caps. The interaction contributed from the gaps between the caps is neglected because the corresponding surface area is small and the separation distance is large. Making use of Derjaguin approximation [17], one can calculate the interaction force for particles having curved boundaries by assuming a series of flat strips. van de Ven [15] provides expressions for the interaction between parallel cylinders and spheres. A similar procedure is used here to first calculate the interaction between two parallel cylindrical caps and from the resulting expression, the interaction between two spherical caps.

A.2.1. Electrostatic Force between Parallel Cylinder Caps

Figure A.3 indicates the geometry of the cylindrical caps and provides the main geometric parameters.

Figure A.3: Geometry of Two Parallel Cylinders



From the geometry, it can be seen that:

$$h_z = 2\left(a_c - (a_c^2 - z^2)^{1/2}\right) + h \quad (\text{A.11})$$

The force per unit area between two strips separated by a distance h_z is given by:

$$F_z = B \exp(-\kappa h_z)$$

where $B = 32 \tanh^2\left(\frac{ze\psi_0}{4kT}\right) \epsilon_0 \epsilon \kappa^2 \left(\frac{kT}{ve}\right)^2$ (A.12)

In Equation A.12, v is used as the symbol for the electrolyte valence to avoid confusion with the distance z . All the other parameters are defined in the List of Symbols, Nomenclature or Abbreviations.

The force per unit length for the cylindrical strips will thus be:

$$\begin{aligned}
 F &= 2B \int_0^r \exp(-\kappa h_z) dz \\
 &= 2B \exp(-\kappa h) \int_0^r \exp\left(-2\kappa a_c + 2\kappa (a_c^2 - z^2)^{1/2}\right) dz
 \end{aligned} \tag{A.13}$$

However, because the main contribution to this integral comes from the strips located close to $z = 0$, the following approximation can be made:

$$-2\kappa \left(a_c - \sqrt{a_c^2 - z^2} \right) \cdot \frac{a_c + \sqrt{a_c^2 - z^2}}{a_c + \sqrt{a_c^2 - z^2}} = -2\kappa \frac{z^2}{a_c + \sqrt{a_c^2 - z^2}} \approx \frac{-\kappa z^2}{a_c} \tag{A.14}$$

Using the geometric parameters $L = 25$ nm and $r = 60$ nm, the maximum error resulting from the approximation given in Equation A.14 is 15% and occurs at $z = r$, i.e. at the position where the electrostatic force is the lowest.

Consequently, the force per unit length can be approximated by:

$$F = 2B \exp(-\kappa h) \int_0^r \exp\left(\frac{-\kappa z^2}{a_c}\right) dz \tag{A.15}$$

The integral in Equation A.15 has no definite value, unless r tends to infinity. Before testing if the assumption is valid for the size of the droplets used in this study, the following change of variable was made:

$$t = \sqrt{\frac{\kappa}{a_c}} \quad (\text{A.16})$$

Equation A.15 thus becomes:

$$F = 2B\sqrt{\frac{a_c}{\kappa}} \exp(-\kappa h) \int_0^r \sqrt{\frac{\kappa}{a_c}} \exp(-t^2) dt \quad (\text{A.17})$$

From the definition of the error function:

$$\int_0^r \sqrt{\frac{\kappa}{a_c}} \exp(-t^2) dt = \frac{\sqrt{\pi}}{2} \operatorname{erf}\left(r\sqrt{\frac{\kappa}{a_c}}\right) \quad (\text{A.18})$$

If $U = r\sqrt{\frac{\kappa}{a_c}} \geq 2.75$, then $\operatorname{erf}(U) = \operatorname{erf}(\infty) = 1$

In such cases, the force between two cylindrical caps is given by:

$$F = B\sqrt{\frac{\pi a_c}{\kappa}} \exp(-\kappa h) \quad (\text{A.19})$$

The validity of the $r = \infty$ assumption was tested by calculating the deviation in the error function resulting from it for several parameters. The results are presented in Table A.1 where $\kappa = 3.29 \times 10^8$ corresponds to a salt concentration of 0.01M and $\kappa = 6.58 \times 10^8$ to a concentration of 0.04M. Note the physical limitation: $L \leq r$.

It can be seen from Table A.1 that the assumption is justified for the experimental conditions (0.04M and protrusions dimensions $L = 25$ nm and $r = 60$ nm) used in this study. However, when the thickness of the spherical caps becomes too small, the error introduced becomes non-negligible. Practically, it is very unlikely that a protrusion with such a small thickness will affect the results.

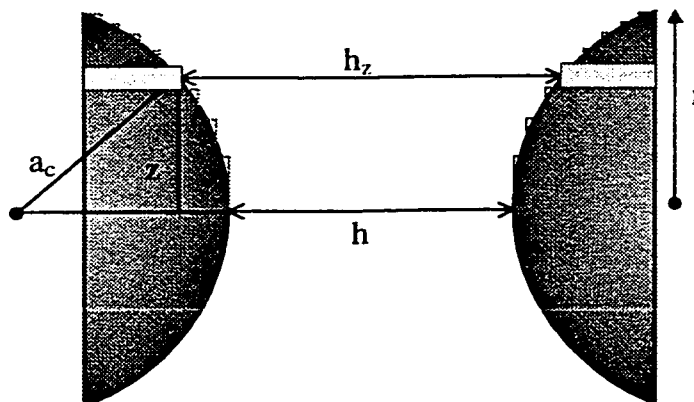
Table A.1: Error Related to the $r = \infty$ Assumption

κ (m^{-1})	r (nm)	L (nm)	a_c (nm)	$U=r(\kappa/a_c)^{1/2}$	$\text{erf}(U)$	% error
3.29×10^8	60	25	84.5	3.744	1.0000	0
6.58×10^8	60	25	84.5	5.295	1.0000	0
3.29×10^8	200	25	812.5	4.024	1.0000	0
6.58×10^8	200	25	812.5	5.692	1.0000	0
3.29×10^8	25	25	25.0	2.868	1.0000	0
6.58×10^8	25	25	25.0	4.056	1.0000	0
3.29×10^8	60	5	362.5	1.807	0.9894	1.06
6.58×10^8	60	5	362.5	2.556	0.9997	0.03
3.29×10^8	60	2	901.0	1.147	0.8948	10.52
6.58×10^8	60	2	901.0	1.621	0.9782	2.18
3.29×10^8	25	5	65.0	1.779	0.9881	1.19
6.58×10^8	25	5	65.0	2.515	0.9996	0.04
3.29×10^8	25	2	157.25	1.144	0.8942	10.58
6.58×10^8	25	2	157.25	1.617	0.9780	2.2

A.2.2. Electrostatic Force between Spherical Caps

The force between two parallel spherical caps can then be calculated, starting with the expression obtained for two parallel cylindrical caps. The geometry and the parameters for the two spherical caps are indicated in Figure A.4.

Figure A.4: Geometry of two Parallel Spherical Caps



In this case, the electrostatic force can be calculated by dividing the two spheres into a series of horizontal cylindrical strips and integrating the expression obtained for the cylindrical strips from $z = -r$ to $z = +r$.

To do so, the following substitutions need to be made:

$$\begin{aligned} a_c &\Rightarrow (a_c^2 - z^2)^{1/2} \\ h &\Rightarrow h_z = 2\left(a_c - (a_c^2 - z^2)^{1/2}\right) + h \end{aligned} \quad (\text{A.20})$$

Thus, the electrostatic force between two spherical caps is given by:

$$F = 2B\left(\frac{\pi}{\kappa}\right)^{1/2} \int_0^r (a_c^2 - z^2)^{1/4} \exp\left(-\kappa\left[2\left(a_c - (a_c^2 - z^2)^{1/2}\right) + h\right]\right) dz \quad (\text{A.21})$$

Using the approximation given in Equation A.14, Equation A.21 can be reduced to:

$$F = 2B\left(\frac{\pi}{\kappa}\right)^{1/2} \exp(-\kappa h) \int_0^r (a_c^2 - z^2)^{1/4} \exp\left(\frac{-\kappa z^2}{a_c}\right) dz \quad (\text{A.22})$$

Equation A.22 can be solved using a numerical integration procedure.

A.2.3. Total Electrostatic Force

The total electrostatic interaction force is simply obtained by adding the interaction force between all the individual pairs of spherical strips. In other words,

$$F_{el} = F_{\text{sph.caps}}(h_0) + 6F_{\text{sph.caps}}(h_1) + 12F_{\text{sph.caps}}(h_2) \quad (\text{A.23})$$

where

$$F_{\text{sph.caps}}(h) = 2B\left(\frac{\pi}{\kappa}\right)^{1/2} \exp(-\kappa h) \int_0^r (a_c^2 - z^2)^{1/4} \exp\left(\frac{-\kappa z^2}{a_c}\right) dz \quad (\text{A.24})$$

However, numerical analysis has shown that the total electrostatic contribution from the third level or roughness, i.e. for the spherical caps separated by a distance of h_2 , is negligible. The highest contribution calculated for this level of roughness was 0.3%. Hence, the model could be further simplified by using only two levels of protrusions.

A.3. London-van der Waals Force

The total London-van der Waals force was calculated based on Hamaker's pairwise additivity method [22] accounting for all possible contributions. Thus, the total van der Waals force is given by:

$$\begin{aligned}
 F_{\text{vdw}} = & F_{\text{vdw},s-s}(h_0 + 2L) + F_{\text{vdw},sc-sc}(h_0) + 6F_{\text{vdw},sc-sc}(h_1) \\
 & + 12F_{\text{vdw},sc-sc}(h_2) + 2F_{\text{vdw},sc-s}(h_0 + L) + 12F_{\text{vdw},sc-s}(h_1 + L) \\
 & + 24F_{\text{vdw},sc-s}(h_2 + L)
 \end{aligned} \tag{A.25}$$

In Equation A.25, the subscript s refers to a sphere and the subscript sc refers to a spherical cap. Thus, $F_{\text{vdw},sc-s}$ is the van der Waals force arising from the interaction between a spherical cap and a sphere. The first term of Equation A.25, corresponding to the interaction between the two bitumen droplets, can be calculated using Equation 3.1. The London-van der Waals force between two spherical caps and between a spherical cap and a droplet were calculated using a formula similar to the one developed by Wu *et al.* [9] for the attractive force between two disks:

$$F_{\text{vdw}} = -\frac{A}{\pi^2} \int dy_2 \int dz_2 \int dx_1 \int dy_1 \int dz_1 \left(\frac{f(q_1)}{d_1^6} - \frac{f(q_2)}{d_2^6} \right) \tag{A.26}$$

Equation A.26 is applicable to both $F_{\text{vdw},sc-sc}$ and $F_{\text{vdw},sc-s}$. Therefore, the subscripts 1 and 2 can refer to either a spherical cap or a sphere. However, the upper and lower limits of the integrals have to be adjusted accordingly. The system of coordinates is

defined in Figure A.1. The variables d_1 and d_2 of Equation A.26 are, respectively, the closest and farthest separation distances when the coordinates x_1, y_1, z_1, y_2 and z_2 are fixed. In Equation A.26, $f(q)$ is a retardation function that differs from that presented in Chapter 1 and is expressed as [9]:

$$f(q) = \frac{1 + 19.39q + 7,526q^2}{1 + 19.31q + 8.436q^2 + 2.946q^3} \quad (\text{A.27})$$

where $q = 2\pi d/\lambda$ (λ being the retardation wavelength). See Figure 10 of Wu *et al.* [9] for further details and note that they used a different system of axes (x and z are interchanged).